Following the Cosmic Evolution of the Pristine Gas

Pop III Star Formation and the First Galaxies

by

Richard John Sarmento

A Dissertation Presented in Partial Fulfillment
of the Requirements for the Degree
Doctor of Philosophy

Approved May 2018 by the
Graduate Supervisory Committee:

Evan Scannapieco, Chair
Jennifer Patience
Frank Timmes
Rogier Windhorst
Patrick Young

ARIZONA STATE UNIVERSITY

August 2018

ABSTRACT

The formation of the first stars, some 100-300 Myr after the Big Bang, marked the end of the cosmic dark ages and resulted in the creation of most of the elements. Understanding their formation, lifetimes, and contributions to the evolution of our universe is one of the current frontiers in astronomy and astrophysics.

While Hubble and other large telescopes have peered back into the first giga-year post-Big Bang, no one has yet observed a metal-free star. Hence it is left to theory and simulation to explain their likely characteristics.

In this work I present a new model for following the formation of Population III (Pop III) stars and follow their effects on early galaxy evolution. I make use of a new subgrid model of turbulent mixing to accurately follow the time scales required to mix supernova (SN) ejecta – enriched with heavy elements – into pristine parcels of gas. I implement this model in a large-scale cosmological simulation and follow the fraction of gas with metallicity below a critical value marking the boundary between Pop III and metal enriched Population II (Pop II) star formation. I demonstrate that accounting for subgrid mixing results in a Pop III star formation rate that is 2-3 times higher than standard models with the same physical resolution.

I also implement and follow a new "primordial metals" (PM) scalar that tracks the metals generated by Pop III SNe. A subset of these SNe generate metals with unique abundance signatures that are taken up by second generation stars resulting in a subclass of carbon-enhanced, metal-poor (CEMP) stars. By tracking both regular metals and PM, I can model, in post-processing, the elemental abundances of simulation stars. I find good agreement between observations of CEMP-no Milky Way halo stars and simulated second-generation stars when assuming the first stars had a typical mass of $60 M_{\odot}$, providing a clue as to the Pop III initial mass function.

DEDICATION

First and foremost I dedicate this work to my loving husband, Jeff Bender. His patience and support was on display every day. I also dedicate this work to my parents, Richard and Elaine. Although gone, they taught me the value of an education and doing what you love. Finally, this work is dedicated to all those who have supported me during my studies... and to all those who find joy in wondering.

ACKNOWLEDGMENTS

While I have always been connected to space science in one way or another, my path to astrophysics was unexpected. Starting a PhD program in your late 40's may not be uncommon, but it certainly is not the norm. This is especially true for me since I had no intention of enrolling in a formal degree program, let alone finishing one, that first day I sat in an undergraduate astrophysics course in 2010. Even after taking several graduate courses, for personal enrichment, I didn't see myself where I am today. For that I owe a debt of gratitude to my School of Earth and Space Exploration professors and fellow students. Their enthusiasm and passion rekindled my love for the subject and carried me through the many trials every graduate student runs into along the way.

In that regard I would like to especially thank Rogier Windhorst and Evan Scannapieco. Professor Windhorst encouraged me to apply to the program and convinced me I could do the work. Professor Scannapieco, my thesis advisor, got me interested in the first stars and took the extra time to guide and mentor a part time graduate student. His patience and guidance were more than I had a right to expect and without it I would surely never have crossed the finish line. The support and challenges he provided me were 'fine-tuned' to my situation as it evolved from part-time student to full-time researcher. I am truly indebted to him for his mentorship over these last several years.

My time at ASU was enriched by all of the new friends and colleagues I have made over the last 7 years. It was truly wonderful to get to know so many bright and energetic students, post-docs, and faculty. Their encouragement and help was a big part of my success.

Then there was the support I received at home. Leaving a successful engineering career and living on a grad student salary is one thing for an individual, but another

thing altogether when you are settled in a committed relationship and stable homelife. In that regard, as in many others, I could not have asked for a better partner in life. My husband Jeff supported me both emotionally and financially in grad school and without him I would not have even been able to attempt this degree, let alone complete it. There were countless nights where his patience was on display: whether I was up late working or just distracted with a problem over dinner, he was always there with a word of support and encouragement. Jeff is the love of my life and I could not even have imagined completing this program without him at my side.

I would also like to thank the National Science Foundation (Grants AST-1715876 & PHY-1430152), the Joint Institute for Nuclear Astrophysics – Center for the Evolution of the Elements (JINA-CEE), NASA theory grant NNX15AK82G, and Professor Frank Timmes for funding my research. I would not have been able to complete this work without their support.

Lastly, I'd like to thank all my friends and family who have stood by me as I embarked on yet another crazy challenge.

TABLE OF CONTENTS

CHAPTER Page

CHAPTER Page

LIST OF TABLES

LIST OF FIGURES

Figure Page

Chapter 1

INTRODUCTION TO COSMOLOGY AND THE FIRST STARS

Our understanding of the universe has progressed at an astounding rate over the last century. It was only about 100 years ago that most astronomers believed the universe was composed of just our Galaxy. However, we now know our universe is unimaginably larger than the Milky Way (MW) and even locally we see a neighborhood populated with dozens of galaxies. Looking deeper we see a clumpy, irregular arrangement of galaxies that is part of a vast web-like structure where galaxies and galaxy clusters surround bubble-like voids where the density of matter is only about 20% of the mean cosmic density (van de Weygaert, 2016). The super-clusters, the largest of these structures, may contain 10's of thousands of galaxies.

Astonishingly, over that same 100 years, astronomers, cosmologists, and physicists have formulated a picture of our universe that ties together observation and theory into a coherent framework. While many puzzling questions remain, the fact that we can speak cogently of the universe's 13 billion year history is a remarkable achievement.

In this introduction I will briefly recap our understanding of cosmology, or the study of the universe as a whole, which leads naturally into some of the less-well understood, and as yet unobserved, details of its early evolution. It is this earliest era – the era of the first stars and galaxies some 100-300 million years (Myr) after the Big Bang (BB) – that has become the center of my research. In particular, the characteristics of the first stars to form in the universe, the so-called Population III (Pop III) stars, are mostly unknown and wholly unobserved. As astronomers have not (as yet) observed Pop III stars in our Galactic neighborhood, or in the high-redshift

universe, it falls to theory and simulation to glean their characteristics and to guide observations for the next generation of giant telescopes. This work is an attempt to further our understanding of these stars and to guide such searches.

1.1 The Very Early Universe

We have strong evidence that the universe started in a hot, BB (Lemaître, 1927; Riess et al., 1998; Perlmutter et al., 1999; de Bernardis et al., 2000; Roos, 2008) in which the matter and energy we now detect and measure was concentrated at an exceedingly high density approximately 13.8 billion years ago. The primordial universe was a remarkably smooth and homogeneous place (Peebles, 1980). However, during the first few minutes after the BB, matter congealed out of the primordial plasma to form the first ions and electrons. This first nucleosynthesis populated the universe with ionized hydrogen (H) and helium (He) [1] .

For the first several hundred thousand years, the universe was still hot enough to keep the new-born atoms ionized. This meant that Thomson scattering, scattering off-of free electrons, ensured that the photons were in thermal equilibrium with the baryons (since the coulomb force bound electrons to the H and He ions) resulting in a optically thick universe in which photons traveled very short distances before interacting with matter. Hence, most electromagnetic information from this era was essentially 'washed out' by photon scattering. However, as discussed below, not all of the information encoded in the photons from this era was randomized.

While this initial distribution of matter and energy was very smooth it was not perfectly so. Primordial quantum fluctuations, inherent in the fabric of space-time on scales less than 10^{-28}cm, were stretched, via inflation (Guth & Pi, 1982), in the first 10^{-32} seconds of cosmic history. These fluctuations seeded matter-energy density

[1] and a trace of lithium.

variations on cosmological scales before the universe was 1 second old (Turner, 1999; Guth & Kaiser, 2005). These included variations in the matter-energy constituents of the universe: dark matter (DM), 'regular' matter and radiation. However, since DM does not interact with electromagnetic radiation, it was free to start collapsing under its own gravity very soon after this epoch.

The DM overdensities continued to collapse gravitationally, but for the first several hundred thousand years the baryons could not follow the DM collapse because of the photon pressure in the tightly coupled baryon-photon fluid. This struggle between gravity and pressure set up oscillations (the baryon acoustic oscillations - BAO) that alternately heated (compression mode) and cooled (expansion mode) the overdensities as compared to the mean plasma temperature (Hu & White, 1996). However, once the universe had adiabatically cooled to $\approx$ 3000K recombination [2] (Peebles, 1968) was possible. We can estimate the redshift of recombination by noting that the temperature of the universe scales with redshift as $T(z) = T_0\,(1+z)$, where $T_0 = 2.725$ K is the temperature of the CMB today. This means recombination occurred at $z \approx 1100$ or approximately $380,000$ yrs after the BB. This is when the electrons combined with the H and He atoms to form a (mostly) neutral gas. At this point most photons, those with energies that did not correspond to the discrete energy levels of these atoms, were able to free stream across the universe. However, because the photons were liberated from baryons that were grouped into various concentrations, the radiation from this epoch carried the imprint of those over and underdensities (Eisenstein et al., 2005).

At present day, this imprint manifests itself as temperature fluctuations in the photons that make up the cosmic microwave background (CMB), Figure 1.1. They are the photons that streamed freely after recombination and the decoupling of radiation

[2]Something of a misnomer since electrons and ions had not previously been combined.

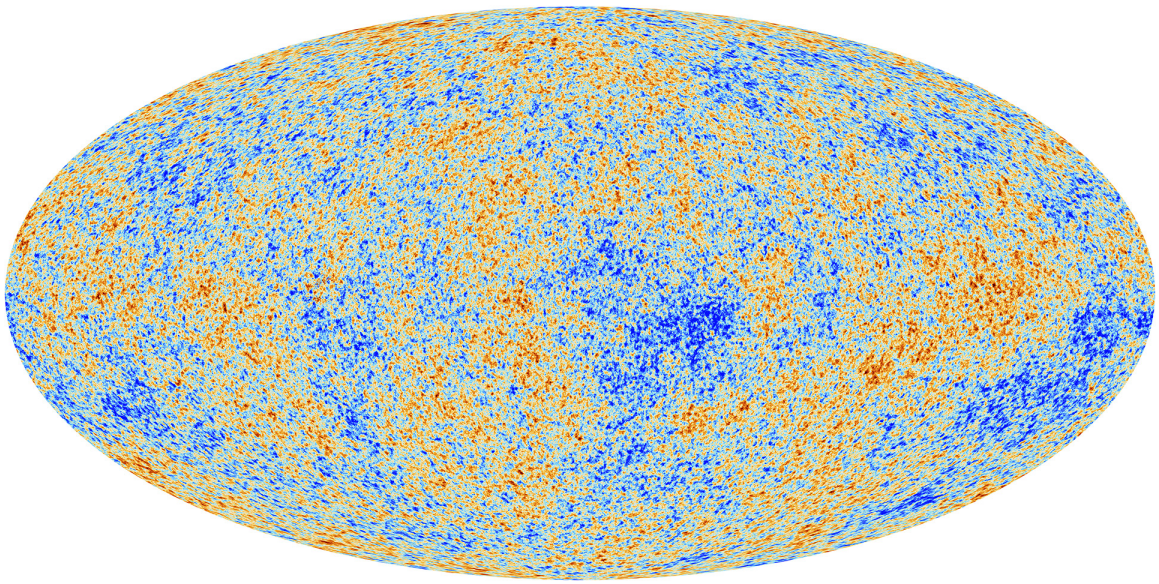

Figure 1.1: The Cosmic Microwave Background. Colors encode temperature fluctuations on the order of micro-Kelvins corresponding to regions of slightly different densities. These density fluctuations were the seeds of the structure we see in the universe today. (Image credit: ESA and the Planck Collaboration).

from regular matter. The temperature variations (Sachs & Wolfe, 1967) have a scale (on the sky - approximately 1 degree) related to the characteristic size-scale of the BAO and are a powerful constraint not only on the characteristic scale of structure we see today, but on the amount of DM in the universe.

After the epoch of recombination/decoupling the baryons were freed from their pressure support and began collapsing. However, the baryons had a gravitational boost: As hinted at above, the Λ Cold Dark Matter (ΛCDM) (Andernach & Zwicky, 2017; Frenk & White, 2012; Zwicky, 1933) model predicts that DM does not interact with electromagnetic energy and was therefore free to begin collapsing under its own gravity before decoupling. DM gravitational collapse could being once the predominate source of energy-density in the universe was not the relativistic photons.

The era of radiation dominance ended when matter became the dominate source of energy density in the universe. The point of matter-radiation equality is defined as

the time when $\rho_r(t) = \rho_m(t)$ or $\rho_{r,0}(1+z)^4 = \rho_{m,0}(1+z)^3$ since the radiation density decays due to both spatial dilution and the redshift of the photons' wavelengths, while the matter density only dilutes because of the expanding volume (Frieman et al., 2008). Since the radiation and matter densities are related to the density parameters, $\Omega_{r,0}$ and $\Omega_{m,0}$, by the same factor we can write

$$z_{\rm m} = \frac{\Omega_{m,0}}{\Omega_{r,0}} - 1 \approx 3200, \tag{1.1}$$

as a reasonable estimate of the redshift of matter-radiation equality. This is about 55,000 years after the BB and the time when the matter density became the dominant form of energy-density of the universe [3] . Hence, DM gravitational collapse had an ≈325 kyr 'head start' as compared to the baryons. Figure 1.2 depicts the relative contributions to the total energy density of the universe as a function of redshift, and depicts the redshift when each component of our universe was/is predominant. As shown, it is only very recently that dark energy has become the dominant component of the universe.

The matter density continued to grow in these early structures as baryons collapsed into the gravitational wells seeded by the DM. As discussed in the next section, it is within these primordial DM halos that the first stars were born, ending the cosmic dark ages. Additionally, some of these halos combined to make even more massive protogalaxies that were capable of gravitationally attracting even more gas. From here the process of hierarchical assembly continues, to the present epoch. This history provides us with the basic understanding leading to the formation of the first stars and galaxies. We can now relate the earliest anisotropies, $t_{age} < 1$ sec, in the primordial universe to the Large Scale Structure (LSS) we see today, 13.8 Gyr later

[3] We can also estimate the temperature of the universe at matter-radiation equality: $T(z) = T_0\,(1+z) \approx 8700K$. This is 45% hotter than the surface of the sun but was the temperature of the entire universe at $z = 3200$.

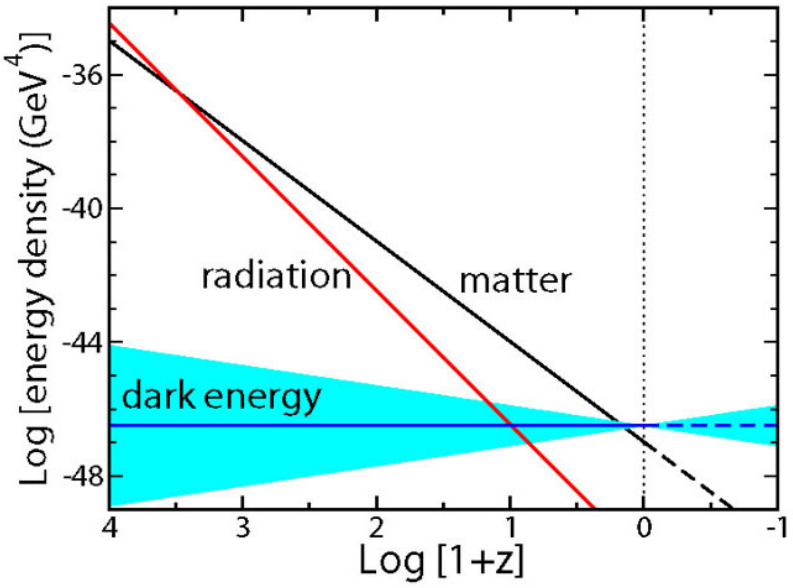

Figure 1.2: The dominant component of the universe throughout cosmic history. Radiation dominated the density of the universe for the first 50,000 yrs giving way to matter-density. We currently live in a dark energy dominated universe. The light blue shaded region captures an uncertainty of 20% in the equation of state parameter, $w = -1$, for dark energy. Dark energy has only recently become the dominant form of energy density in the universe. (Image credit: Frieman et al. (2008)).

(Press & Schechter, 1974). That we can trace the universe's origin to the first fraction of a second after the BB is one of the most astounding results in science.

1.2 The First Stars and Galaxies

The first stars formed from the baryons that collapsed into the structures seeded by DM at redshift $20 \leq z \leq 15$ (Bowman et al., 2018). However, while the physics that describes star formation in the modern universe is relatively well understood, and has been observed locally (Larson, 2003; McKee & Ostriker, 2007), the conditions surrounding the formation of the first stars is still theoretical and much more uncertain (Abel et al., 2000; Norman, 2010). This is due to Pop III stars' unique composition. Whereas the fast majority of the stars born in the universe contain traces of metals,

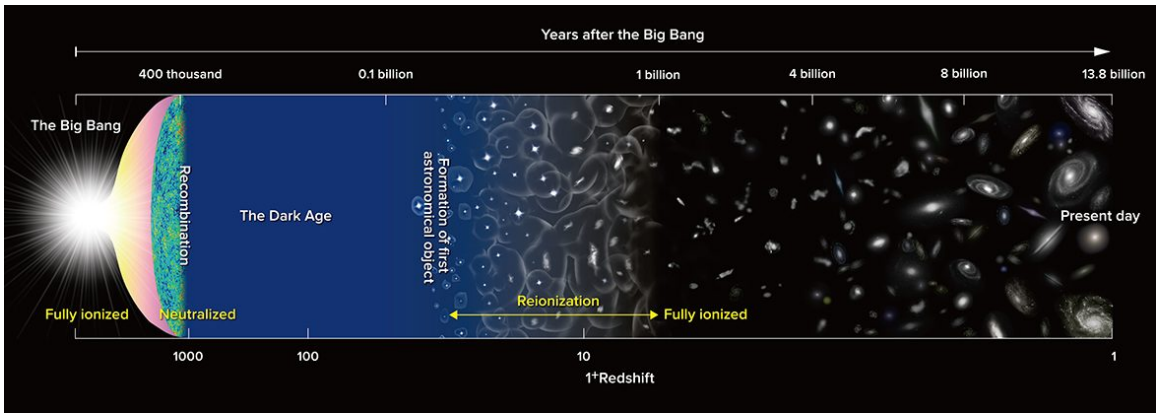

Figure 1.3: The history of our universe. From it's start in a hot, Big Bang to the formation of galaxies and galaxy clusters, astronomers and astrophysicists have a compelling and surprising well-understood story to tell. However, there are still many details left to fill-in. (Image credit: National Astronomical Observatory of Japan).

i.e. - elements heavier than He, the first generation of stars were composed purely of hydrogen and helium (Schaerer, 2002).

While hydrogen is the main source of fuel for all stars on the main sequence, the presence of metals significantly changes the characteristics of collapsing gas and of the subsequent star (Abel et al., 2002). Trace metals allow a gas heated by gravitational collapse to cool radiatively since many metals have low-lying energy transitions that can be collisionally excited. Such collisions convert the kinetic energy of the gas to radiation once the atom relaxes to a lower energy state. Such photons typically escape an optically thin gas. Additionally, metals in the photosphere of stars tend to 'trap' photons making a star puffier than its more compact Pop III equivalent and metals such as carbon and oxygen are crucial to nuclear reactions in the core. Without them Pop III stars have higher core and surface temperatures (Ezer & Cameron, 1971; Heger & Woosley, 2010).

As baryons collapsed into primordial DM halos they condensed into the first star-forming clouds. However, as just briefly discussed, heat generated by the collapse was difficult to dissipate in a gas composed of only H and He since the only radiative

cooling channel below $\approx 10^4$ K was provided by hydrogen molecules (Hutchins, 1976; Abel et al., 2000; Bromm & Loeb, 2003) – which was present in only trace amounts. Hence star formation could only proceed in DM minihalos where gravity could overcome the thermal pressure in clumps of gas cooled, to ≈ 200 K, only by molecular hydrogen. This required a mass of $\sim 10^6 M_\odot$, (Yoshida et al., 2003). Hence minihalos with approximately this mass are thought to be the site of first-star formation.

While minihalos were able to gather enough gas to create protostellar clouds, the DM in the halo remained diffuse since it was not able to cool radiatively. Primordial gas was therefore only able to undergo runaway collapse when it reached a mass such that $t_{\rm ff} < t_{\rm sc}$, where $t_{\rm ff} = \sqrt{\frac{3\pi}{32G\rho}}$ is the gravitational free-fall time of the gas and $t_{\rm sc} = \frac{R}{c_s}$ is the sound crossing time in a spherical region of gas with radius R. If we relate the sound crossing time to the temperature and density of the gas, $c_s = \sqrt{\frac{5kT}{3\mu m_p}}$, and the radius, $R = \left(\frac{3M}{4\pi\rho}\right)^{1/3}$, to the mass in a spherical region of uniform density, we can determine the Jeans Mass, the mass required for runaway collapse (Collins, 1989),

$$M_{\rm j} \approx 500 M_\odot \left(\frac{T}{200\,{\rm K}}\right)^{3/2} \left(\frac{n}{10^{-4}}\right)^{-1/2}. \tag{1.2}$$

Since the temperature of primordial gas clouds was likely 10-20 times higher than the temperature of gas cooled via metal lines, the Jeans mass in the early universe was likely 100 times what we expect (and observe) today. This likely resulted in a massive generation of first stars on the order of 100 $M_\odot$ (Bromm et al., 1999; Yoshida et al., 2006; O'Shea & Norman, 2007). Such massive stars have typical lifetimes between 1 and 10 Myrs (Schaerer, 2002) since the higher temperature in their cores results in a significant increase in the nuclear reaction rate. The formation of these first, massive stars marked the end of the cosmic dark ages that persisted since recombination/decoupling. Figure 1.4 is an artist's rendering of a supermassive Pop III star.

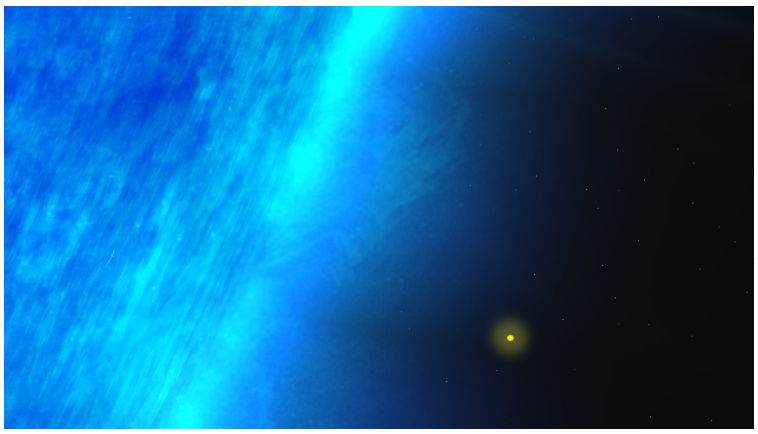

Figure 1.4: An artist's conception of a supermassive Pop III star compared to a small dwarf. While the theoretical jury is still out, Pop III stars may have been 100's of times more massive than our Sun.

The formation of the first stars may not herald the first galaxies since there is some debate as to the definition of a galaxy (Greif, 2015). The feedback from this first generation of stars in minihalos was likely enough to expel most of the remaining gas from their shallow potential wells, stifling further star formation. If we require that galaxies be able to maintain star formation over some length of time, and hence retain a significant fraction of their gas, the first galaxies were born later, when atomic cooling halos began to coalesce (Oh & Haiman, 2002). These halos had virial temperatures in excess of 10^4 K where cooling by H atomic lines was still effective and the partially ionized gas was conducive to H_2 formation (Glover, 2005).

While the first Pop III stars likely formed in minihalos, the larger atomic cooling halos may have produced larger numbers of Pop III stars as well as second generation Pop II stars with $Z > Z_{\rm crit}$ (Greif et al., 2008). This is the metallicity above which gas clouds are able to fragment and generate stars more akin to those in the local universe (Hutchins, 1976; Bromm & Loeb, 2003). The location, persistence, and formation rates for Pop III stars is still an area of intensive research.

1.3 Tying the First Stars to Observations

After their short lifetimes, most of the first stars ended their lives as SN. However, the nucleosynthetic products they generated was dependent on their masses. Stars in the mass range $25M_{\odot} \lesssim M_{\star} \lesssim 140M_{\odot}$ and $M_{\star} \gtrsim 260M_{\odot}$ leave a black hole (BH) remnant that traps most of the heavier elements while injecting lighter elements, such as carbon and oxygen, into the ISM (Heger et al., 2003). In the mass range $140M_{\odot} \lesssim M_{\star} \lesssim 260M_{\odot}$ stars end their lives as pair-instability supernova (PISN) which completely disrupt the star. These PISN pollute their surroundings with an abundance of heavy elements, such as iron and nickel. Both of these types of SN polluted early halos, as well as the intergalactic medium (IGM) giving rise to the next generation of stars, the Pop II stars, that have $Z > Z_{\rm crit}$. Figure 1.5 depicts the fates of metal free stars from sub-solar to kilo-solar masses.

The relationship between progenitor mass and SN chemical yields allows us to tie the metal content in ancient stars that we observe today to the likely mass ranges of Pop III stars (Frebel et al., 2005). In particular, observations of the chemical composition of metal poor (MP) stars in the MW halo and in nearby Ultra-faint dwarf (UFD) galaxies are thought to be the direct result of pollution by the SN ejecta of a single (or at most a few) primordial star(s) (Simon et al., 2015). By examining these stars' elemental abundances, and matching them (after considering dilution and mixing) to the nucleosynthetic SN products of models of the first stars, we can reverse-engineer the likely characteristics of the progenitors. This is near-field cosmology and was first described by Freeman & Bland-Hawthorn (2002). The process allows us to glean some of the first stars' likely characteristics (Cooke & Madau, 2014; Frebel & Norris, 2015) – or at least rule out unlikely initial mass functions (IMFs).

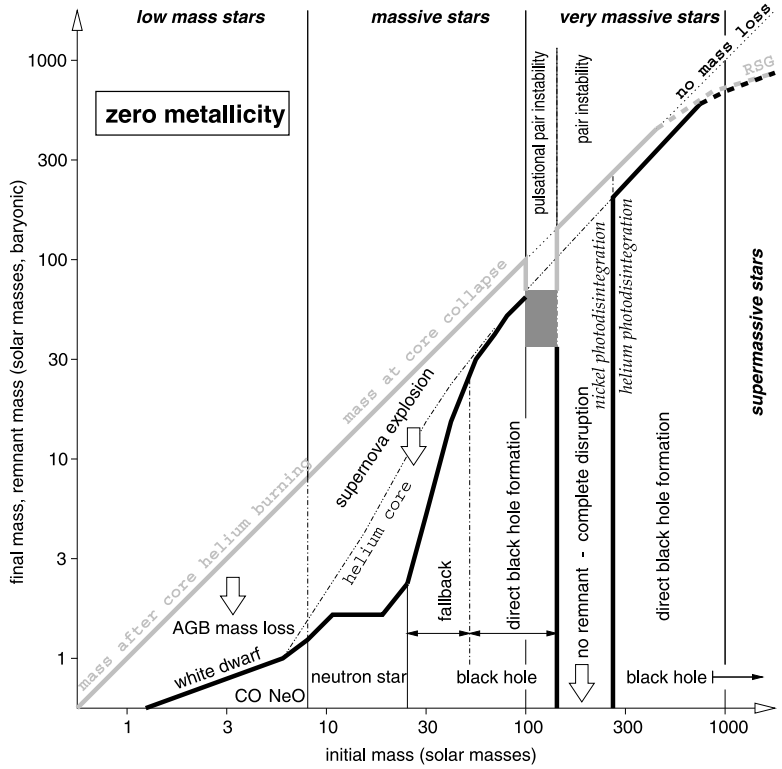

Figure 1.5: The fate of stars with various progenitor masses. Stars in the mass range $25 \lesssim M_\star/M_\odot \lesssim 140$ likely leave a BH after going SN trapping most heavy elements within the singularity. Stars in the mass range $140 \lesssim M_\star/M_\odot \lesssim 260$ likely end their lives as PISN and are completely disrupted. These two types of SN have very different elemental yields. Image credit: Woosley et al. (2002).

1.4 Modeling the Formation of Pop III Stars

Given the lack of observations, it falls to simulation and modeling to glean the likely characteristics of the first stars (Scannapieco et al., 2003, 2006; O'Shea & Norman, 2007; Wise et al., 2012). While physical concerns such as radiative and supernova (SN) feedback figure prominently into our models of Pop III star formation, other less studied processes have the potential to significantly impact our understanding of early metal free star formation. One of the factors that is often overlooked in such simulations is the turbulent mixing of heavy elements that pollutes a star forming parcel of gas above the critical metallicity for Pop III star formation (Pan & Scalo,

2007; Greif et al., 2010; Bromm, 2013, 2014; Ritter et al., 2015). This is due to the typical range of scales involved. While simulating a meaning cosmological volume from initial conditions typically results in a best resolution of 10-100 pc, the mixing of pollutants into the gas takes place at much smaller scales, as we will discuss in Chapter 2.

To perform such comparisons we require cosmological simulations that model the formation, life and death of the stars all within a realistic hydrodynamical and gravitational context. For our work we have chosen RAMSES (Teyssier, 2002), an Eulerian adaptive mesh refinement (AMR) code.

Thorough mixing of pollutants within a primordial galaxy is not an instantaneous process and most cosmological simulations simply assume that SN pollutants are well mixed, instantaneously, at the scale of resolution elements. To study the effects of turbulent mixing timescales on Pop III star formation, we carry out simulations that track the fraction of pristine gas at subgrid scales. Our implementation of the mixing timescale is derived from a turbulent mixing model for gas stirred by SN (Pan et al., 2012, 2013). Specifically, we model the timescale required to pollute the pristine gas and characterize the effect on Pop III stars formation as well as the subsequent chemical evolution of early galaxies. Implementing and characterizing this model is the focus of Chapter 2, along with predictions concerning the likely mass of Pop III stars based on observations of MW halo Carbon Enhanced Metal Poor (CEMP) stars. In Chapter 3 we address the observability of high redshift Pop III galaxies in the context of our new subgrid model.

Observing Pop III stars is the next frontier in observational astronomy. Understanding their formation, masses and lifetimes is the key to understanding a variety of topics from early structure formation and reionization to the history of chemical enrichment. We hope this work contributes to this ongoing scientific endeavor.

Chapter 2

FOLLOWING THE PRISTINE GAS: IMPLICATIONS FOR MILKY WAY HALO STARS[1]

2.1 Introduction

The death of the first stars resulted in the highly nonuniform pollution of the universe. By this time big bang nucleosynthesis had produced helium efficiently, but it had been halted by the expansion of the universe before it could go much further, leaving stars and supernovae (SNe) to form and disseminate the heavier elements (Walker et al., 1991). These early SNe first enriched the gas in and around protogalaxies which, in turn, led to a gradual, spatially inhomogeneous transition from metal-free Population III (Pop III) star formation to metal-enriched Population II (Pop II) star formation (Scannapieco et al., 2003, 2006; Brook et al., 2007; Tornatore et al., 2007; O'Shea & Norman, 2007; Trenti & Shull, 2010; Maio et al., 2010; Wise et al., 2012; Crosby et al., 2013; Johnson et al., 2013; Pan et al., 2013; Pallottini et al., 2014).

Most of the properties of this transition remain unknown. High-redshift observations have yielded candidates for Pop III stellar populations (Malhotra & Rhoads, 2002; Dawson et al., 2004; Jimenez & Haiman, 2006; Dijkstra & Wyithe, 2007; Nagao et al., 2008; Kashikawa et al., 2012; Cassata et al., 2013) including a single $z = 6.6$ galaxy with no detected metal emission lines and narrow HeII λ1640 emission (Sobral et al., 2015) that is possibly indicative of metal-free stars (e.g Tumlinson et al., 2001; Schaerer, 2002). However, these measurements are only able to hint at the overall

[1]This chapter previously published as Sarmento et al. (2017).

progression of early metal enrichment.

Similarly, searches for individual Pop III stars in the Milky Way (MW) halo have yielded only indirect clues as to the Pop III/Pop II transition. Even the most pristine stars observed have a substantial mass fraction of metals (Christlieb et al., 2002; Cayrel et al., 2004; Aoki et al., 2006; Frebel et al., 2005; Norris et al., 2007; Caffau et al., 2011; Keller et al., 2014; Howes et al., 2015), even though theoretical studies suggest that metal-free stars should have already been observed if they had masses low enough to survive to the present-day (Scannapieco et al., 2006; Tumlinson, 2006; Brook et al., 2007; Salvadori et al., 2010; Hartwig et al., 2015; Ishiyama et al., 2016). On the other hand, low-temperature cooling is extremely inefficient without dust and metals, and pristine gas would have been much less susceptible to fragmentation, forming individual $\approx 10^3 M_\odot$ stars, (Hutchins, 1976; Abel et al., 2002; Bromm et al., 2002; Bromm & Loeb, 2003) or single or binary $10 - 100 M_\odot$ stars with very short lifetimes (e.g. Johnson & Bromm, 2006; Padoan et al., 2007; McKee & Tan, 2008; Turk et al., 2009; Stacy et al., 2010; Clark et al., 2011; Hosokawa et al., 2011; Greif et al., 2012; Hirano et al., 2014).

Theoretically, the key process determining the Pop III/Pop II transition is the turbulent mixing of heavy elements to pollute the medium above the critical metallicity, $Z_{\rm crit}$, that marks the shift to lower-mass star formation. This evolution is dependent on two important issues. The first is the uncertain value of $Z_{\rm crit}$, which is expected to be between 10^{-6} and $10^{-3} Z_\odot$, depending on whether low-metallicity cooling is dominated by dust emission or by the fine-structure lines of carbon and oxygen (Schneider et al., 2003; Bromm & Loeb, 2003; Omukai et al., 2005). The second issue is the rate at which the gas within the galaxy can be polluted above $Z_{\rm crit}$ by the turbulent mixing of heavy elements (Pan & Scalo, 2007; Greif et al., 2010; Pan et al., 2012, 2013; Bromm, 2013, 2014; Ritter et al., 2015). Here the key quantity is the evolution

of the pristine gas fraction, the fraction of material with metal concentration below $Z_{\rm crit}$ as a function of time and space. Clearly the behavior of this quantity depends both on the rate at which stars deposit new metals into the surrounding medium and also on how gravity and large-scale motions act to move metals between different regions within that medium. However, the evolution of the pristine gas fraction is also highly dependent on a third process: the small-scale turbulent mixing of metals within a given region of initially pristine gas.

This last process is particularly difficult to model in cosmological simulations, due to the enormous range of physical scales required to capture it properly. Estimating the diffusivity of the ionized medium as the Spitzer-Braginskii value (Spitzer, 1956)

$$\nu_{\rm spitzer} = \frac{6.0 \times 10^{-17} (T/{\rm K})^{5/2}}{(\rho/{\rm g/cm^{-3}})} {\rm cm^2 s^{-1}}, \tag{2.1}$$

gives $L_{\rm diss} \approx \nu_{\rm spitzer}/c_s \approx 10^{-3}\, T_4^2\, n_{-3}^{-1}\, {\rm pc}$ where T_4 is temperature in units of 10^4 K and n_{-3} is the number density in units of 10^{-3} cm^{-3}, which is the mean density at $z \approx 15$. On the other hand, the maximum comoving resolution of modern large-scale cosmological simulations is $\approx 10 - 1000$ pc (e.g. Richardson et al., 2013; Kim et al., 2014; Vogelsberger et al., 2014; O'Shea et al., 2015; Schaye et al., 2015; Dubois et al., 2014).

Given the mismatch between these spatial scales, thorough mixing of pollutants at the scale of individual resolution elements is expected to take several eddy turnover times, (Pan et al., 2013; Ritter et al., 2015) corresponding to a significant number of simulation time steps. However, most simulations instantaneously update the affected cells' average metallicity once they are contaminated with SN ejecta. In other words, because such cells may have a relatively high average metallicity immediately after a local SN event, they are usually assumed to be fully polluted to above the critical metallicity, even though in reality their mass fraction, P, of unpolluted, pristine gas

remains large until these metals are well mixed.

In this work, we develop and apply a subgrid model that explicitly tracks the pristine gas fraction, P, within every zone in a cosmological simulation. Our model is built on standard techniques for estimating unresolved turbulent velocities and the results of both theoretical modeling and high-resolution simulations of the pollution of pristine gas in fully developed turbulence, as described in Pan et al. (2013, hereafter PS13) (see also Pan et al., 2012). The model is implemented within the cosmological adaptive mesh refinement (AMR) code RAMSES (Teyssier, 2002) which also includes models for star formation and metal generation/dispersal by SNe. All quantities that include an overbar indicate cell or star-particle-averaged qualities. Hence, the average metallicity of a simulation cell is denoted $\overline{Z}$ while quantities including the *star* subscript (e.g., $\overline{Z_\star}$) refer to values associated with simulated star particles. We also add another scalar quantity, $\overline{Z_{\rm P}}$, to the code ,which tracks the metallicity due only to metal-free stars (here, the subscript P is short for 'primordial metals'). When star particles are formed within a given cell, they inherit not only the total metallicity $\overline{Z}$, but also P and $\overline{Z_{\rm P}}$, from the gas. This allows us to calculate the fraction of stars in a given star particle that are metal-free, $P_\star$, as well as the relative contributions that metals from Pop III and Pop II stars make to the stars that are enriched, $\overline{Z_{{\rm P},\star}}/\overline{Z_\star}$.

These values remained locked into the stellar populations for all times, and can be compared with observations of MW Halo stars with very low metallicities. We directly compare our simulation results with observations of the metallicity distribution function of MW halo stars, and show that accounting for $P_\star$ is essential for making such comparisons reliably. In addition, knowledge of $\overline{Z_{{\rm P},\star}}/\overline{Z_\star}$ allows us to investigate the idea that stars formed in gas enriched only by Pop III stars are likely to be carbon-enhanced and especially iron-poor (Umeda & Nomoto, 2003; Keller et al., 2014; Hansen et al., 2016).

The structure of this work is as follows. In §2 we describe our methods, including both our implementation of the subgrid model of metal pollution and our RAMSES modeling of the overall evolution of cosmological objects and the formation of star particles within them. In §3 we describe our results, focusing on comparisons between the properties of our final stellar distributions and observations of metal-poor stars in the MW Halo. Conclusions are given in §4. Throughout this paper, we adopt the following cosmological parameters: $\Omega_{\rm M} = 0.267$, $\Omega_\Lambda = 0.733$, $\Omega_{\rm b} = 0.0449$, $h = 0.71$, $\sigma_8 = 0.801$, and $n = 0.96$, where $\Omega_{\rm M}$, Ω_Λ, $\Omega_{\rm b}$ are the total matter, vacuum, and baryonic densities, in units of the critical density, h is the Hubble constant in units of 100 km/s, σ_8 is the variance of linear fluctuations on the 8 h^{-1} Mpc scale, and n is the "tilt" of the primordial power spectrum (Larson et al., 2011).

2.2 Methods

2.2.1 Primordial Metallicity and Pristine Gas Fraction

Our study makes use of RAMSES (Teyssier, 2002), a cosmological AMR code, which uses an unsplit second-order Godunov scheme for evolving the Euler equations. RAMSES variables are cell centered and interpolated to the cell faces for flux calculations, which are then used by a Harten-Lax-van Leer-Contact Riemann solver (van Leer, 1979; Einfeldt, 1988). Self-gravity is solved using the multigrid method (Guillet & Teyssier, 2011) for all coarse levels in the simulation, and the conjugate gradient method is used for levels ≥ 11. The code is capable of advecting any number of scalar quantities, defined as mass fractions, in each simulation cell. For example, the standard version of RAMSES evolves a mass fraction of metals for each cell, which may have contributions from Pop III stars and second-generation stars, referred to as total average metallicity $\overline{Z}$. As a simulation evolves, RAMSES creates star particles

in regions of overdense gas, each of which represents hundreds to thousands of solar masses of individual stars. Like the gas, each such star particle is tagged with a $\overline{Z_\star}$ value, representing the average metallicity of the medium from which it was born.

We use these capabilities to generate and track new metallicity-related quantities for both the gas and star particles. For the gas, we introduce two new scalars: the average *primordial metallicity*, $\overline{Z_{\rm P}}$ and the *pristine gas mass fraction*, P. The primordial metallicity scalar, $\overline{Z_{\rm P}}$, tracks the mass fraction of metals generated by Pop III stars, which are likely to have nonsolar abundance ratios (Heger & Woosley, 2002; Umeda & Nomoto, 2003; Ishigaki et al., 2014). Our pristine gas fraction scalar models the mass fraction of gas with $Z < Z_{\rm crit}$ which allows us to track the process of metal mixing within each cell. While a cell may have a relatively high average metallicity, $\overline{Z}$, those metals are normally not well mixed throughout its volume at the time of injection. By tracking P, we can quantify the amount of pristine gas in such cells ($P \approx 1.0$) even if their mean metallicities are large.

Since we are primarily interested in the characteristics of stellar populations, we also track the pristine fraction and the primordial metallicity of each star particle ($P_\star$ and $\overline{Z_{{\rm P},\star}}$ respectively). These values are adopted for each star particle from the gas in which it was formed. For example, a star particle born in a region of gas with $P = 0.5$ inherits $P_\star = 0.5$ and represents a stellar population containing 50% pristine (Pop III) stars and 50% polluted stars, by mass. As $P_\star$ is known for each star particle, when a star enriches the surrounding medium through SNe, we can determine the fraction of Pop III SN ejecta contributed, allowing us to track the primordial metallicity contributed by these stars. As such we are able to track the pollution of surrounding cells not only in terms of $\overline{Z}$ and P, but also in terms of the cells' primordial metals, $\overline{Z_{\rm P}}$. As discussed in detail below, this allows us to connect assumptions about the yields from Pop III stars with observations of carbon-enhanced metal-poor (CEMP-

no) stars (Beers & Christlieb, 2005; Hansen et al., 2016; Yoon et al., 2016), which are defined as having [C/Fe] $> +0.7$ and [Ba/Fe] < 0.0 (Beers & Christlieb, 2005) . While Cooke & Madau (2014) and Sluder et al. (2016) attribute the abundances in CEMP stars to primordial, faint SNe and anisotropic ejecta, respectively, our method depends only on mixing and the abundance patterns of Pop III SNe.

By knowing the average metallicity, $\overline{Z}$, and the pristine gas fraction, P, we can better model the metallicity of the polluted fraction of gas (or stars). Since $\overline{Z}$ represents the average metallicity of a parcel of gas and the polluted fraction, $f_{\rm pol} \equiv 1 - P$, models the fraction of gas that is actually polluted with metals, we can use the value of $f_{\rm pol}$ to predict the enhanced metallicity ($Z > \overline{Z}$) of the polluted fraction of gas in each simulation cell. This allows us to more accurately model the metallicity of the star particles created from this gas.

However, our new scalar only indicates that the pristine fraction of the cell contains gas with $Z < Z_{\rm crit}$. When considering primordial cells we know that the pristine gas has $Z \approx 0$ and hence the polluted fraction, $f_{\rm pol}$, accounts for all of the metals in the cell. In this case we can use $f_{\rm pol}$ to precisely determine the enhanced metallicity of the polluted fraction of gas:

$$Z \equiv \frac{\overline{Z}}{f_{\rm pol}}, \tag{2.2}$$

where Z is the enhanced metallicity of the polluted fraction of gas.

For instance, consider an initially primordial parcel of gas that is enriched, on average, to $\overline{Z} = 10^{-1}\, Z_{\odot}$ with $P = 0.9 \implies f_{\rm pol} = 0.1$ by a nearby SN event. The fraction of stars subsequently produced from such gas will, ignoring possible differences in the star-forming efficiency between metal-free and polluted gas, be 90% pristine and 10% polluted. However, the metallicity of the polluted stars will be $10\times$ greater than the average metallicity since all of the metals in the cell are currently

concentrated in 10% of its volume. Thus, in this case, we can simply correct the metallicity of star particles born in the gas by taking into account the polluted fraction of gas as described by equation (2.2).

However, once mixing has reduced $P < 1.0$ with $\overline{Z} > Z_{\rm crit}$ it becomes possible for the average metallicity of a cell to fall to $\overline{Z} < Z_{\rm crit}$ either via the advection of either pristine material from neighboring cells or via the movement of material with a lower average metallicity into the cell. Such cells' pristine fractions evolve back toward unity since mixing now dilutes areas with $Z > Z_{\rm crit}$ until the entire cell has $P = 1.0$ and $\overline{Z} = Z < Z_{\rm crit}$ throughout the cell. Now subsequent injections of pollutants can once again raise $\overline{Z} > Z_{\rm crit}$, but in this case not all of the metals are concentrated in the incoming pollutants.

Our scalar P does not encode the metallicity of the pristine gas: the scalar only captures the fraction of gas with $Z < Z_{\rm crit}$ and as such we do not know the fraction of metals, captured in the scalar $\overline{Z}$, that are distributed in the pristine fraction of gas. However, we can bound this value since we know that the metallicity of the polluted and pristine fractions of the gas must sum to the average metallicity of the cell. Equation (2.3) solves for the metallicity of the polluted fraction of gas, Z, when considering that the pristine fraction has an unknown metallicity $Z_{\mathbb{P}}$:

$$\begin{aligned} \overline{Z} &= Z(1-P) + Z_{\mathbb{P}}P, \\ Z &= \frac{\overline{Z} - Z_{\mathbb{P}}P}{(1-P)}. \end{aligned} \tag{2.3}$$

It can be seen that when $Z_{\mathbb{P}} = 0$ we recover $Z = \overline{Z}/f_{\rm pol}$, the enhanced metallicity of a polluted volume of gas within a primordial cell. This correction is the upper bound for the metallicity of the polluted fraction. We can also establish a lower bound for the polluted fraction's metallicity correction by considering the definition of the pristine fraction, namely, that $Z_{\mathbb{P}} < Z_{\rm crit}$. Substituting for $Z_{\mathbb{P}}$ this means that

$$Z = \frac{\overline{Z} - Z_{\rm crit} P}{(1-P)}, \tag{2.4}$$

is a lower bound on the correction to the metallicity of the polluted fraction. Comparing the lower and upper bounds of the correction to the metallicity of the polluted fraction, we see that the term $Z_{\rm crit} P$ will have the largest effect when $\overline{Z} \approx Z_{\rm crit}$ and $P \approx 1$. This is depicted in Figure 2.1.

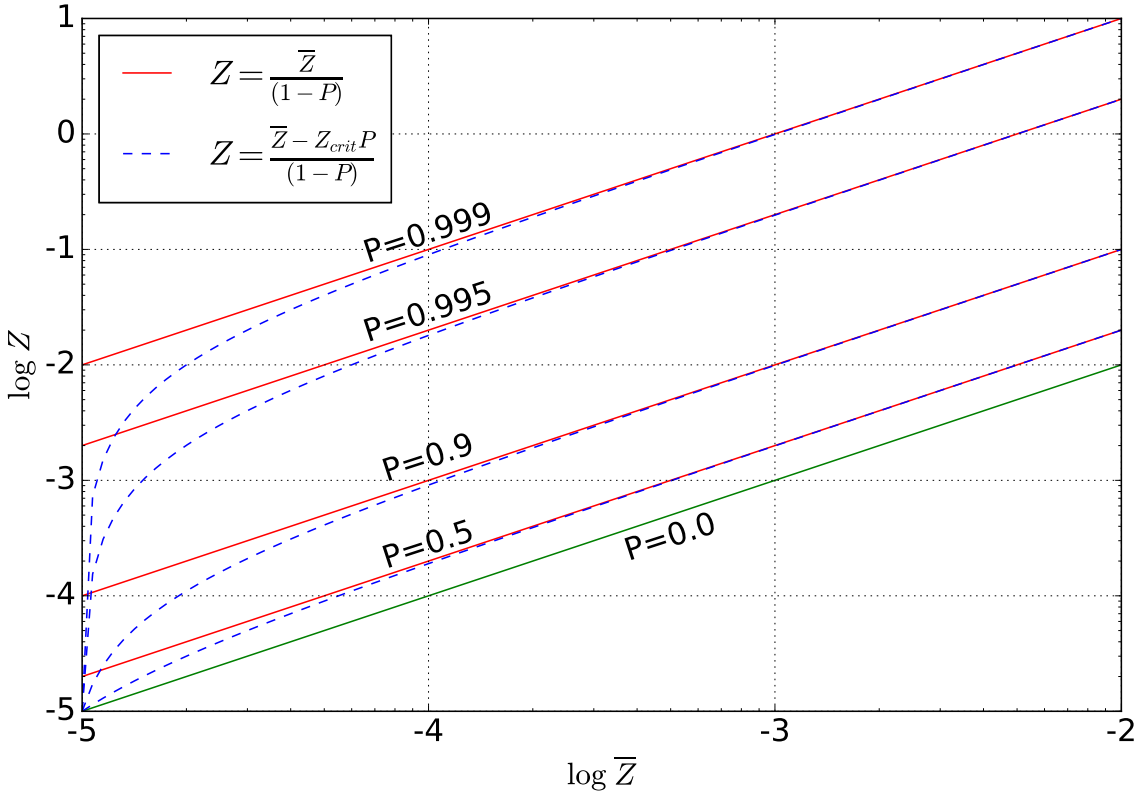

Figure 2.1: Curves depicting the lower and upper bounds for the corrected metallicity, Z, of the polluted region of gas over a range of average cell metallicities, $\overline{Z}$. The corrected metallicity will fall on the solid red (or green) line when the pristine fraction of gas has $Z = 0$. As the metallicity of the pristine fraction moves to $Z \rightarrow Z_{\rm crit}$ the corrected metallicity moves toward the dotted blue line. The largest difference between the two corrections occurs at small polluted fractions, where pollutants are concentrated in a small volume, at low $\overline{Z}$.

The pristine gas fraction, P, is initialized to 1.0 for all cells in the simulation.

Table 2.1: Notation

Symbol	Definition
P, $P_\star$	The mass fraction of gas (star particles) with $Z < Z_{\rm crit}$.
$f_{\rm pol}$	The mass fraction of gas or star particles with $Z \geq Z_{\rm crit}$. $f_{\rm pol} \equiv 1 - P$.
$Z_{\mathbb{P}}$	The metallicity of the pristine fraction of gas or star particle; while undetermined, it is bounded by $0 \leq Z_{\mathbb{P}} \leq Z_{\rm crit}$.
$\overline{Z}$, $\overline{Z_{\rm P}}$, $\overline{Z_\star}$, $\overline{Z_{\rm P,\star}}$	The average metallicity (primordial metallicity) within an unmixed volume of gas (or star particle).
Z, $Z_{\rm P}$ $Z_\star$, $Z_{\rm P,\star}$	The corrected and assumed homogeneous metallicity (primordial metallicity) of the polluted fraction of gas (or star particle).

As the first stars are formed and go SNe, metal-rich ejecta, along with entrained gas from the cell, is immediately carried into neighboring cells, where it increases the cell density from $\rho_{\rm cell}$ to $\rho_{\rm cell} + \rho_{\rm ejecta}$. This decreases the cell's pristine gas fraction from 1.0 to $P = \rho_{\rm cell}/(\rho_{\rm cell} + \rho_{\rm ejecta})$ starting the decay of P. We note that this method of computing the change to P assumes that the ejecta (with density $\rho_{\rm ejecta}$) is well mixed. The subgrid mixing algorithm is then invoked for each cell at each time-step, resulting in the decay of the pristine gas fraction (based on theoretical modeling of the pristine fraction with physical parameters calibrated by numerical simulations, as described below) for all cells where $P < 1.0$.

Finally, we note that star formation is likely to be more efficient in polluted gas, due to more efficient cooling. However, given the uncertainties in the Pop III initial mass function (IMF) we have elected to weigh star formation rates in pristine and polluted gas only by the pristine gas fraction. For example, stars born in gas with $P = 0.9$ give rise to star particles with $P_\star = 0.9$ meaning 90% of the mass of the star particle represents Pop III stars. Below we include Table 2.1 clarifying the notation used to describe the scalars we reference throughout this paper.

2.2.2 Subgrid Model for the Pollution of Pristine Gas

Self-Convolution Model

The novelty of our approach is in how the pollution of pristine gas is modeled on subgrid scales. Here we rely on the work described in PS13, which determined that in fully developed turbulence, the pollution rate can be modeled by a relatively simple self-convolution model. While SN forcing is intuitively compressive, P13 used solenoidal forcing to drive turbulence. However, studies by Federrath et al. (2010) and Padoan et al. (2016) demonstrate that SN driving forces are not purely compressive. Indeed, the effective SN driving force may possibly be more solenoidal than compressive with a compressive-to-solenoidal ratio below one, due to the non-sphericity of the SN blast which tends to be clumpy in both velocity and density space. Additionally, each 'SN' in our simulation represents the combined energy of several SN since each star particle represents a Salpeter IMF with a total mass in the range $726 - 3628\,M_{\odot}$. These considerations conspire to make the ISM highly turbulent. While compressive forcing is surely a part of SN-driven turbulence, results from simulations using solenoidally driven turbulence are a reasonable approximation when determining the mixing timescales for SN-driven turbulence.

There has been compelling evidence that in a turbulent medium, the dominant scalar structures at small scales are two-dimensional sheets or edges (e.g. Pan & Scannapieco, 2011), and the rate at which these sheets are produced is determined mainly by the turbulent stretching rate at large length scales. With time, the sheets become thinner, and once their thickness is sufficiently small for molecular diffusivity to efficiently operate, neighboring sheets are homogenized, leading to a reduction in the width of the local metallicity probability distribution function, $\Phi(Z;t)$.

The evolution of $\Phi(Z;t)$ within a turbulent region in this physical picture can be

approximately described as

$$\frac{\partial \Phi(Z;t)}{\partial t} = s(t) \left[-\Phi(Z;t) + \int_0^1 dZ_1 \Phi(Z_1;t) \times \int_0^1 dZ_2 \Phi(Z_2;t) \times \delta \left(Z - \frac{Z_1 + Z_2}{2} \right) \right], \tag{2.5}$$

where $s(t)$ is the turbulent stretching rate that controls the rate at which the probability density function (PDF) convolution proceeds (Curl, 1963; Dopazo, 1979; Janicka et al., 1979). Extending this model, Venaille & Sommeria (2007) developed a "continuous" version, which essentially assumes that the convolution occurs everywhere in the flow at any given time, but in an infinitesimal time, Δt, the number of convolutions is infinitesimal and equal to $\epsilon = s(t)\Delta t$. Duplat & Villermaux (2008) then generalized this even further, including a parameter n such that a fraction $n\epsilon$ of the flow experiences mixing events during a time interval, Δt, and the number of convolutions in this fraction of the flow is $1/n$. In this model, n characterizes the degree of spatial locality of the PDF convolution, with larger values of n corresponding to more global convolutions. The models of Curl (1963) and Venaille & Sommeria (2007) correspond to $n = 1$ and $n \to \infty$, respectively.

By integrating $\Phi(Z;t)$ from a finite but extremely small value up to the critical metallicity, the Duplat & Villermaux (2008) model can be used to derive a very simple equation for the evolution of the $Z < Z_{\rm crit}$ pristine fraction:

$$\frac{dP}{dt} = -\frac{n}{\tau_{con}} P(1 - P^{1/n}). \tag{2.6}$$

The $n = 1$ case of this equation was first given in Pan & Scalo (2007). This equation traces the evolution of P as a function of n and a timescale τ_{con}, and these parameters, in turn, are functions of the turbulent Mach number, M, and the average metallicity of the cell relative to the critical metallicity, $\overline{Z}/Z_{\rm crit}$ (Pan et al., 2012, PS13).

Note that equation (2.6) has the property that if $P = 1$ then $\dot{P} = 0$ ensuring that pristine cells remain pristine. There are no metals in such a cell with which to pollute it. As soon as the injection of polluted material causes $P < 1.0$ however, the polluted fraction will then continue to decrease. Including the cell-to-cell advection handled by RAMSES and the addition of enriched ejecta material to a cell, the full equation for the evolution of P is

$$\frac{\partial(\rho P)}{\partial t} + \nabla \cdot (\mathbf{u}\,\rho\,P) = -\frac{n}{\tau_{con}}\rho P(1 - P^{1/n}) - \dot{\rho}_{\rm ej} P, \tag{2.7}$$

where ρ and $\mathbf{u}$ are the local density and velocity, and $\dot{\rho}_{\rm ej}$ is the rate that the density of cell is increased by the addition of ejecta. The reader may notice that we have omitted the diffusion term described by PS13 (equation (49) in that work). We have not tried to characterize the numerical diffusion inherent in RAMSES and a proper treatment would need to account for any difference between it and the diffusion term in PS13 when computing cell-to-cell diffusion. We leave this for a future work.

Locality Parameter and Convolution Timescale

The evolution of P described in Eqs. (2.6) and (2.7) depends on a convolution timescale, τ_{con} and the parameter n, which quantifies the locality of mixing. Here we are interested in the case in which the driving scale of the turbulence and the length scale at which pollutants are added to the medium (referred to as L_f and L_p in PS13) both occur on the grid scale Δx. In this case, as shown in PS13, the locality parameter as a function of Mach number is well fit by

$$n = 1 + 11\,\exp\left(-\frac{M}{3.5}\right). \tag{2.8}$$

This means that in subsonic turbulence, pollution is more of a global process, corresponding to $n \approx 12$, and in highly supersonic turbulence pollution is more local, corresponding to $n \approx 1$, the n value in Curl's original model.

Also following PS13, we model the dynamical mixing time as

$$\tau_{con} = \frac{\Delta x}{v_t} \begin{cases} \tilde{\tau}_{con1} & \text{if } P \geq 0.9 \\ \\ \tilde{\tau}_{con2} & \text{if } P < 0.9 \end{cases}, \tag{2.9}$$

where v_t is the turbulent velocity of the cell, and $\tilde{\tau}_{con1}$ and $\tilde{\tau}_{con2}$ account for the slightly less efficient mixing that occurs at low pollution fractions (PS13). Unlike n, these timescales depend not only on the Mach number but also on the ratio of the average metallicity in the turbulent region to the critical metallicity. For example, if the mean metallicity in the region is less than the critical metallicity, then the fraction of pristine material cannot monotonically decrease since complete mixing with $\overline{Z} < Z_{\rm crit}$ should imply $P = 1.0$. On the other hand, as PS13 were concerned only with cases in which the mean metallicity in the medium was much greater than the critical metallicity, their fits to the convolution timescale show only a weak dependence on $\overline{Z}/Z_{\rm crit}$. Using an extrapolation of the dependence $\overline{Z}/Z_{\rm crit}$ given in PS13 for $\overline{Z}/Z_{\rm crit} < 1.0$ results in P always decreasing – even when the average metallicity is subcritical.

Thus, we refit the dependence of $\tilde{\tau}_{con1}$, $\tilde{\tau}_{con2}$ on $\overline{Z}/Z_{\rm crit}$ working with the results of the PS13 data over a much larger range of values. Figure 2.2 depicts the normalized convolution timescale as a function of $\overline{Z}$ for the range of turbulent flows studied by PS13. For convenience we normalize to its value when $Z_{\rm crit} = 10^{-7}\,\overline{Z}$ as this value was used in the fits presented in PS13. As expected, the mixing time increases exponentially as $\overline{Z}$ approaches $Z_{\rm crit}$. As the critical metallicity in the simulations in PS13 was taken to be 10^{-7} of the mean metallicity, we define our fits in terms of the ratio

$$x \equiv -\log_{10}\left(\frac{\overline{Z}}{10^7 Z_{\rm crit}}\right)\left[\log_{10}\left(\frac{\overline{Z}}{Z_{\rm crit}}\right)\right]^{-1}, \tag{2.10}$$

which equals zero when $\overline{Z}/Z_{\rm crit} = 10^7$ and approaches infinity as $\overline{Z}/Z_{\rm crit}$ drops to 1.

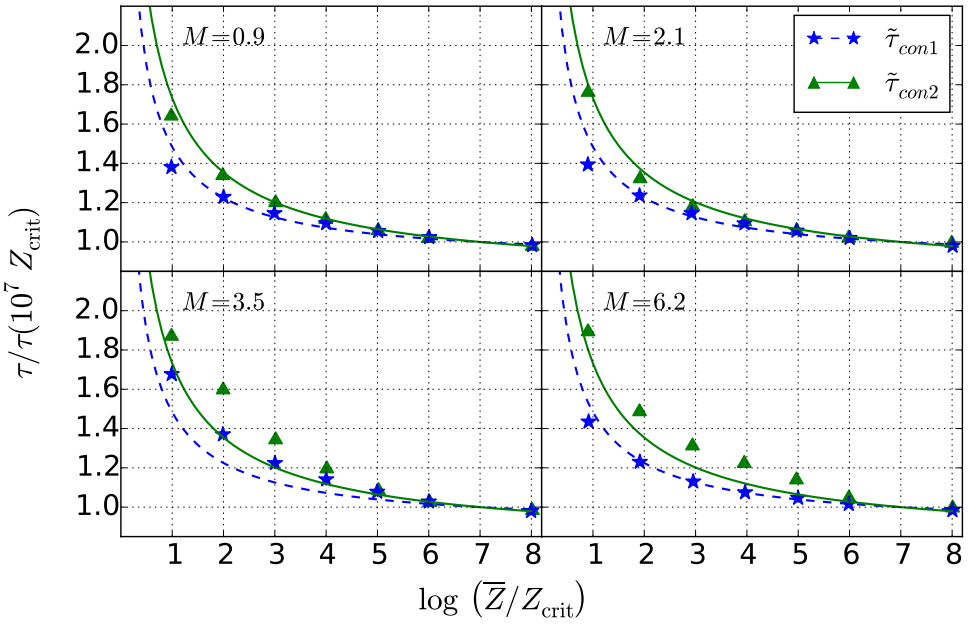

Figure 2.2: Our analytic fits to the dynamical mixing times (*triangles* and *stars*) as determined by PS13. Time scale $\tilde{\tau}_{\rm con1}$ is used when $P \geq 0.9$, $\tilde{\tau}_{\rm con2}$ is used otherwise. For this plot, the mixing time is normalized to the mixing time for region with $Z_{\rm crit} = 10^{-7}\,\overline{Z}$. Note that as $\overline{Z} \rightarrow Z_{\rm crit}$ the mixing time becomes exponentially longer, going to infinity when $\overline{Z} < Z_{\rm crit}$.

We then obtained a simple fit to the PS13 simulation results as

$$\begin{aligned} \tilde{\tau}_{con1} &= \left[0.225 - 0.055\ \exp\left(-\frac{M^{3/2}}{4}\right)\right]\ \sqrt{\frac{x}{5}+1}, \\ \tilde{\tau}_{con2} &= \left[0.335 - 0.095\ \exp\left(-\frac{M^{2}}{4}\right)\right]\ \sqrt{\frac{x}{3}+1}, \end{aligned} \tag{2.11}$$

if $\overline{Z}/Z_{\rm crit} > 1$ and $\tau_{con} = \infty$ if $\overline{Z}/Z_{\rm crit} \leq 1$. It is possible for a region with $\overline{Z} > Z_{\rm crit}$ to evolve back to $\overline{Z} \leq Z_{\rm crit}$ due to the advection of highly pristine material from nearby cells. In this case we think of mixing as making the cell more pristine, rather than less, and evolve the pristine gas fraction back toward 1 as an exponential function of the cell's turbulent velocity:

$$\frac{d}{dt}(1-P) = -(1-P)\frac{v_t}{\Delta x}. \tag{2.12}$$

We note that the pristine fraction does not always evolve toward 1 immediately once $\overline{Z} < Z_{\rm crit}$. For example, if the polluted fraction in a cell is below $\overline{Z}/Z_{\rm crit}$, the

average metallicity in the polluted region is still above $Z_{\rm crit}$, and thus the pristine fraction in the cell would still be decreasing as the polluted region mixes with more ambient pristine gas. Roughly speaking, only after the polluted fraction in a cell exceeds $\overline{Z}/Z_{\rm crit}$, does the pristine fraction start to evolve toward 1. However, accounting for this complexity by checking whether the polluted fraction in a cell is above or below $\overline{Z}/Z_{\rm crit}$ does not cause a significant difference from the results using equation (2.12) immediately (when the average metallicity in a cell drops below $Z_{\rm crit}$). We will therefore focus on results from equation (2.12).

All the fits above depend on the cells' turbulent velocity, v_t and its ratio to the local sound speed, $M = v_t/c_s$. This velocity can be estimated in turn as $v_{\rm t} = \nu_{\rm t}/\Delta x$, where $\nu_{\rm t}$ is the turbulent kinematic eddy viscosity of the scale of the cell, or as $v_{\rm t} = \sqrt{2K}$ where K is the subgrid kinetic energy. Many possible models exist in the literature for the estimate of v_t (e.g. Yoshizawa, 1986; Moin et al., 1991; Erlebacher et al., 1992; Vreman et al., 1997) or K (e.g. Schumann, 1975; Moeng, 1984; Ghosal et al., 1995; Schmidt et al., 2006; Genin & Menon, 2010; Scannapieco & Brüggen, 2010; Chai & Mahesh, 2012). While a comparison between different approaches merits further study, here we adopt the simplest approach, making use of the eddy viscosity model of Smagorinsky (1963). A brief overview of the approach used to compute v_t follows.

We first compute the numerical velocity gradients across each cell $\Delta_{\rm i} v_{\rm j}$ to determine the local rate-of-strain tensor

$$\mathcal{S}_{\rm ij} \equiv \frac{1}{2}(\Delta_{\rm i} v_{\rm j} + \Delta_{\rm j} v_{\rm i}), \tag{2.13}$$

which captures the 3D velocity shear around each cell (Sur et al., 2014). Starting with the energy in the Kolmogorov inertial spectrum ($\epsilon^{2/3} k^{-5/3}$), and equating it to the loss of kinetic energy in the flow, $2\nu\langle \mathcal{S}_{ij}\mathcal{S}_{ij}\rangle$, we have the following:

$$2\nu\langle \mathcal{S}_{ij}\mathcal{S}_{ij}\rangle = 2\epsilon^{2/3}\int_0^{1/\Delta x} k^2\, k^{-5/3} dk \propto \epsilon^{2/3}\Delta x^{-4/3}, \tag{2.14}$$

where we have summed the energy spectrum (in k-space) up to the size of the filter scale to capture the sub-grid energy. Noting that $\epsilon \propto v_t^3/\Delta x$, results in

$$v_t \propto \sqrt{\nu}\ |\overline{\mathcal{S}_{ij}}|\ \Delta x, \tag{2.15}$$

demonstrating that the amplitude of velocity fluctuations on the filter scale is directly related to the magnitude of the rate of strain, as adopted in our simulation and by Smagorinsky: $v_t = |\overline{\mathcal{S}_{ij}}|\ \Delta x$.

2.2.3 Molecular Cooling

Beyond the subgrid model for the pollution of pristine gas described above, we have also modified RAMSES to include a simple molecular cooling model which is important for low-temperature cooling in the pristine gas (Johnson & Bromm, 2006; Prieto et al., 2008; Hirano & Yoshida, 2013). Our model is analytic and based on the work of Martin et al. (1996), which provides a radiative cooling rate per H_2 molecule, Λ_r/n_{H_2}, across a range of densities, as depicted in Fig. 2.3. We truncate our H_2 cooling model above 50,000 K as the contribution of molecular cooling becomes negligible and molecular hydrogen is highly dissociated above this temperature.

The cooling rate is computed for each simulation cell based on the cell's density, temperature, and molecular fraction, $f_{\mathrm{H_2}}$. Our initial H_2 fraction is primordial ($f_{\mathrm{H_2}} = 10^{-6}$; Reed et al., 2005), we model the Lyman-Werner flux from our star particles as $\eta_{\mathrm{LW}} = 10^4$ photons per stellar baryon (Greif & Bromm, 2006) and we assume optically thin gas throughout the simulation volume. We compute the number of stellar baryons, $N_{*,b}$, by totaling the mass in star particles, at each simulation step, assuming a near-primordial composition (X=0.73, Y=0.25). This results in an updated $f_{\mathrm{H_2}}$ for each simulation step:

$$f_{H_2,new} = \frac{(f_{H_2,old}\, N_{gas} - N_{\rm LW})}{N_{gas}}, \tag{2.16}$$

where

$$N_{\rm LW} = N_{*,b}\, \eta_{\rm LW}. \tag{2.17}$$

We note that the total stellar mass created at the onset of star formation generates enough Lyman-Werner flux to permeate our simulation volume of 27 $\mathrm{Mpc}^3\ \mathrm{h}^{-3}$ (Johnson et al., 2013; Bromm & Loeb, 2003), destroying all of the molecular hydrogen. We do not model subsequent H_2 formation since cooling becomes dominated by metal lines shortly after the first star particles form and any subsequent molecular hydrogen would be quickly destroyed by the Lyman-Werner flux. Hence, our molecular cooling model is significant only for the very first generation of stars.

Metal-line cooling is computed as a function of gas metallicity and temperature using Sutherland & Dopita (1993) for temperatures down to $\approx 10^4\, K$ below which RAMSES makes use of Rosen & Bregman (1995). We fix the gas temperature floor at 100 K for radiative cooling although adiabatic cooling below this limit is possible. Lastly, our UV background is based on the work of Haardt & Madau (1996).

2.2.4 Star Formation and SN Generation

Following the cosmic evolution of pristine gas is sensitive to our implementation of star formation and SN generation. RAMSES creates star particles in regions of gas according to a Schmidt law (Schmidt, 1959), as

$$\frac{d\rho_\star}{dt} = \frac{\rho}{t_\star}\theta(\rho - \rho_{\rm th}), \tag{2.18}$$

where the Heaviside step function $\theta(\rho - \rho_{th})$ allows for star formation only when the density exceeds a threshold value ρ_{th}. Here we have set $\rho_{\rm th}$ to be the maximum

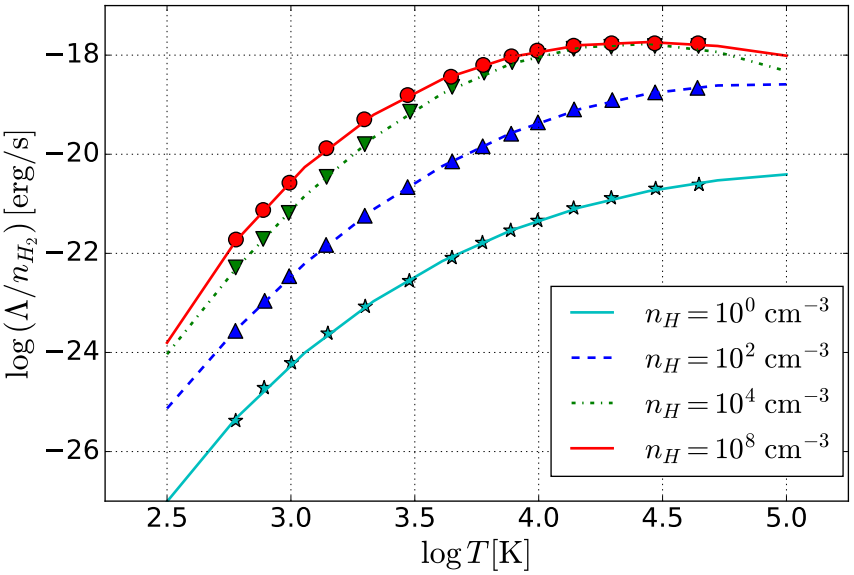

Figure 2.3: Cooling per H_2 molecule. Data points are from Martin et al. (1996). The curves are our analytic fits and are used in the code.

of $0.75\,m_p\,\mathrm{cm}^{-3}$ and 150 times the mean density in the simulation, where the latter criterion ensures that star particles are only formed in virialized halos and not in high-density regions of the cosmological flow (Rasera & Teyssier, 2006; Dubois & Teyssier, 2008). To generate an SFR in $M_\odot\,\mathrm{yr}^{-1}$ in good agreement with Madau & Dickinson (2014) and Bouwens et al. (2012b), we have tuned the star formation time scale $t_\star = 0.316$ Gyr, approximately 5 times the free fall time, $t_{ff} \equiv (3\pi/32G\rho)^{1/2}$, for a gas with $\rho = 0.75\,m_p\,\mathrm{cm}^{-3}$. The mass of the newly created star particle is $m_\star = \rho_{th}\Delta x_{min}^3 N$, where Δx_{min} is the best resolution cell size and N is drawn from a Poisson distribution

$$P(N) = \frac{\overline{N}}{N!}\,\exp(-\overline{N}), \tag{2.19}$$

with

$$\overline{N} = \frac{\rho\,\Delta x^3}{\rho_{th}\Delta x_{\mathrm{min}}^3}\frac{\Delta t}{t_\star}. \tag{2.20}$$

A further limitation on star particle formulation is that no more than 90% of the cell's gas mass can be converted into stars.

As each star particle represents a mass range of stars, a fraction of the mass will be returned to the grid in the form of SN. In our simulations, this recycling is assumed to occur after the 10 Myr lifetimes for stars near the top of the IMF (e.g. Raskin et al., 2008). In this case the impact of massive stars is determined by the fraction of the star particle mass they eject, η_{SN}, and the kinetic energy per unit mass of this ejecta, $E_{\rm SN}$. For simplicity, we take $\eta_{\rm SN} = 0.1$ and $E_{SN} = 1 \times 10^{51}\, ergs/10\, M_{\odot}$, for all stars formed throughout the simulation, regardless of their primordial fractions. Note however that as the Pop III IMF is likely to have been biased to massive stars, metal ejection from such stars may have been more efficient (e.g. Scannapieco et al., 2003; Scannapieco, 2005), leading to differences in stellar enrichment which we plan to explore in future work.

For each newly formed star particle, the ejected mass and energy are deposited into all cells whose centers are within 150 pc and if the size of the cell containing the particle is greater than 150 pc, the energy and ejecta are deposed into the adjacent cells (Dubois & Teyssier, 2008). Here the total mass of the ejecta is that of the stellar material plus an amount of the gas within the cell hosting the star particle (*entrained gas*) such that $m_{\rm ej} = m_{sn} + m_{ent}$, with $m_{\rm sn} \equiv \eta_{sn}\, m_{\star}$ and $m_{ent} \equiv {\rm m}in(10\, m_{sn},\ 0.25\, \rho_{\rm cell}\, \Delta x^3)$. Similarly, the mass in metals added to the simulation is taken to be 15% of the SN ejecta plus the metals in the entrained material, $Z_{\rm ej}\ m_{\rm ej} = m_{\rm ent}\, Z + 0.15\, m_{\rm sn}$, and the mass in primordial metals is taken to be $Z_{{\rm P},ej}\, m_{\rm ej} = m_{\rm ent}\, Z_{\rm P} + 0.15\, m_{\rm sn}\, P_{\star}$. SN energy is the dominate driver of turbulence in our simulation and we have chosen to partition it equally between kinetic and thermal energy. Lastly, we note that we do not model black hole formation or feedback.

Since our SN feedback model deposits SN energy in the surrounding cells, it tends to leave the central portion of the star-forming cloud, in the host cell, mostly intact. Additionally, while radiative feedback, especially from massive stars, can be quite

effective in evacuating gas and disrupting star formation in small halos (Wise et al., 2012; Whalen et al., 2004), we have not modeled it in this simulation. Conversely, however, the ionization and shock fronts created by radiative feedback may also trigger star formation in clumps or pillars (Tremblin et al., 2012; Deharveng et al., 2010) of very dense gas that are likely to form near the shock boundary. Given these considerations we feel our approach is a reasonable starting point for modeling star formation in turbulent flows. We leave the analysis of the impact of radiative feedback and different SN energies for future study.

2.2.5 Simulation Setup

We evolved a cubic 3 Mpc h^{-1} comoving box from $z = 499$ to $z = 5$ starting from initial conditions generated by the MPGRAFIC code (Prunet et al., 2008). The initial gas metallicity was $Z = Z_{\rm P} = 0$, the initial H_2 fraction was 10^{-6}, and we define $Z_{\rm crit} = 10^{-5} Z_{\odot}$. The base resolution was 512^3 cells ($l_{min} = 9$) corresponding to a grid resolution of 5.86 comoving kpc $\rm h^{-1}$, and a dark matter particle mass of $5.58 \times 10^4\, h^{-1}\, \Omega_{\rm DM}\, M_{\odot}$. We refined cells as they become $8\times$ overdense, or when the local Jeans length is less than four times the current cell size, ensuring we always resolved the Jeans length with at least 4 simulation cells. We allowed for up 8 additional refinement levels ($l_{max} = 17$), using a courant factor of 0.8, resulting in a best possible spatial resolution of 22 physical pc h^{-1}. However, because these additional levels maintain a maximum physical resolution rather than a comoving resolution, the highest refinement level reached by $z = 5$ was level 14. Our settings resulted in a range of star particle masses between $726\, M_{\odot} \leq M \leq 3628\, M_{\odot}$. The nonlinear length scale at the end of the simulation was 0.15 h^{-1} comoving Mpc, corresponding to a mass of $1.5 \times 10^9 M_{\odot}$. Finally, we tuned the code reionization parameters to ensure that the reionization redshift agrees with recent results (specifically, $z_{reion} \approx 8.8$;

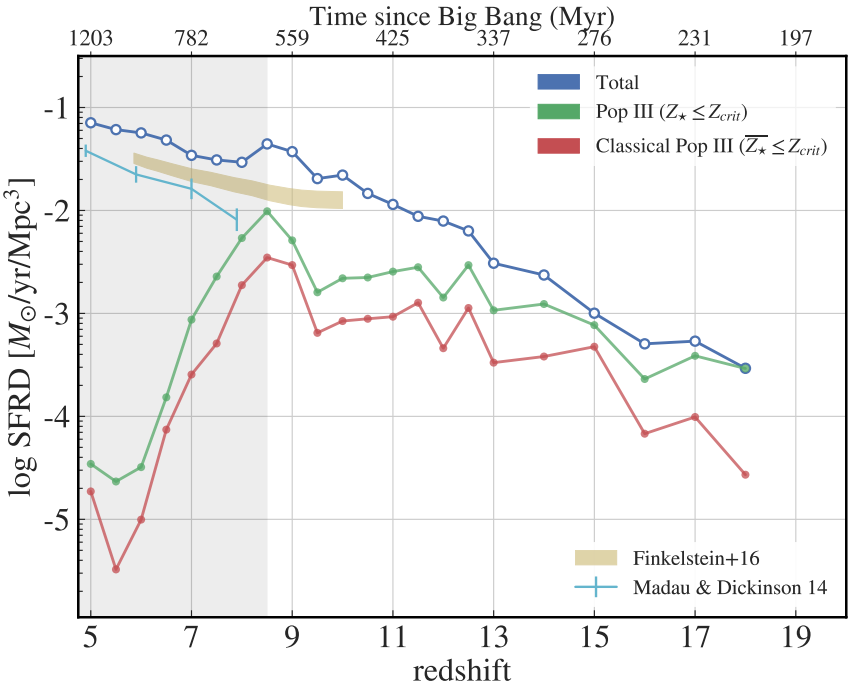

Figure 2.4: Star formation rate (SFR) density for our simulation. For this plot, the "classical Pop III" rate includes only those stars formed in cells in which $\overline{Z} < Z_{\rm crit}$. The Pop III curve also includes metal-free stars found in star particles with $\overline{Z} > Z_{\rm crit}$: the star particle mass fraction $P_\star \times m_\star$. Note that the overall Pop III SFR density is $2-3\times$ higher than the classical rate, indicating that roughly 2/3 of Pop III stars form in partially polluted regions with a mean metallicity $\overline{Z} > Z_{\rm crit}$. We include the observational SFR density by Madau & Dickinson (2014) (compiled from Bouwens et al. (2012a,b)) and the SFRD obtained by integrating the galaxy luminosity function by Finkelstein (2016). The grey region indicates redshifts post-reionization.

Planck Collaboration et al., 2016).

2.3 Results

2.3.1 Evolution of the Overall Star Formation Rate

Our simulation generated a total of 345 halos (at z=5) with a mass range of 79,000 to 372,468,025 $M_\odot$. The largest halo was composed of 513,749 star particles, while the smallest considered had 109. Halos needed to consist of at least 100 star particles before we counted them in this total. Our star formation over-density threshold

(150× overdense), ensured that star formation only occurred in and around collapsed objects. The mean matter density of our simulation in terms of the average matter density of the universe was $\langle \rho_{sim} \rangle / (\rho_{\rm crit} \Omega_{\rm M}) = 1.001$ indicating our volume represents a typical region of the universe.

Figure 2.4 shows the evolution of the star formation rate (SFR) density in our simulation, along with observational results compiled by Madau & Dickinson (2014) from Bouwens et al. (2012a,b). The onset of star formation occurs at $z \approx 18$, which quickly dissociates the small initial level of H_2 in the box, raising the minimum virial temperature of halos in which stars can form efficiently to $\approx 10^4$K. This is above the nonlinear scale for redshifts above $z \approx 6$, and so the SFR density increases roughly exponentially with decreasing redshift throughout the simulation, with some flattening below the redshift of reionization (Scannapieco, 2005). This overall rate is also in good agreement with $z \leq 7$ observations, and while our results are somewhat higher than observations at $z = 8$, this is to be expected as galaxy surveys are magnitude limited, while our simulations also include star formation down to very small mass limits.

For comparison, our high-redshift SFR density is much lower than the one obtained from the Renaissance zoom Simulation of a 'normal' region of the universe (Xu et al., 2016). However, their simulation retains a maximum resolution of 19 comoving pc and ours maintains a maximum resolution of 23 physical pc. At their final simulation redshift of $z \approx 12.5$, this corresponds to a physical resolution of ≈ 1.5 pc vs our ≈ 23 pc, allowing them to trace star formation in much smaller objects than we track and discuss here.

While the very first stars in our simulation are purely metal-free (Pop III), they quickly generate SNe, and the resulting pollution of the pristine gas gives rise to subsequent stellar populations with varying levels of metals. As our subgrid models

allows us to track the pristine gas fraction for every particle, we can calculate not only the "classically determined" Pop III star formation rate in $\overline{Z} < Z_{\rm crit}$ regions but also the formation of stars in unmixed regions with $\overline{Z} > Z_{\rm crit}$ as $P_\star \times m_\star$. In the classically determined case, our results are in good agreement with the simulations of Pallottini et al. (2014) (see also Tornatore et al., 2007) over the range $5 \leq z \leq 8$, while at higher redshifts our rate is somewhat higher, most likely due to our higher base resolution (5.86 versus 19.53 comoving kpc h^{-1}). This extended evolution is indicative of a large-scale spatially-inhomogeneous Pop III/Pop II transition as progressively lower-sigma peaks collapse and form stars in regions far away from sites of previous metal enrichment (Scannapieco et al., 2003).

On the other hand, including metal-free star formation in unmixed regions with $\overline{Z} > Z_{\rm crit}$ leads to an increase in the Pop III rate by a factor of 2-3 over the full range from $5 \leq z \leq 16$. This indicates that small-scale mixing is at least as important as large-scale inhomogeneities in determining the history of metal-free star formation. Or, in other words, at least as many Pop III stars are formed within metal-enriched protogalaxies as are formed in purely metal-free objects.

As noted earlier, our SFR density is dependent on the stellar and SN feedback prescriptions we have adopted, which are the standard ones in RAMSES. In particular, we have not modeled radiative feedback from these first, massive stars. As discussed in Whalen et al. (2004), such feedback is likely quite effective in dispersing the original star-forming cloud. We leave the modeling of radiative feedback – as well as progenitor-dependent SN energy – to a follow-up work.

2.3.2 The Gas

To better understand this small-scale pollution of metals, we examine two representative star-forming regions in detail. In Figure 2.5, we show the characteristics

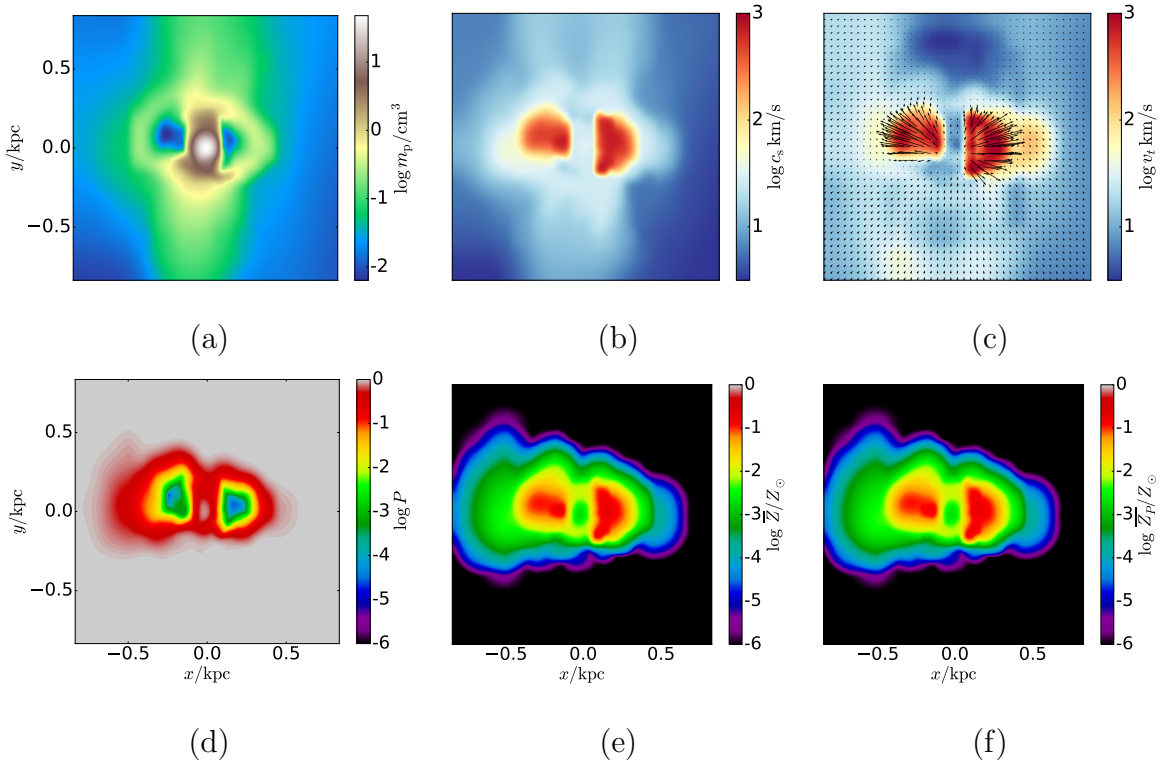

Figure 2.5: Plots of the gas in a representative star-forming region at $z = 16.0$. Panel (a) depicts gas density, (b) sound speed, (c) turbulent velocity (colors) and velocity in the $x - y$ plane (vector lengths on a linear scale up to $\approx 300 km/s$), (d) pristine gas fraction, (e) average metallicity and (f) average primordial metallicity. Note that the $\overline{Z}$ and $\overline{Z}_{\rm P}$ plots are essentially identical indicating that most metals are from Pop III stars. Also, while the average metallicity of much of the gas is non-zero, a high percentage has $P \gtrsim 10^{-1}$, even near the center of the halo. All plots indicate physical scale and correspond to $20\,{\rm kpc}\,h^{-1}$, comoving. All plots are thin slices in the z-plane of the simulation box.

of the gas at $z = 16$, in one of the earliest star-forming regions in our simulation. In the center of panel (a) in this figure, we see the overdense region of gas in which star formation and a burst of SNe have recently occurred. In fact, this is the first occurrence of SNe in this halo. We again point out that each SN in our simulation represents the combined action of $\approx 4 - 20$ SNe, due to our star particle mass range. Panels (b) and (c) depict the impact of the SN burst in terms of the sound speed of the gas (which is $0.15\,km/s\,(T/K)^{1/2}$) and the turbulent velocity. Here we see how SNe heat the surrounding gas to sound speeds of $\gtrsim$ 200 km/s, corresponding

to $10^6 - 10^7$K. These temperatures, while high, are much lower than the initial temperatures at the time at which the SNe occurred in the simulation, because the gas is strongly cooled by adiabatic expansion as the high-pressure regions expand into the intergalactic medium. Thus the radial velocities in figure (c) (vector overlay) are over 300 km/s, resulting in shear strong enough to generate turbulent velocities up to ≈ 500 km/s. This typically leads to supersonic subgrid turbulent mixing as discussed in Section 2.2.2. The value of the pristine fraction shortly after a burst of SN occurs is set by the mass-density of ejecta relative to the newly polluted cells' mass densities – as described in Section 2.2.1. Further, while we have demonstrated that the ISM is likely highly turbulent for reasons previously described, we note that in the case of a compressive shock, the subgrid mixing time is proportional to the sound crossing time in the cell: $\Delta x/c_s$. This is just another way of saying that the mixing time is proportional to the time it takes the shocked gas, along with the pollutants, to cross the cell. As can be seen in Figure 2.5, in a mostly radially expanding shock, *apparently* dominated by compressive modes, our formulation appropriately models the mixing time, $\tau \propto v_t^{-1}$ since in the radial case $v_t \propto v_r$ where v_r is the radial velocity of the shocked gas. This situation only arises in areas of pristine, low density gas that has not been previously stirred by SN or other dynamical effects (e.g. - gravitational shear). However, we say *apparently* here since even a single SN shock expanding into a uniform medium is likely far from purely compressive owing to instabilities in the blast that start within the SN. Such instabilities generate vorticity resulting in clumpy, turbulent ejecta (Padoan et al., 2007).

In the lower panels of this figure, we see two regions of gas with $\overline{Z} \approx 10^{-1}\, Z_\odot$ (red areas in panel (e)). These areas also have the highest polluted fractions ($P \lesssim 1\%$, or $f_{\rm pol} \gtrsim 0.99$) as depicted in panel (d). These areas are found close to the sites of the SNe, in low density gas, and thus they have been turbulently stirred for the

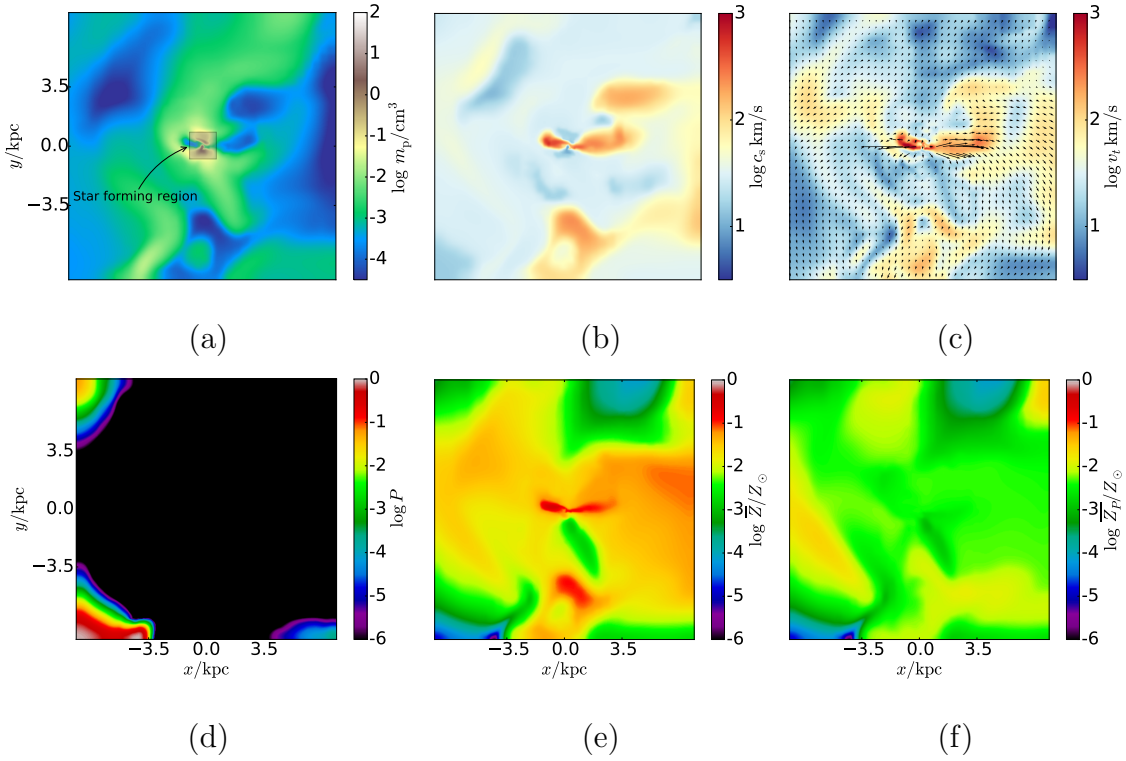

Figure 2.6: Plots for $z = 8.0$ as in Fig. 2.5, whereas the vectors in panel (c) correspond to a linear scale up to 500 km/s. Comparing the $\overline{Z}_{\rm P}$ and $\overline{Z}$ plots, $\overline{Z}_{\rm P}$ is ≈ 1 dex down over most regions indicating pollution by a second-generation of stars. All plots indicate physical scale at the redshift indicated and correspond to 100 kpc h^{-1}, comoving. The region of star formation called out in the density plot is used in Fig. 2.9.

longest times. In addition, the turbulent velocity and sound speed are comparable in these regions– implying subsonic turbulent mixing, which operates more efficiently than supersonic mixing as discussed above. We also see a very small region of highly pristine gas in the area of high-density gas near the center of the halo. This pocket of gas, with $\overline{Z} \approx 10^{-3}$, if it were to collapse, is capable of producing star particles with a very high pristine fraction.

Moving farther out from the center, we see that the average metallicity of the gas falls off relatively slowly, indicating that polluted material has been carried most of the way across this region. However, the radial increase in the pristine fraction is

much steeper, moving to $\gtrsim 10\%$ in $\overline{Z} \lesssim 10^{-2.5} Z_\odot$ areas and increasing to $\approx 100\%$ in areas where $\overline{Z} \lesssim 10^{-4} Z_\odot$. This unmixed gas occurs in the regions in which the turbulent velocity drops sharply, illustrating the correlation between turbulent mixing, the kinetic energy, and the sound speed in the gas. Finally, we note that the vast majority of metals are from primordial stars, indicated by the near identical plots for $\overline{Z}_{\rm P}$ and $\overline{Z}$.

Figure 2.6 depicts the gas in a $100\,{\rm kpc}\,h^{-1}$ comoving star-forming region at $z = 8$. Unlike in the early halo case shown in Figure 2.5, most of the gas in this case is thoroughly mixed. The metallicity plot shows that the gas has been enriched to at least $\overline{Z} \geq 10^{-3}\, Z_\odot$ throughout most of this slice. Looking at the sound speed and turbulent velocity plots we note that, in general, there are few regions where $v_{\rm t} \gg c_{\rm s}$, indicating that SN energy has mostly been disbursed: another indication that there has been sufficient time for mixing to occur. On the other hand, there remain pockets of gas around the edge of this slice in which the overall metallicity is relatively high, $\overline{Z} \gtrsim 10^{-3} Z_\odot$, but where $P \gtrsim 10^{-2}$. These regions of incomplete mixing correlated with regions of lower density. By comparing $\overline{Z}$ to $\overline{Z}_P$, we note that, roughly, only 10% of the metals in this region are primordial indicating thorough pollution by a second-generation of SN. Interestingly however, there is one region just below the central star-forming region with $\overline{Z} \approx 10^{-3} Z_\odot$ with densities of $10^{-1}\, m_{\rm p}\,{\rm cm}^{-3} < \rho \leq 10^{-2.5}\, m_{\rm p}\,{\rm cm}^{-3}$ where we find $\overline{Z} \approx \overline{Z}_P$, indicating that most of the metals here are likely from first generation ejecta. Should subsequent star formation occur in this moderately dense region we would expect a population of stars with a high fraction of primordial metals. Even in this seemingly well polluted region our two new scalars have allowed us to paint a more nuanced picture of metal-enrichment of the gas, that will lead to important observable differences for the resulting stellar populations.

2.3.3 *Stellar Populations*

Figure 2.7 shows several properties of stars formed in a representative minihalo at $z = 16$. Note that the metallicities in this figure are corrected to correspond to the metallicities of the subset of enriched stars within the star particle, $Z_\star = \overline{Z}_\star f_{\rm pol}^{-1}$, as described in §2. Here we have used the upper bound for the correction to the metallicity since we are at high redshift and the gas in and around the halos is in the process of being enriched by a group of SN. As the star particles in the uppermost left panel of subplot (a) in this figure have $Z_\star \leq Z_{\rm crit}$, even after correcting for $f_{\rm pol}$, they represent stellar mass composed of pristine material, labeled as 'classical' Pop III stars in Figure 2.4. Such particles make up about 17% of the stellar mass of this early halo, as compared to the majority of the star particles which fall into the metallicity bin $10^{-3} Z_\odot < Z_\star \leq 10^{-1} Z_\odot$. Interestingly, correcting for the polluted fraction of gas results in no stars in the metallicity bin $10^{-5} Z_\odot < Z_\star \leq 10^{-3} Z_\odot$. This indicates that the polluted fraction of the cell must have been relatively small when ejecta in this range polluted star-forming cells, resulting in enhanced metallicities ($Z_\star > 10^{-3}\, Z_\odot$) due to the concentration of the metals. This can be easily seen in the top panels of Figure 2.8. Examining the pristine and polluted fraction plots, its apparent that many of the higher $Z_\star$ star particles reach these high corrected metallicities only because they not only have pristine fractions, $P_\star$ greater than 10%, but polluted fractions $f_{\rm pol} = 1 - P_\star$ less than 10%, implying $P_\star > 0.9$; meaning that the majority of the gas from which they were formed was unmixed. In fact if we include the pristine fractions of all star particles, the Pop III fraction for this halo grows to 57%, an increase of a factor of nearly 3.4. However, we note several star particles in panel (a), $10^{-3} Z_\odot < Z_\star \leq 10^{-1} Z_\odot$, to the lower-right of the central concentration of particles, that do not appear in the pristine fraction plot for $P_\star > 10^{-1}$. These star

particles formed at a later time in gas that was more thoroughly mixed and represent a relatively small population of almost all Pop II stars with $10^{-5} < P_\star \leq 10^{-3}$. Additionally, by comparing the spatial distribution of stars as a function of metallicity, $Z_\star$, to the distribution of stars as a function of primordial metallicity, $Z_{\mathrm{P},\star}$, we can see that almost all of the metals in the enriched stars within this halo are produced by Pop III stars.

These conclusions are supported by Figure 2.8, which shows the total, Pop III, and primordial stellar masses ($f_{\mathrm{pol}} \times M_\star \times \frac{Z_{P\star}}{Z_\star}$) binned according to the star particles' corrected metallicity (right side). For comparison, we also include an uncorrected metallicity histogram to show the effects of the f_{pol} correction to $\overline{Z}_\star$. While there are a fair number of star particles with average metallicities in the range $10^{-5} Z_\odot < \overline{Z}_\star \lesssim 10^{-2.6} Z_\odot$, the lowest nonzero corrected metallicities are $\approx 10^{-3.1} Z_\odot$. In fact, after correcting for the polluted fraction, these extremely low average metallicity star particles are amongst the star particles with the highest corrected metallicities, such that star particles with $Z_\star \gtrsim 10^{-1.6} Z_\odot$ are over 99.6% pristine. These are the star particles that form at the edges of the extent of enriched material, still within the central star-forming region, in which the average gas metallicity is low but very little mixing has occurred, such that the metals are concentrated into just a few stars.

As mentioned above, we have not modeled radiative feedback in our simulation and our example halo at z=16 formed classical Pop III stars in two successive yet closely spaced ($\Delta t < 7$ Myr) waves. Even though radiative feedback from these stars would likely lower densities and suppress further central star formation (Wise et al., 2012), it is also possible for feedback to trigger nearby collapse in dense clumps in the pristine gas. Our simulation indicates subsequent significant star formation in this halo takes place on a time scale of < 20 Myr, such that star particles still have relatively high pristine fraction, $P > 0.1$. While we feel these results are representative

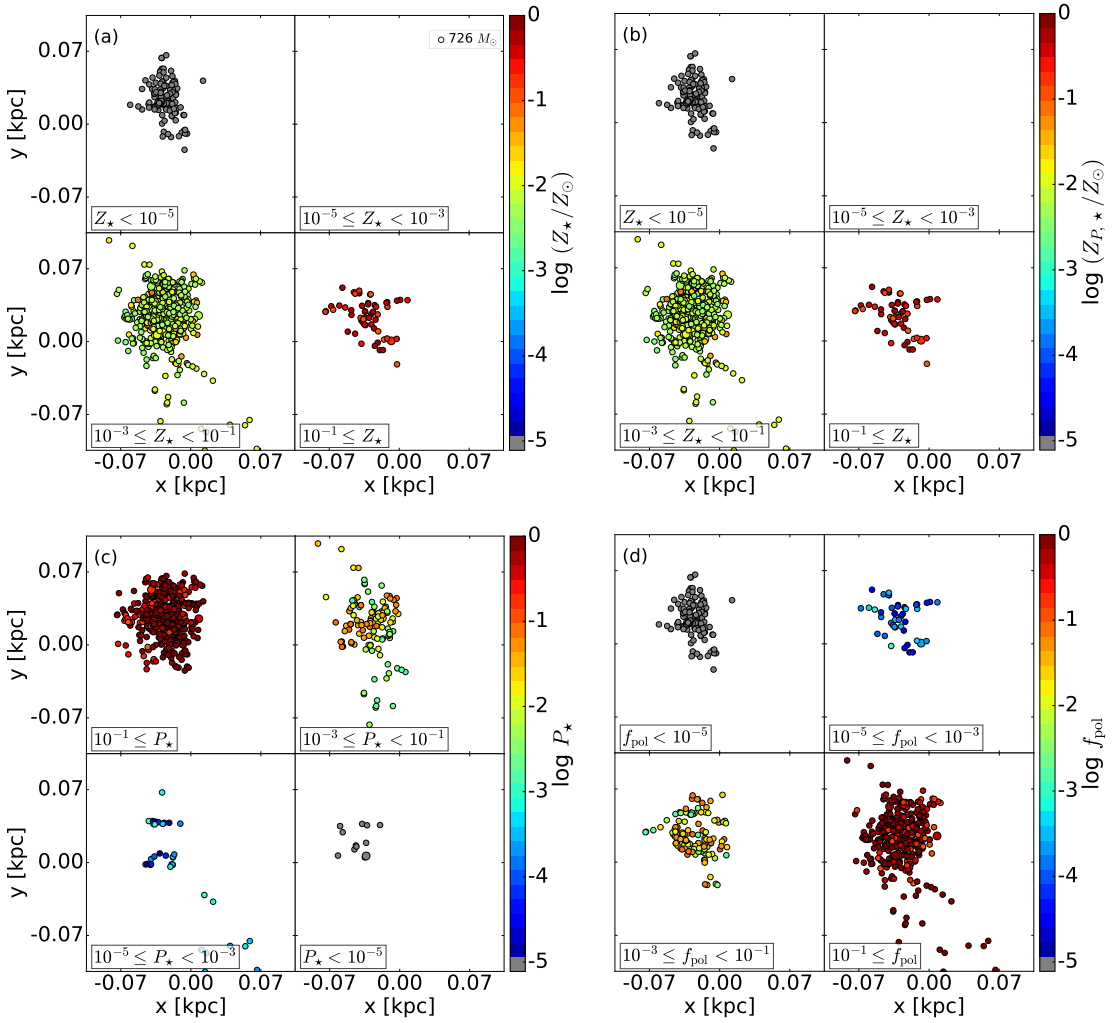

Figure 2.7: Properties of the stars formed in a halo at $z = 16$. Each group of 4 plots depicts star particle locations in physical kpc, 2.5 kpc h^{-1} comoving. Dot size indicates star particle mass in $M_\odot$. Panels (a) & (b) depict corrected metallicity & primordial metallicity binned in 4 metallicity subranges. These are nearly identical, indicating that almost all (99%) of the metals in this halo are primordial (from Pop III SN). Panels (c) & (d) depict star particle pristine fraction and the polluted fraction binned in 4 subranges. While many of these star particles have metallicities in the range $10^{-3}Z_\odot \leq Z_\star < 10^{-1}Z_\odot$, a significant fraction of the stars they represent are Population III (panel (c), $10^{-1} \leq P_\star$).

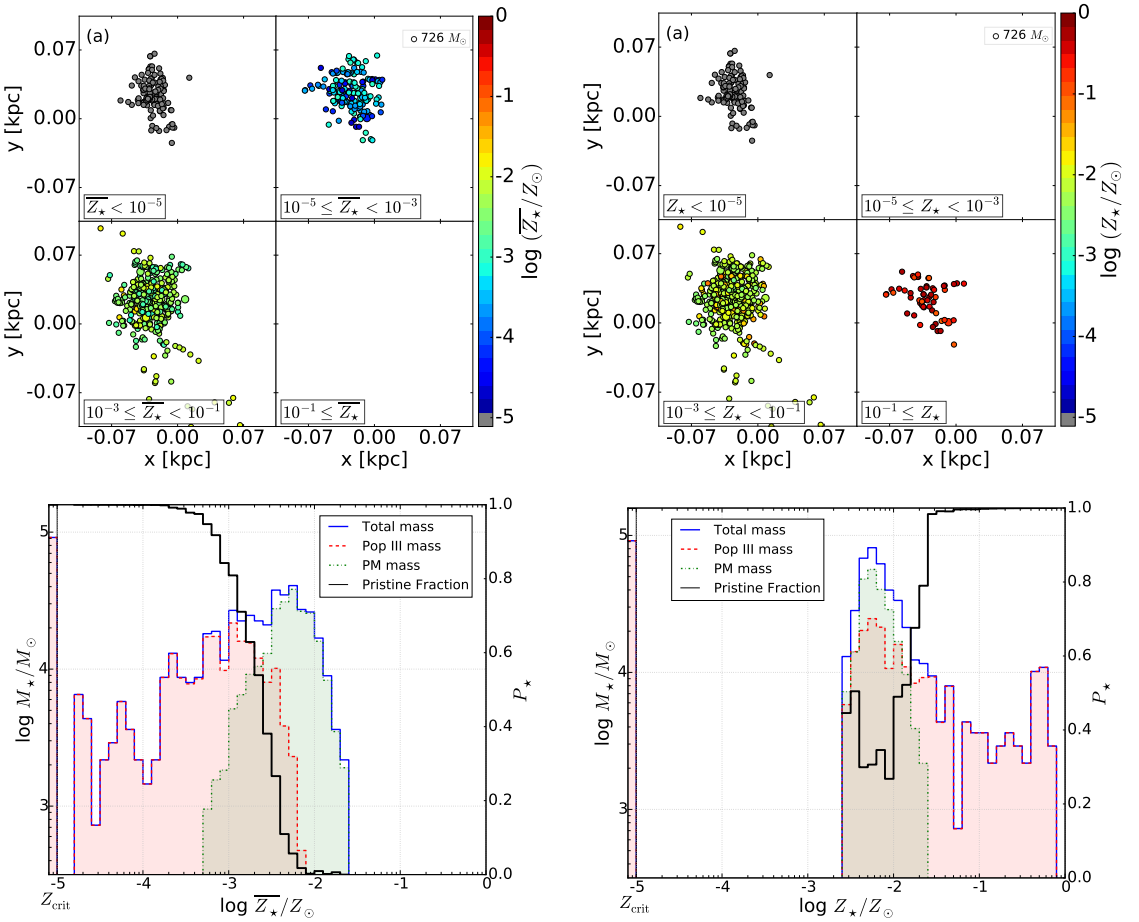

Figure 2.8: Histograms depicting star particle pristine and primordial mass binned in the particles' associated average (left) or corrected (right) metallicity for a star-forming region at $z = 16$ using 50 logarithmic metallicity bins from $10^{-5}\,Z_\odot$ to solar. We have binned all classical Pop III stars ($Z_\star$ or $\overline{Z}_\star < Z_{\rm crit}$) just below the bin at $Z_{\rm crit} = 10^{-5} Z_\odot$. The histograms' right axes depict the particles' pristine fraction in each metallicity bin. The Pop III mass in each metallicity bin corresponds to $P_\star \times M_\star$ (red) and the primordial metal (PM) mass is $f_{\rm pol} \times M_\star \times Z_{P\star}/Z_\star$ (green). Comparing the two panels, we see that the relatively small $f_{\rm pol}$ of gas in this halo significantly enhances the metallicity of the star particles with $\overline{Z}_\star \lesssim 10^{-2.5} Z_\odot$. In fact, 99.6% of star particle mass with $Z_\star \gtrsim 10^{-1.6} Z_\odot$ (right panel) represents Pop III stars. Overall, 98.6% of stellar metals are primordial and these polluted stars have metallicities $10^{-2.8} Z_\odot < Z_\star < 10^{-1.6} Z_\odot$.

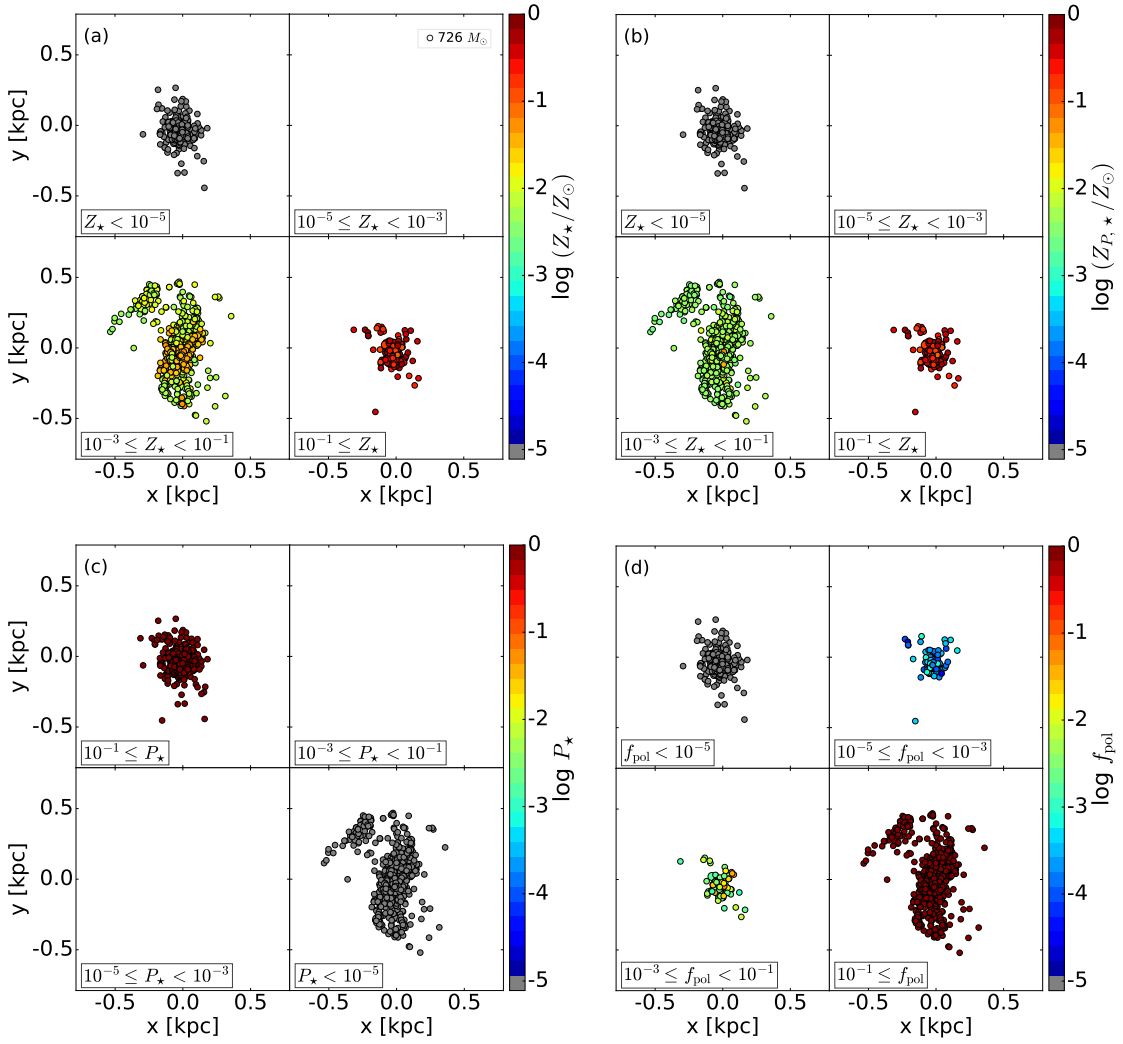

Figure 2.9: Halo at $z = 8$. Panels as in Fig. 2.7. For this halo we note the PM is down ≈ 1 dex from the overall metallicity of the stars in the range $10^{-3}Z_\odot \leq Z_\star < 10^{-1}Z_\odot$ (panels (a) and (b)). However, there is still a relatively large fraction of pristine stars in this halo as discussed in the text. The comoving scale is 9.5 kpc h^{-1} with the axis labeled in physical kpc.

it will be interesting to model radiative feedback and quantify the differences.

Moving to $10^{-2.8} Z_\odot < Z_\star \lesssim 10^{-1.6} Z_\odot$ star particles formed in more vigorously stirred material, we find that 38% of this material is composed of Pop III stars. In fact, only when one also includes star particles with average metallicities up to $10^{-1.6} Z_\odot$ does one arrive at a 57% mass fraction of Pop III stars in this object. Finally, from the primordial stellar mass histograms we can see that the majority of enriched stars are found in $10^{-2.5} Z_\odot < \overline{Z}_\star \lesssim 10^{-1.5} Z_\odot$ particles, and that in these particles, essentially all the metals are generated by Pop III stars.

In Figure 2.9, we turn our attention to the properties of the stars formed in a halo at $z = 8$. Unlike Figure 2.7, which shows a different $z = 16$ region than shown in the gas plots in Fig. 2.5, Fig. 2.9 shows the stellar distribution in the same region at the center of the $z = 8$ region depicted in Figure 2.6. This halo is older than the $z = 16$ halo and has formed stars over a longer period, resulting in more metals and significantly more mixing. However, while the more extended history shifts the average metallicity to somewhat higher values than in the $z = 16$ case, they still share many features. In both halos, the largest collection of star particles occurs in the $10^{-3} Z_\odot < Z_\star \leq 10^{-1} Z_\odot$ range, in both halos there are large number of star particles with $f_{\rm pol} < 0.1$, and in both halos a significant number of Pop III stars are formed.

On the other hand, unlike the higher redshift case, second-generation metals are present in the $z = 8$ halo, as can be seen by comparing the total metallicity in subplot (a) to the primordial metallicity in subplot (b). This shows that the primordial metals are down by a factor of ≈ 3 from the $Z_\star$ levels. And while there is a large fraction of star particles with $P_\star > 0.1$, there is also now a comparable fraction with $P_\star \leq 10^{-5}$ indicating a large fraction of star particles fully polluted with metals.

Figure 2.10 depicts the metallicity distribution for the star particles in this mini-

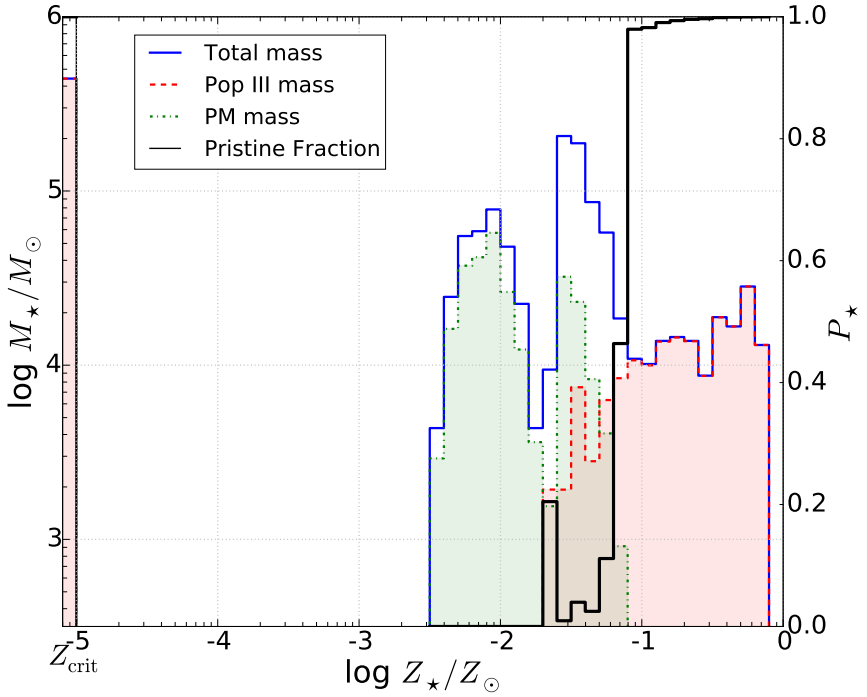

Figure 2.10: Metallicity histogram for the halo at $z = 8$ binned as in Fig. 2.8 with pristine fraction on the right axis. We note three distinct stellar populations: one with $10^{-2.6} < Z_\star \leq 10^{-1.8}$ consisting mostly of older stars with a high fraction (67%) of primordial metals. Another population of stars between $10^{-1.8} < Z_\star \lesssim 10^{-1.1}$ has a much lower fraction of PM, 13%, and composed mostly (95%) of Pop II stars. Finally, 99.5% of the stellar mass with $Z_\star \geq 10^{-1.1}$ represent Pop III stars.

halo. As visible in the scatter plots, a much larger fraction of stars in the range $10^{-1.8} Z_\odot < Z_\star \lesssim 10^{-1.1} Z_\odot$ are polluted (95%) and the fraction of primordial metals, 0.13, is much lower than in the earlier halo. However, looking at stars in the range $10^{-2.7} Z_\odot < Z_\star \leq 10^{-1.8} Z_\odot$ we again see a population of Pop II stars with a high fraction of primordial metals. These most likely represent an older population that was mostly polluted with Pop III material, which are likely good CEMP-no candidates. We also note another large Pop III group of stars born in largely unmixed gas with $Z \geq 10^{-1.1} Z_\odot$. In fact, 99% of the stars in these star particles are pristine. For comparison, Table 2.2 captures some of the relevant characteristics of the two halos we have been discussing. Here, angle brackets around the metallicity indicates

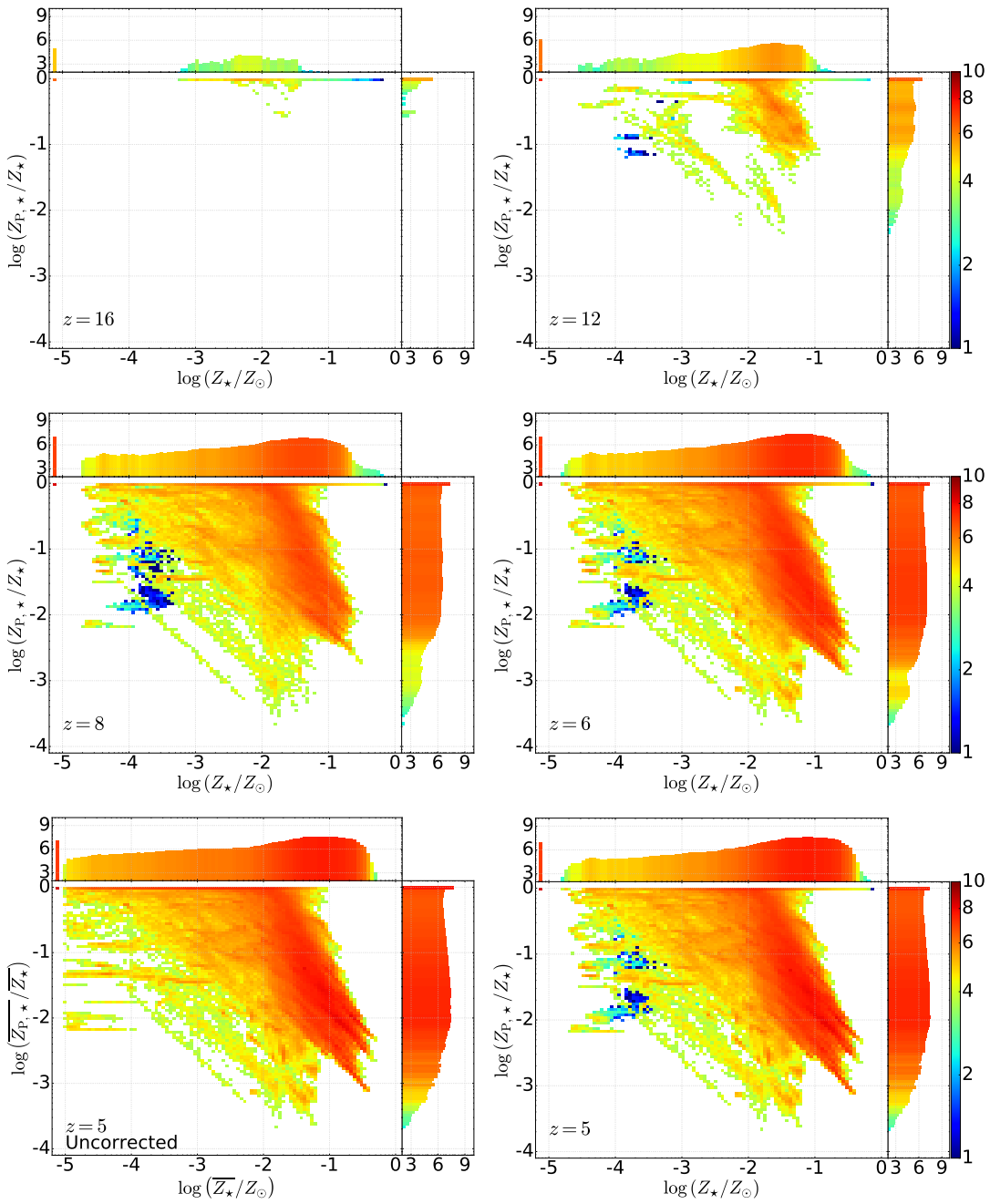

Figure 2.11: Evolution of the joint mass-weighted PDFs for our star particles. Units are $M/M_\odot$ normalized to the (logarithmic) bin size and comoving volume of the simulation, all metal-free star particles are represented at [-5,0]. There is a clear trend toward smaller primordial fractions, $Z_{\rm P,\star}/Z_\star < 1$, in higher metallicity stars, $Z_\star \geq 10^{-3}\,Z_\odot$. However purely primordial star particles $Z_{\rm P,\star} = Z_\star$ are found over a range of metallicities ($10^{-3}Z_\odot \lesssim Z_\star \lesssim 10^{-0.5}Z_\odot$). For comparison, we also include a PDF for the uncorrected metallicities (lower left panel), which is dramatically different at low metallicities.

Table 2.2: Halo characteristics

Redshift	Total $[M/M_\odot]$	Pop III $[M/M_\odot]$	$\frac{\text{Classic Pop III}}{\text{Pop III}}$	$\langle Z_\star \rangle^{\text{a}}$ $[Z_\odot]$	$\langle Z_{\text{P},\star}/Z_\star \rangle^{\text{b}}$
16	5.35×10^5	3.04×10^5	0.300	3.07×10^{-3}	0.988
8	1.45×10^6	6.19×10^5	0.714	1.53×10^{-2}	0.322

[a] Mass-weighted average metallicity for all stars in the halo.
[b] Mass-weighted average primordial metal fraction for polluted stars in the halo

a mass-weighted average taken over all stars in the halo.

Finally, we examine the evolution of the metallicity of our star particles in aggregate. Figure 2.11 depicts the evolution of the mass-weighted probability density function (PDF) for our star particles, with the primordial metal fraction, $Z_{\text{P},\star}/Z_\star$ plotted against the corrected metallicity, $Z_\star$. As expected, as metallicity increases the fraction of primordial metals decreases (at every epoch) giving the plots their characteristic negative slope. By redshift 5, the majority of the stars have metallicities in the range $10^{-1.8} Z_\odot < Z_\star < 10^{-0.5} Z_\odot$. As we move to extremely metal poor populations, $Z_\star < 10^{-3}$, the negative slope of our PDF indicates that the fraction of primordial metals increases as overall metallicity decreases such that the most stars have $Z_{\text{P}}/Z_\star > 10^{-1}$. These Population II stars are likely CEMP-no candidates. Furthermore the distribution of stars with $Z_\star < 10^{-1.5}\, Z_\odot$, remains roughly constant below $z = 6$ indicating that most of the low-metallicity stars, including those with a high fraction of primordial metals, have been formed before this epoch.

As in previous diagrams, we have used the upper bound for the corrected metallicity to make these plots. For comparison, the lower left plot, annotated 'Uncorrected', shows the effects of not making the polluted fraction correction to the metallicity at $z = 5$. The f_{pol} correction is greatest for star particles with $\overline{Z}_\star \lesssim 10^{-3.5}$ since these were contaminated by material with both a low average metallicity and a small f_{pol}.

Without this correction we would predict a larger number of stars with metallicities near $Z_{\rm crit}$, while the corrected results show very few stars enhanced to values below $10^{-4}Z_{\odot}$. The correction also shifts the population of purely primordial star particles, $Z_{\rm P}/Z_{\star} = 1$ at $z = 5$, away from very low metallicities, concentrating them in the range $10^{-3}Z_{\odot} < Z_{\star} < 10^{-1}Z_{\odot}$. While stars in this metallicity range are not extremely metal poor, they do possess a large fraction of primordial metals and may represent an important iron-poor stellar population.

For comparison, we include PDF plots for the lower bound on the correction to $Z_{\star}$. As can be seen in Figure 2.12, if we assume that the maximum amount of metals in these star particles is distributed in the Pop III stars, at a level $Z_{\star} \lesssim Z_{\rm crit}$, we reduce the enhancement of the lowest metallicity stars. This is clearly depicted in lower-left panel where we have differenced the masses in the metallicity bins between the upper and lower bounds for star particles at $z = 5.0$.

2.3.4 Chemical Evolution

The two types of metallicity associated with our star particles, $Z_{\star}$ and $Z_{\rm P,\star}$, provide us with the information needed to more accurately model their chemical make-up, and compare them with observations. Motivated by the lack of $Z \leq 10^{-1.5}Z_{\odot}$ Pop II star formation below $z = 6$, we assume that at $10^{-1.5}\,Z_{\odot}$ the final distribution of enriched stars in our simulation can be compared with the distribution of metal-poor halo stars, and we model the abundances of our stars as the convolution of the ejecta of a single type of Pop III SN (for $Z_{\rm P,\star}$) and a single-set of abundances representative of second-generation metals (for $Z_{\star}$) at $z = 5$. While a more heterogeneous model for Pop III SN ejecta would be more physical (Heger & Woosley, 2002; Ishigaki et al., 2014), it would also introduce additional parameters into the problem, and thus we focus in this first paper on a single representative model for this study. Specifically,

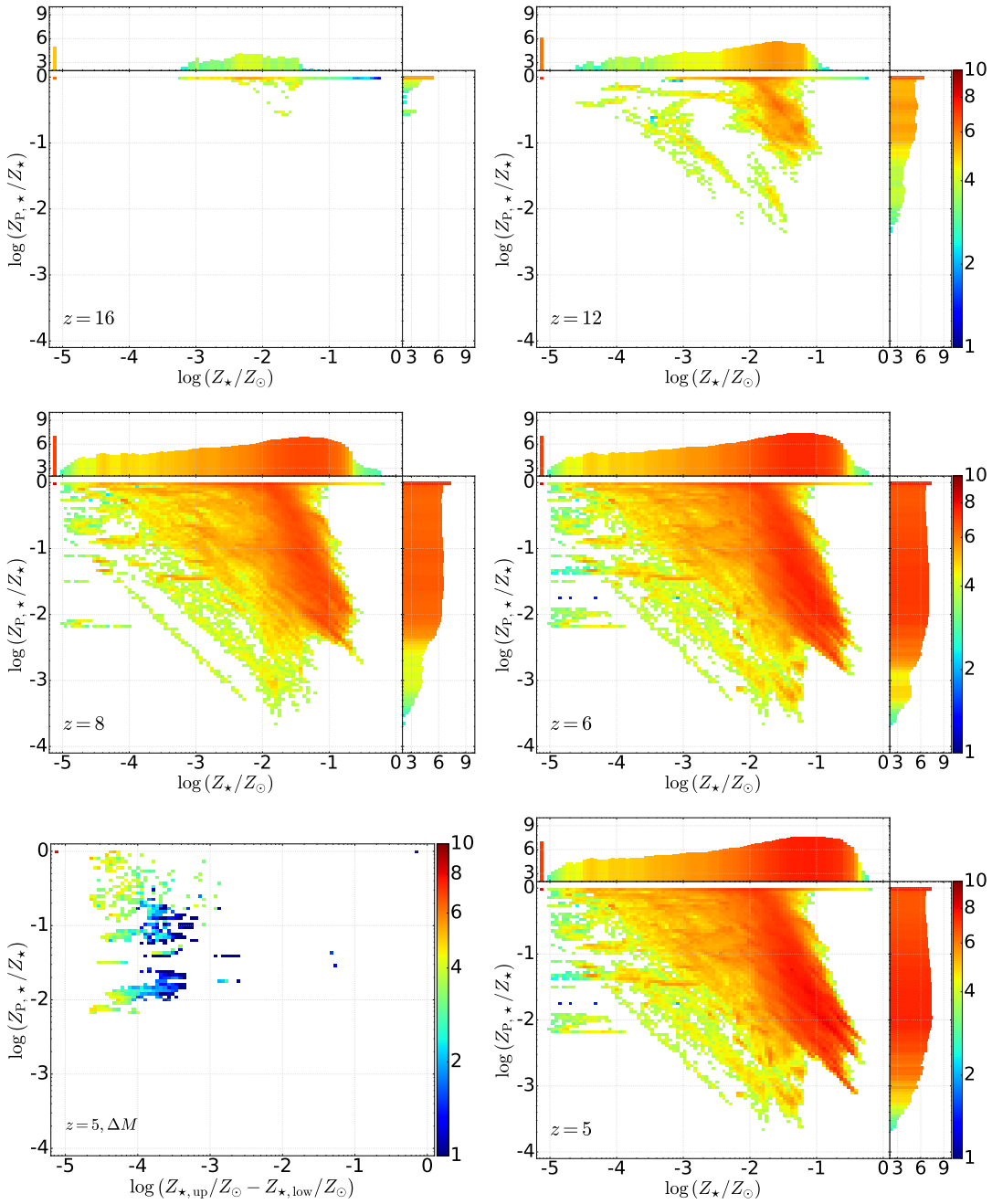

Figure 2.12: Joint mass-weighted PDFs for our star particles using the lower bound on the metallicity correction to correct star particle metallicity. Units are as in the previous figure. Here we note more mass in the very low ($Z_\star \lesssim 10^{-4} Z_\odot$) bins since the lower bound correction assumes that the maximal amount of metals are tied up in Pop III stars ($Z_\star \approx Z_{\mathrm{crit}}$). The lower-left panel depicts the difference between the upper-bound and lower-bound metallicities for all $z = 5$ star particles.

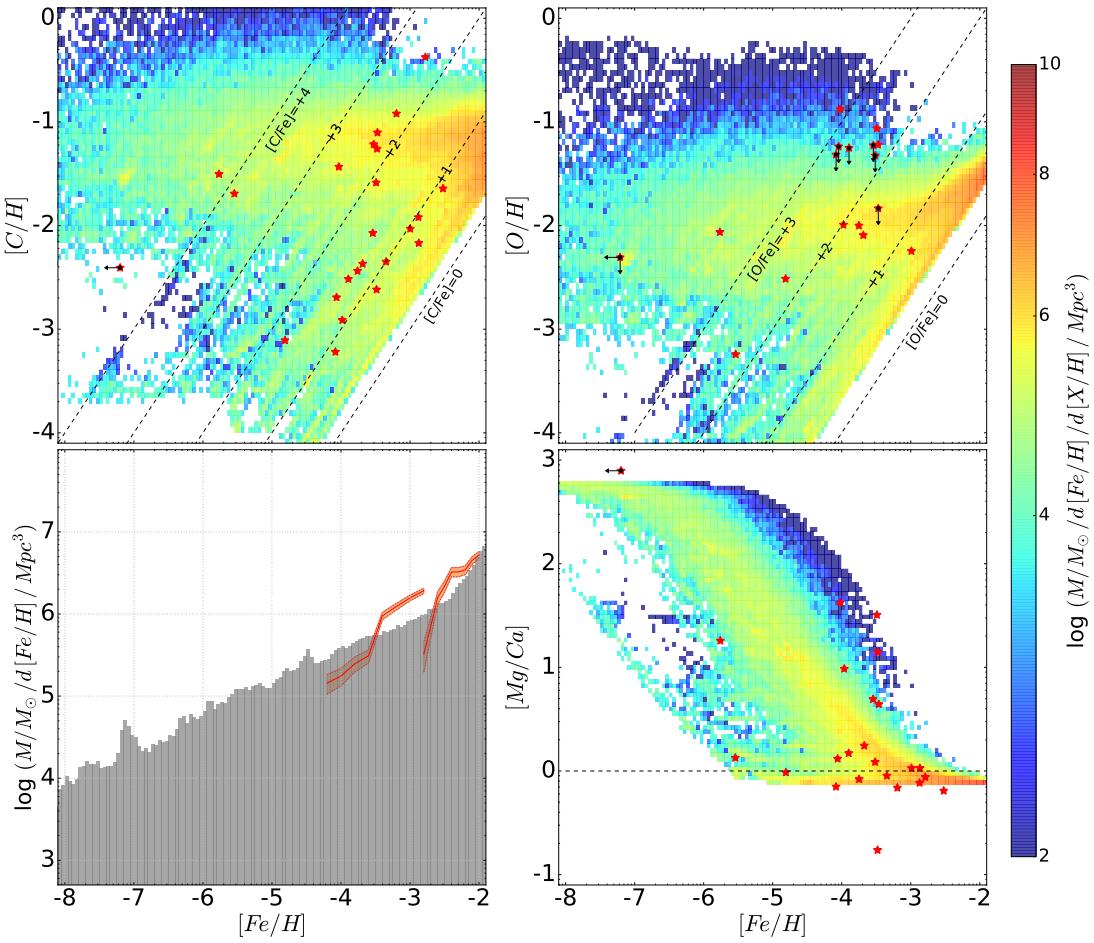

Figure 2.13: Joint PDFs depicting the mass-weighted probabilities for the chemical abundances of [C/H], [O/H] and [Mg/Ca] as a function of [Fe/H] for stars in our simulation. The histogram (bottom left) bins our stars' [Fe/H] abundance and captures our MDF. The histogram is overlaid with observational MDFs for a population of metal poor stars selected from Yoon et al. (2016) (lower MDF) and An et al. (2013) (upper MDF). Our PDFs correlate well with the observations of CEMP-no stars from Keller et al. (2014) (red stars). Note that our MDF histogram includes all stars in our simulation, while the observational data focus on metal poor and CEMP(-no) stars.

Table 2.3: Mass fractions of metals

Element	X/Z 1 Gy	X/Z_P 60 $M_\odot$ Pop III SNe
C	1.68×10^{-1}	7.11×10^{-1}
O	5.29×10^{-1}	2.73×10^{-1}
Mg	2.49×10^{-2}	9.56×10^{-4}
Ca	3.00×10^{-3}	1.43×10^{-7}
Fe	5.39×10^{-2}	2.64×10^{-12}

The mass fractions of metals for selected elements used to model the normal and primordial metallicity of star particles in our simulation. Data for gas typical of $1\,Gyr$ post BB provided by Timmes (2016). Data for $60 M_\odot$ Pop III SN provided by Heger (2016).

we model the metallicity produced by primordial stars as the yield from $60\,M_\odot$ Pop III SN (Heger, 2016). This very iron poor and carbon enhanced ejecta is a best-fit for the CEMP-no star SMSS J031300.36-670839.3 studied by Keller et al. (2014) and is representative of core-collapse SN yields in the $25 M_\odot \leq M_\star \leq 140 M_\odot$ range in which metal yields are believed to be carbon-enhanced and iron poor (Heger & Woosley, 2002). The composition typical of $z = 5$ was determined by a chemical evolution model run to that epoch by Timmes (2016). We capture the characteristics of these two types of material in Table 2.3.

Using the $60 M_\odot$ Pop III SN yields, we model [C/H], [O/H] and [Mg/Ca] to [Fe/H] ratios for stars in our simulation as

$$Z^i_\star = (Z_\star - Z_{\mathrm{P},\star})\; X^i_{\mathrm{T}} + Z_{\mathrm{P},\star}\, X^i_{60\mathrm{SN}} \tag{2.21}$$

Here, $Z^i_\star$ denotes the star particle's final mass fraction (not solar units) of $i \in$ [C, O, Mg, Ca, Fe] and where the subscripts T and 60 SN denote the mass fractions of these elements in Timmes (2016) model and Heger (2016), respectively. The results are displayed in Figure 2.13 in which we present mass-weighted, joint PDFs for all of

the stars in our simulation. The probabilities have been determined using each star particle's corrected metallicity and primordial metallicity as described above. Once again we have used the upper bound for the correction to star particle metallicity. Using the lower bound does not change the probability distribution and hence does not make a difference in this analysis. The PDFs have also been normalized by the logarithmic bin size and the comoving simulation volume. As the Timmes (2016) iron yields are [Fe/H] ≈ -0.5, and very few $Z < 10^{-1.5} Z_{\odot}$ Pop II stars are formed below $z = 6$, as shown in Figure 2.11, we focus on the [Fe/H] range below -2, for which the $z = 5$ results can be related to stars observed today. In this range, for comparison, we have over-plotted the CEMP stars from Keller et al. (2014), with uncertainties, where known.

Without any fine tuning, our model results in reasonable agreement between the simulation's results and the observed characteristics of metal-poor stars, albeit using a single progenitor yield model. Note that this is not guaranteed by our choice of Pop III yields, which were selected by Keller et al. (2014) to reproduce the properties of a single extremely metal-poor star, but are now being convolved with a wide range of $Z_{\star}$ and $Z_{\mathrm{P},\star}$ values. Nevertheless, our model captures many of the features observed in the data. While [Fe/H] can reach extremely low values due the lack of iron in our PopIII yields, [C/H] and [O/H] are always greater than -4 and almost always greater than -3. Note that the lack of such extremely carbon and oxygen poor stars would not be reproduced in models that did not apply corrections to boost the observed metallicities of low $\overline{Z}_{\star}$ star particles with small polluted fractions. Furthermore, our simulations reproduce many other features suggested by the data including the enhanced probability of finding CEMP stars with [C/H] ≈ -1.5 or with [C/Fe] ≈ 0.5, the enhanced probability of finding low-[Fe/H] stars with [O/H] ≈ -2, and the preponderance of low-[Fe/H] stars with [Mg/Ca] ≈ 0.

The histogram at the lower left of this figure depicts the mass-weighted metallicity density function (MDF) for our model overlaid with MDFs derived from MW halo populations (Yoon et al., 2016; An et al., 2013). To account for the fact that these have been derived from surveys targeted to find stars in a specific metallicity range, each of the observational MDFs has been normalized to the simulation's average MDF value over their respective intervals. Additionally, we have included 1 sigma Poisson noise based on the original data for each set of observations.

Given the very low number of stars observed below [Fe/H] = -4.5 and since these MDFs were derived from local observational data over specific, and limited, metallicity ranges we do not expect a tight correlation with our global MDF at $z = 5$. Specifically, the MDF for $-4.3 \leq$ [Fe/H] ≤ -2.8 exhibits selection effects based on the authors' focus on CEMP-no (Yoon et al., 2016) stars, not all metal poor stars and consists of high-resolution observations selected from medium resolution spectra likely to be extremely metal poor. On the other hand, the (An et al., 2013) higher metallicity MDF, [Fe/H] > -3.8, is focused on medium-resolution spectroscopy that makes it hard to identify stars at the low end of the metallicity range, so we have chosen to use [Fe/H] ≥ -2.8 for this data.

2.4 Conclusions

Despite many recent advances in observations of MW halo stars with low metallicities, not a single star has yet been observed that does not contain some metals, pointing to the strong likelihood of a top-heavy Pop III IMF. Without direct observations to constrain the nature of such stars, it falls to theory to help us understand their properties and formation history. Yet modeling this evolution involves not only carrying out large-scale cosmological simulations but also simultaneously tracking the enrichment of material on the much smaller scales in which stars form.

Put simply, the overriding factor that determines the transition from Pop III to Pop II star formation is the metallicity of the gas. While the critical metallicity for this transition is poorly constrained (Schneider et al., 2003; Bromm & Loeb, 2003; Omukai et al., 2005) it is expected to be $Z_{\rm crit} \approx 10^{-5}\, Z_{\odot}$, a level that is not reached until the ejecta from a single SNe are diluted into ≈ 10 million solar masses of material. This means that a key process affecting the formation of Pop II stars is the turbulent mixing of metals into pristine gas. On the other hand, when modeling a statistically significant number of early galaxies, it is too computationally expensive to model the composition of the gas down to star-forming scales. Thus, most works simply assume that metals injected into simulation cells instantaneously change the metallicity of the effected resolution elements, with subsequent star formation making use of these values. Others have used a high-resolution approach to study turbulent mixing within a single galaxy (Greif et al., 2010).

In this work we have developed a new approach that allows us to track, statistically, the effects of subgrid turbulent mixing via a new scalar: the fraction of pristine gas, P, in each cell. We have used a self-convolution model to estimate the rate at which turbulence mixes pollutants thoroughly throughout a given volume of gas (PS 13), which is based only on two physical parameters: the average metallicity, $\overline{Z}$, of the pollutants/ejecta and the turbulent Mach number. We have discovered that thorough mixing can take several eddy turnover times, demonstrating that modeling turbulent mixing is at least as important as modeling large-scale inhomogeneities when determining the Pop III star formation rate density. In fact, we find an increase of $2-3\times$ the Pop III SFR density as compared to similar cosmological simulations that do not account for subgrid mixing (Pallottini et al., 2014; Tornatore et al., 2007). A natural follow-up to this work will be a parameter study in which we vary our stellar feedback prescriptions to quantify the effect on the SFR density.

As a result of modeling the pristine fraction of gas, we also improve our modeling of the metallicity of the polluted fraction, $f_{\rm pol}$, of gas and stars. Since the polluted gas fraction represents the vast majority of the metals in the cell that will eventually be mixed throughout its volume, we know that the metallicity of the fraction of polluted gas in the cell is $Z = \overline{Z}/f_{\rm pol}$. By examining two representative halos, we find a significant difference between $Z_\star$ and $\overline{Z}_\star$ for stars with $\overline{Z}_\star < 10^{-3} Z_\odot$, many of which have $f_{\rm pol} < 10^{-3}$. Assuming that Pop III/Pop II star formation in such incompletely mixed gas proceeds according to the fraction of polluted to pristine gas, we find that the effects of incomplete mixing are extremely important and help us to depict a more physical picture of metallicity evolution of early stars.

Given that the ejecta from the massive first stars is likely to be very different from that of subsequent stellar generations (Heger & Woosley, 2002), we have also developed a straightforward method to track the metals generated by Pop III stars. Our primordial metallicity scalar, $\overline{Z}_{\rm P}$ allows us to follow this material, and model the final metal content of stars as a convolution of two different types of material resulting in star particles with both $Z_{\rm P,\star}$ and $Z_\star$. This alleviates the need to model more detailed, and costly, chemical synthesis networks, and it allows us to quickly explore some of the parameter space suggested by others (Ishigaki et al., 2014; Umeda & Nomoto, 2003), possibly ruling out certain SN progenitor ranges or yield models. In this work, we have modeled primordial metals as the result of $60 M_\odot$ Pop III SN (Keller et al., 2014; Heger, 2016), demonstrating a possible origin for the metal levels seen in the sample of CEMP stars studied by Keller et al. (2014). In the future, we will explore a wider range of PopIII models, hoping to provide insights for interpreting observations of the chemical composition of low-metallicity stars in the local universe.

Finally, we plan to use our new tools to trace the evolution of and derive observational characteristics for a number of early galaxies. While the hunt for Pop III stellar

populations is ongoing, and some promising candidates have been discovered (Sobral et al., 2015), the upcoming James Webb Space Telescope and ground-based Giant Magellan Telescope, Thirty-meter Telescope, and European Extremely Large Telescope will open a much larger window on these objects. Simulations such as ours can help predict the spatial and temporal distribution of Pop III star formation needed to plan future searches for these objects. We are still in the midst of developing models that capture the complex physics of PopIII star formation, and such tools will be crucial in defining the boundaries that help guide observers to find them.

2.5 Appendix - Convergence Across Resolutions

In this section we compare the SFRDs from two 3 h^{-1} Mpc^3 simulations at different resolutions to demonstrate that the subgrid mixing model described in Sarmento et al. (2017) – and used herein – consistently models the formation of Pop III stars in gas with $Z < Z_{\rm crit}$. The simulation from that work has a average physical spatial resolution of 23 pc h^{-1} resulting in the fiducial SFRD depicted in Figure 2.14. As expected, reducing the average physical resolution to 46 pc h^{-1} results in a delayed and lower SFRD early, since small-scale overdensities are 'smoothed over' at lower resolution. However, both the overall SFRD and the Pop III SFRD recover and reach the fiducial level of star formation by $z = 16$, demonstrating the subgrid model produces results that converge for Pop III star formation when using different resolutions.

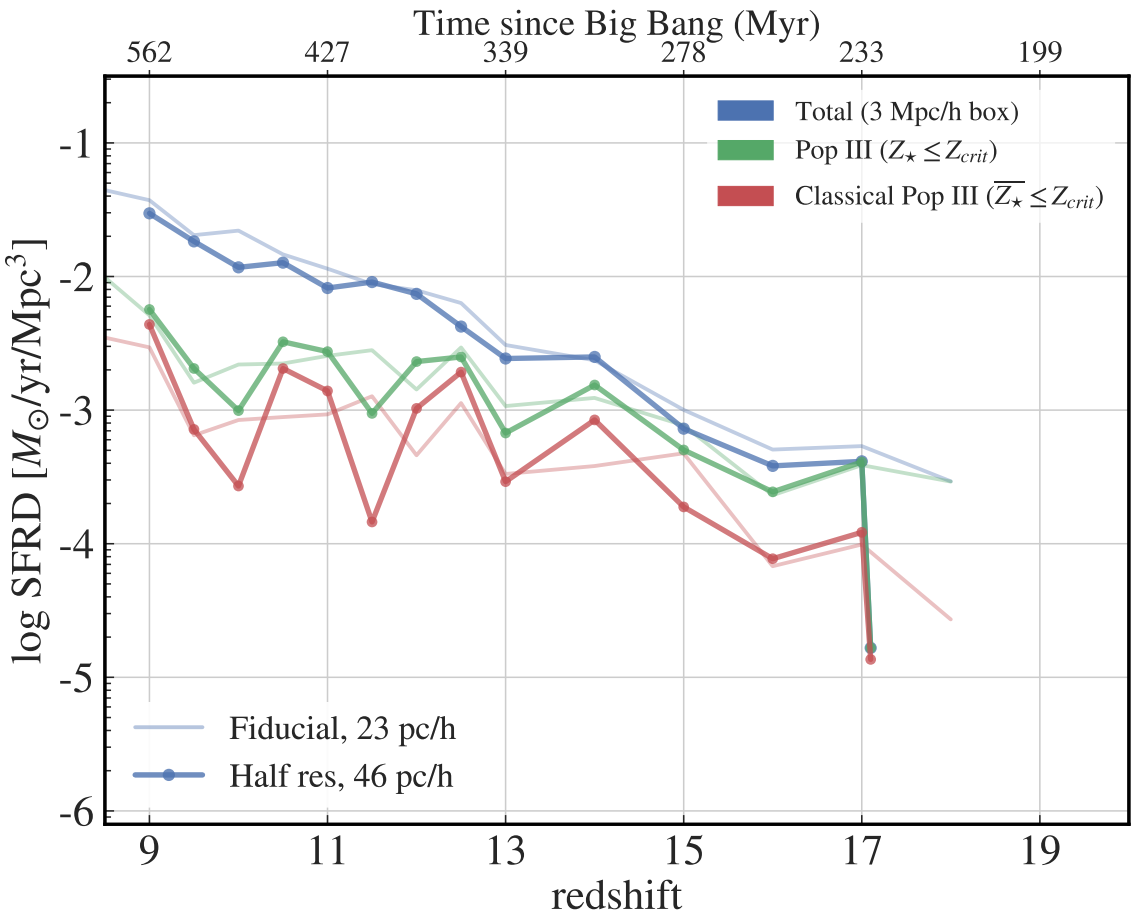

Figure 2.14: The SFRD for the fiducial run in Sarmento et al. (2017) and a run performed at 1/2 resolution. While there are inevitable differences between simulations due to the different resolutions, the subgrid model successfully recovers the Pop III rate shortly after the start of star formation at $z \approx 18$. This demonstrates that modeling the subgrid fraction of pristine gas effectively improves the resolution of Pop III star formation for the simulation.

Chapter 3

THE SEARCH FOR POP III-BRIGHT GALAXIES[1]

3.1 Introduction

Finding and characterizing the first galaxies is the next frontier in observational astronomy. Theoretical studies suggest that these metal-free stars could be observed today if their initial mass function (IMF) extended to low masses (Scannapieco et al., 2006; Tumlinson, 2006; Brook et al., 2007; Salvadori et al., 2010; Hartwig et al., 2015; Ishiyama et al., 2016). However, no one has yet observed a Population III (Pop III) star in or near the Galaxy (Christlieb et al., 2002; Cayrel et al., 2004; Aoki et al., 2006; Frebel et al., 2005; Norris et al., 2007; Caffau et al., 2011; Keller et al., 2014; Howes et al., 2015).

High-redshift observations have yielded candidates for Pop III stellar populations (Malhotra & Rhoads, 2002; Dawson et al., 2004; Jimenez & Haiman, 2006; Dijkstra & Wyithe, 2007; Nagao et al., 2008; Kashikawa et al., 2012; Cassata et al., 2013), without definitive detections. These include a controversial z = 6.6 galaxy analyzed by Sobral et al. (2015) that displays He II λ1640 emission – an indicator of the hard-ultraviolet (UV) spectrum produced by Pop III stars (Tumlinson et al., 2001). Yet, to date, there has not been a confirmed observation of a galaxy dominated by the flux from Pop III stars (Bowler et al., 2017; Pacucci et al., 2017).

This may change in the near future. The soon-to-launch *James Webb Space Telescope* (JWST) is poised to greatly expand our understanding of the high-redshift universe and possibly detect the first galaxies dominated by Pop III flux. Using

[1]This chapter previously published as Sarmento et al. (2018).

JWST, astronomers will be able to assemble galaxy catalogs out to $z = 10$ and beyond and probe the era of the first galaxies (Gardner et al., 2006). However, planning for such observations requires estimating how such galaxies are distributed and, even more importantly, what fraction of galaxies as a function of magnitude and redshift will be dominated by Pop III flux – warranting spectroscopic follow-up.

For now we only have general observational clues about the history of such early galaxy formation. Using extremely deep Hubble Space Telescope (HST) observations, astronomers have been able to amass photometric galaxy catalogs out to $z = 8$ and place initial constraints on galaxy populations out to $z \approx 11$ (Ishigaki et al., 2018; Finkelstein, 2016; Bouwens et al., 2015; Mason et al., 2016; McLeod et al., 2015; Coe et al., 2013; Oesch et al., 2013). While a lot of progress has been made, the latest work at $z > 8$ is hampered by small number statistics and completeness uncertainties (Livermore et al., 2017; Oesch et al., 2015; Atek et al., 2015).

Several groups have used large-scale cosmological simulations and analytic models to investigate galaxy formation, the high-z luminosity function (LF), and galaxy assembly (Somerville et al., 2012; O'Shea et al., 2015; Mason et al., 2016; Barrow et al., 2017). Others have used simulations to explore the transition between Pop III and Population II (Pop II) star formation (Scannapieco et al., 2003; Tornatore et al., 2007; O'Shea & Norman, 2007; Trenti & Shull, 2010; Maio et al., 2010; Zackrisson et al., 2011; Wise et al., 2012; Crosby et al., 2013; Johnson et al., 2013; Pan et al., 2013; Pallottini et al., 2014).

By definition, the first generation of Pop III stars must have formed in the primordial gas. However, an IMF lacking low-mass stars may also result from gas with metallicity below a critical threshold, $Z_{\rm crit}$. The exact value of the threshold depends on whether the dominant cooling channel for the gas is the fine-structure lines of metals or dust emission (Schneider et al., 2003; Bromm & Loeb, 2003; Omukai et

al., 2005). While the value is poorly constrained, it is believed to be in the range $10^{-6} < Z_{\rm crit} < 10^{-3} Z_{\odot}$.

Here we make use of the work described in Sarmento et al. (2017) to track the pollution of the pristine gas at subgrid scales in high-resolution simulations of galaxy formation at high redshift. By following the evolution of the pristine gas, we can estimate the fraction of Pop III stars created in regions that would otherwise be considered polluted above $Z_{\rm crit}$. This allows us to present theoretical predictions for deep photometric galaxy surveys and, in particular, to characterize the fraction of Pop III flux in early galaxies. This information can guide planning for spectrographic follow-up in the search for Pop III stars, searching for their unique observational characteristics (Visbal et al., 2015).

Our approach uses a customized version of RAMSES (Teyssier, 2002), a cosmological adaptive mesh refinement (AMR) code, to follow galaxy formation from the dawn of star formation, at $z \approx 21$, to $z = 7$. Using these simulation results, we generate rest-frame UV ($1500\mathring{A}$) galaxy luminosity functions, to demonstrate that our approach is consistent with existing photometric surveys and generate higher-redshift galaxy luminosity function for a set of JWST Near InfraRed Camera (NIRCam) filters to aid in planning for future such surveys.

Furthermore, using our unique capability to track the rate of subgrid metal pollution, we trace the formation of Pop III stars in these early galaxies and model their impact on the galaxies' flux. In doing so, we are able to identify a fraction of galaxies across a range of redshifts that have a significant fraction of Pop III stellar flux. This allows us to make predictions as to the galaxy luminosities and redshifts that are most likely to show Pop III features, such as narrow He II λ1640 emission, when they are followed up spectroscopically.

The work is structured as follows. In Section 2 we describe our methods, includ-

ing a brief discussion of the implementation of our subgrid model for following the evolution of the pristine gas fraction, our approach to halo finding, and the spectral energy distribution (SED) models used to compute the luminosity of our stars. In Section 3 we show that our high-redshift LF agrees with current observations and make predictions for future JWST surveys. Next, we focus on an analysis of the fraction of Pop III flux emitted by early galaxies that can be used to guide the search for metal-free stars. Conclusions are discussed in Section 4.

3.2 Methods

3.2.1 Simulation Setup & Characteristics

We adopt the following cosmological parameters $\Omega_{\rm M} = 0.267$, $\Omega_\Lambda = 0.733$, $\Omega_{\rm b} = 0.0449$, $h = 0.71$, $\sigma_8 = 0.801$, and $n = 0.96$, based on Komatsu et al. (2011), where $\Omega_{\rm M}$, Ω_Λ, and $\Omega_{\rm b}$ are the total matter, vacuum, and baryonic densities, in units of the critical density; h is the Hubble constant in units of 100 km/s; σ_8 is the variance of linear fluctuations on the 8 h^{-1} Mpc scale; and n is the "tilt" of the primordial power spectrum (Larson et al., 2011).

For this study, we make use of RAMSES (Teyssier, 2002), a cosmological adaptive mesh refinement (AMR) simulation code that uses an unsplit second-order Godunov scheme for evolving the Euler equations. RAMSES tracks cell-centered variables that are interpolated to the cell faces for flux calculations. Flux between cells is computed using a Harten–Lax–van Leer–Contact Riemann solver (van Leer, 1979; Einfeldt, 1988) and the code is capable of advecting any number of these scalar quantities across simulation cells. Self-gravity is solved using the multigrid method (Guillet & Teyssier, 2011) along with the conjugate gradient method for levels ≥ 12 in our simulation. Stars and DM are modeled with collisionless particles and are evolved

using a particle-mesh solver with cloud-in-cell interpolation.

We use RAMSES to evolve a 12 Mpc h^{-1} on-a-side volume from Multi-Scale Initial Conditions (MUSIC, Hahn & Abel, 2013) generated initial conditions through $z = 7$. The initial gas metallicity was $Z = 0$, the initial H_2 fraction was 10^{-6} (Reed et al., 2005), and we define $Z_{\rm crit} = 10^{-5} Z_{\odot}$. The base resolution of 1024^3 cells ($l_{\rm min} = 10$) corresponds to a grid resolution of 11.7 comoving kpc $\rm h^{-1}$, and a dark matter (DM) particle mass of $4.47 \times 10^5\, M_{\odot}\, h^{-1}\, \Omega_{\rm DM}$. We refine cells as they become $8\times$ overdense, resulting in a quasi-Lagrangian approach to refinement. We allowed for up to eight additional refinement levels ($l_{\rm max} = 18$), resulting in an average physical spatial resolution of 45.8 pc $\rm h^{-1}$. Our choice of parameters resulted in a range of star particle masses $8.6 \times 10^3\, M_{\odot} \leq M_{\star} \leq 6.2 \times 10^4\, M_{\odot}$. The highest refinement level reached was 15. The nonlinear length scale at the end of the simulation, $z = 7$, was 47 comoving kpc $\rm h^{-1}$, corresponding to a mass of $3.2 \times 10^7 M_{\odot}$ $\rm h^{-1}$. We did not model sink particles (black holes (BH)) in our simulation since BH feedback is not likely to be significant for our very early galaxies (Somerville et al., 2008; Scannapieco & Oh, 2004). We tune the code reionization parameters to ensure that the reionization redshift occurs at $z_{\rm reion} \approx 8.5$, as reported by the Planck Collaboration et al. (2016). Finally, all magnitudes are in the AB system (Oke & Gunn, 1983).

3.2.2 Simulation Physics

Cooling is modeled using CLOUDY (Ferland et al., 1998) for $T \gtrsim 10^4$ K. Below 10^4 K we adopt the cooling rates from Rosen & Bregman (1995). We allow the gas to cool radiatively to 100 K, but adiabatic cooling can lower the temperature below this threshold. The UV background is derived from Haardt & Madau (1996).

We have also modified RAMSES to include a simple molecular cooling model that is important for low-temperature cooling in the pristine gas (Johnson & Bromm, 2006;

Prieto et al., 2008; Hirano & Yoshida, 2013). Our analytic model is based on Martin et al. (1996) and provides a radiative cooling rate, Λ_r/n_{H2}, per H_2 molecule across the range of densities encountered in the simulation. The details are found in Sarmento et al. (2017).

Star particles (SPs) are spawned in regions of gas according to a Schmidt law (Schmidt 1959) with

$$\frac{d\rho_\star}{dt} = \epsilon_\star \frac{\rho}{t_{\rm ff}} \theta(\rho - \rho_{\rm th}), \tag{3.1}$$

where the Heaviside step function, $\theta(\rho - \rho_{\rm th})$, allows for star formation only when the density exceeds a threshold value $\rho_{\rm th}$. We have set $\rho_{\rm th}$ to be the maximum of $1.0\, m_p\, {\rm cm}^{-3}$ and 200 times the mean density in the simulation. These criteria ensure that SPs are only formed in virialized halos and not in high-density regions of the cosmological flow (Rasera & Teyssier, 2006; Dubois & Teyssier, 2008). We set the star forming efficiency to $\epsilon_\star = 0.01$, a value that results in reasonable agreement with the observed cosmic star formation rate (Finkelstein, 2016; Madau & Dickinson, 2014). The gas freefall time is $t_{\rm ff} = \sqrt{3\pi/(32G\rho)}$.

A fraction of the each SP's mass is returned to the gas in the form of supernovae (SNe). This occurs after the 10 Myr lifetimes for the most massive stars in the IMF (Raskin et al., 2008). The impact of these SNe is parameterized by the fraction of the SP mass that goes SN, $\eta_{\rm SN}$, and the kinetic energy per unit mass of this ejecta, $E_{\rm SN}$. We take $\eta_{\rm SN} = 0.10$ and $E_{\rm SN} = 10^{51}$ ergs/10 $M_\odot$ for all stars formed throughout the simulation, regardless of metallicity. The fraction of new metals in SN ejecta is 0.15 even though metal yields and energy from Pop III stars are likely to have been higher (Scannapieco et al., 2003; Scannapieco, 2005). We may explore different yields and the subsequent effect on stellar enrichment in future work.

While all star particles, within the simulation, are modeled using a Salpeter (1955) IMF with regard to the SN fraction, we model the SEDs of Pop III and Pop II stars

using different IMFs. Each SP models a Salpeter (for the polluted fraction with $Z \geq Z_{\rm crit}$) and a log-normal (for Pop III stars) IMF. Our SP mass resolution is dictated by the star-forming density threshold and our resolution resulting in $m_\star = \rho_{\rm th}\Delta x^3 = 6.6 \times 10^3\, M_\odot$. The final mass of each SP is drawn from a Poisson process such that it is a multiple of $m_\star$.

We do not model radiative transfer or radiation pressure. While radiation pressure from massive young stars can disrupt star formation (Wise et al., 2012; Whalen et al., 2004) it can also trigger it in dense clumps of gas (Tremblin et al., 2012; Deharveng et al., 2010). While we have not modeled its effects for this work, it will be important to characterize the effects of radiative feedback in future work.

3.2.3 The Pristine Fraction and the Corrected Metallicity

In order to more accurately model the fraction of Pop III stars created throughout cosmic time, we track two new metallicity-related quantities. The *pristine gas mass fraction*, P, models the mass fraction of gas with $Z < Z_{\rm crit}$ in each simulation cell. The evolution of this scalar tracks the time history of metal mixing within the cell such that when $P = 0$ the entire cell has been polluted above $Z_{\rm crit}$. The scalar $P_\star$ records, for all time, the value of P in star particles at the time they are spawned and indicates the mass fraction of the SP with $Z_\star < Z_{\rm crit}$.

Figure 3.1 depicts an example of the situation we are addressing by tracking the pristine fraction in simulation cells. Here, a realistic distribution of metals is spread across 4 simulation cells, in 2 dimensions. While the average metallicity in each of these cells is much greater than $Z_{\rm crit}$ there are regions within each cell that are still pristine.

A simple equation can be used to describe the evolution of the pristine gas fraction

in simulation cells:

$$\frac{dP}{dt} = -\frac{n}{\tau_{\rm con}} P(1 - P^{1/n}). \tag{3.2}$$

This equation traces the evolution of P as a function of n and a timescale $\tau_{\rm con}$, which, in turn, are functions of the turbulent Mach number, M, and the average metallicity of the cell relative to the critical metallicity, $\overline{Z}/Z_{\rm crit}$ (Pan & Scannapieco, 2010; Pan et al., 2012, 2013; Sarmento et al., 2017). Modeling the decay of the pristine gas fraction allows us to track the formation of Pop III stars as a mass fraction of all stars created, even in cells with an average metallicity above critical.

Each SP in the simulation is tagged with the average metallicity of the medium from which it was born, $\overline{Z} \rightarrow \overline{Z}_\star$. Furthermore, by knowing the average metallicity, $\overline{Z}$ (or $\overline{Z}_\star$ for SPs), and the pristine gas fraction, P ($P_\star$), we can better model the metallicity of the polluted fraction of gas (or stars). More explicitly, since $\overline{Z}$ represents the average metallicity of a parcel of gas, and the polluted fraction, $f_{\rm pol} \equiv 1 - P$, models the fraction of gas that is currently polluted with metals, we can use the value of $f_{\rm pol}$ to predict the enhanced, or corrected, metallicity,

$$Z = \frac{\overline{Z}}{f_{\rm pol}}, \tag{3.3}$$

of the polluted fraction of gas in each simulation cell. Similarly, $Z_\star$ captures the corrected metallicity of SPs. As expected, when $f_{\rm pol} = 1$ the corrected metallicity is the average metallicity.

The metallicity of the polluted fraction as described by Eqn. (4.3) is only precise when all of the metals are contained in the polluted fraction. This is true only in regions where the pristine gas is first polluted by Pop III SNe. However, it is possible for some of the metals to be distributed in the pristine gas fraction defined as $0 \leq Z < Z_{\rm crit}$. As discussed in Sarmento et al. (2017), this results in a small

uncertainty in the resulting corrected metallicity of our SPs that we will ignore in this work. However, we can easily bound the correction to metallicity. While equation (4.3) captures the upper bound, the lower bound on the correction is

$$Z = \frac{\overline{Z} - Z_{\mathbb{P}} P}{f_{\rm pol}}, \tag{3.4}$$

where $Z_{\mathbb{P}} = Z_{\rm crit} = 10^{-5} Z_{\odot}$ is the upper limit on the metallicity of the pristine gas. If the pristine fraction has $Z_{\mathbb{P}} = 0$, as it would when polluting the primordial gas, we recover equation (4.3). Even when considering this uncertainty, the corrected metallicity, Z, allows us to more accurately model the metallicity of our gas and SPs than would be possible using the average metallicity alone.

Lastly, we note that we do not create polluted stars when $f_{\rm pol} < 10^{-5}$. In this case, we assume that all stars formed in the cell are Pop III since only a tiny fraction of the cell is polluted with metals. While this may seem arbitrary, it is used for convenience as such a small fraction of Pop II stars does not detectably contribute to the luminosity of our galaxies over the entire redshift range analyzed.

3.2.4 Halo Finding

We use the AdaptaHOP halo finder by Aubert et al. (2004) to find star-forming regions in the simulation volume at each redshift of interest. Only halos with at least 100 DM particles, corresponding to a DM halo mass of $1.4 \times 10^7\, M_{\odot}$, are considered by AdaptaHOP. Groups of 20 particles are used to compute the local density of a candidate halo and only objects with a density 80 times the average total matter density are stored.

Several of the more massive objects found by AdaptaHOP consist of more than one observationally distinguishable galaxy. Hence, we post-processed the halos as follows. For each AdaptaHOP halo, we compute a mass, in stars, within a 3 kpc

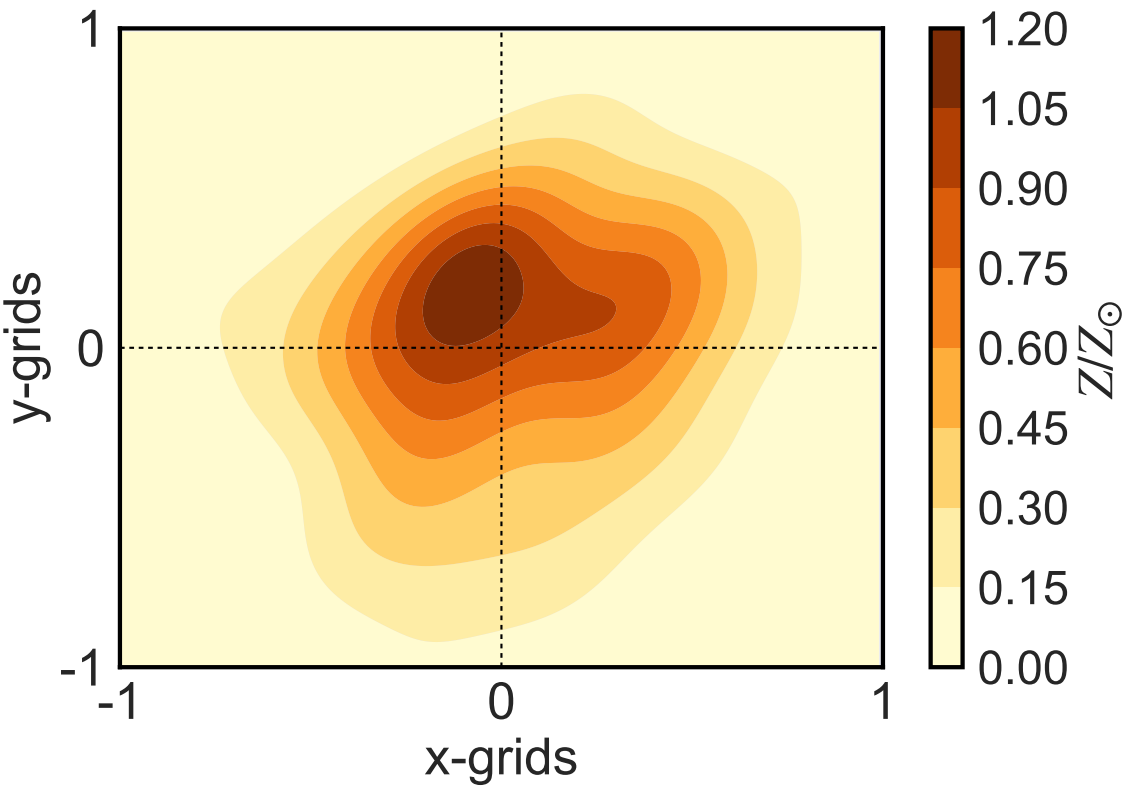

Figure 3.1: An example (2D) distribution of metal concentrations across a set of AMR cells. While the average metallicity, $\overline{Z}$, across these four cells is greater than $Z_{\rm crit}$, there are clearly regions that are still pristine. We track a new scalar, P, in each AMR cell to quantify the fraction of gas with $Z < Z_{\rm crit}$. In conjunction, P and $\overline{Z}$ allow us to better model the actual metallicity of the polluted fraction of gas (as described in the text).

comoving sphere centered on the halo's coordinates. This typically corresponds to the core of the most massive galaxy in the field. Next, we iteratively compute the mass in larger concentric spheres about this core. At each step, we increase the radius by 10^{-1} arcsec converted to a proper distance (in kpc) at the galaxy's redshift. By using a redshift-dependent step size based on the observational reference frame, we can roughly determine the boundaries of our galaxies, assuming, as is possible with the HST, that objects on the order of 0.1 arcsec apart are distinguishable. We continue increasing the radius until the fractional change in enclosed mass is less than

one part in 10^4. Specifically, when ${}^{\Delta M_{\rm enc,i}}/_{M_{\rm enc,i}} < 10^{-4}$, we consider the current radius to be the radius of a single galaxy. Figure 3.2 depict the galaxies associated with an unreprocessed AdaptaHOP halo (left) and the resolved galaxies (right) that result from using this procedure. The approach ensures we do not overrepresent bright objects by considering multiple galaxies as one when computing their luminosities.

To ensure that we capture the faint end of the LF, ignoring simulation resolution effects for now, we also locate and analyze the 'missing' galaxies in our simulation, i.e., those that may have been missed by AdaptaHOP as configured. To accomplish this, we collect the locations of all SP at each redshift that are not within the previously computed radii of AdaptaHOP galaxies. This results in a set of temporarily orphaned SPs. Next, we select an SP from this orphan list and locate all SPs within a 2 kpc comoving radius. If there are none, we assume the star is a galactic outlier, ignore it for the current iteration, and select another SP. Given a collection of SPs within 2 kpc, we compute the center of mass of this set and use this new location with our expanding sphere method to find the extent of the galaxy. If the resulting object has $M_{\rm G} > 10^4\ M_\odot$, its center of mass location and radius are added to the list of galaxies and stored; otherwise, it is ignored. In either case, all of the object's SPs are then removed from the orphan list, and the procedure is repeated until all SPs have been processed.

The final results are depicted in Figure 3.3 where the figure on the left depicts the raw halos, at $z = 12$, detected by AdaptaHop. The figure on the right depicts the halos after running our halo refinement algorithm. As can be seen, many of the larger halos are really multiple individual galaxies since they are more than 0.1 arcsec apart. Additionally, we ignore objects with a stellar mass less than $10^4\ M_\odot$ since these objects are composed of very few (< 10) SPs and are not observable.

Figure 3.4 depicts simulation halos at $z = 12$ and 9; approximately 377 and 559

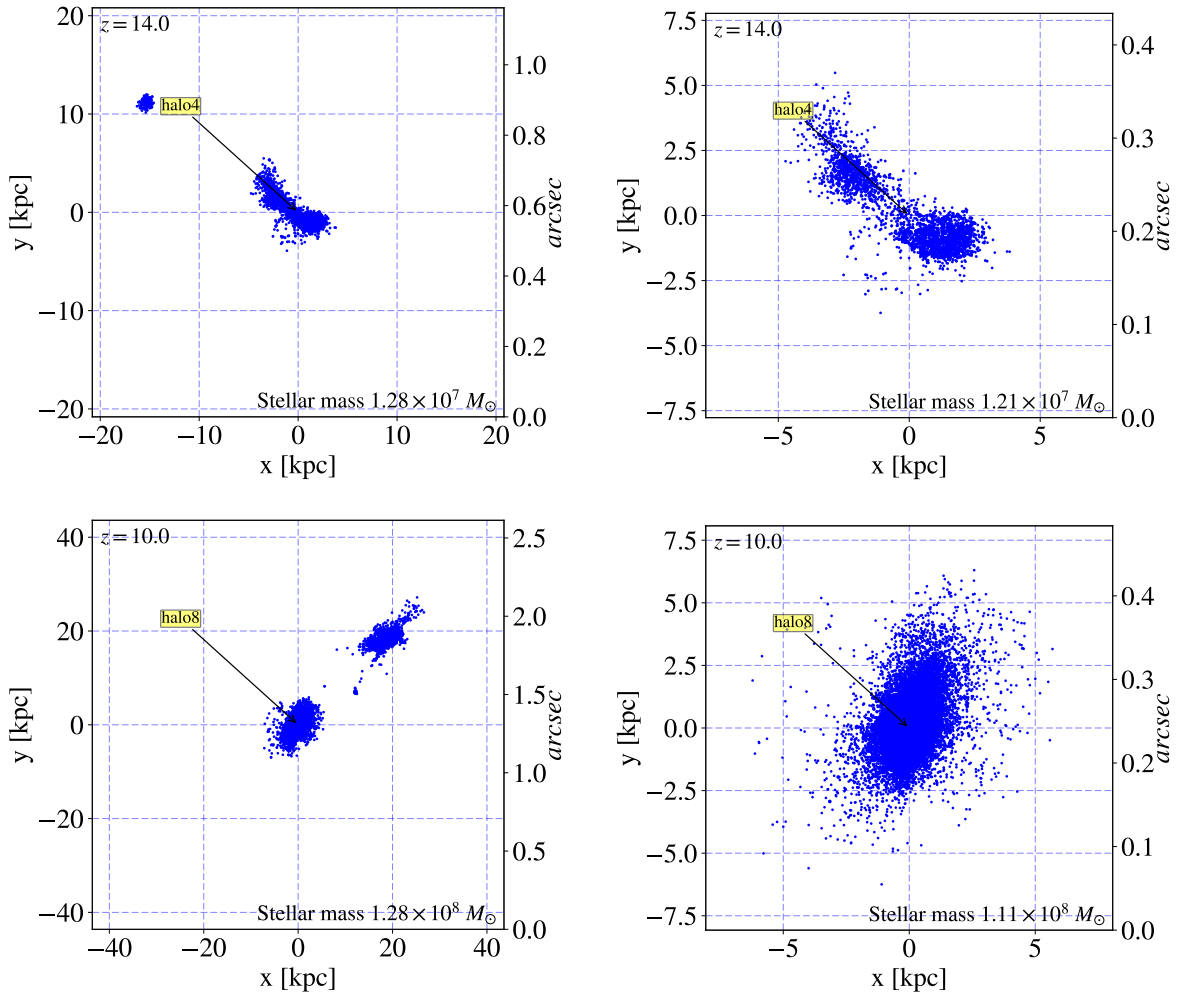

Figure 3.2: Scatter plots of high-redshift galaxies in our simulation. Blue points are SP locations relative to the center of the located halo (coordinate 0,0). The images on the left depict the AdaptaHOP halos found by our modified SP-based algorithm. As can be seen, more than one observationally identifiable galaxy is plotted within the radius depicted. On the right, we have used our post-processing algorithm to correctly identify the larger of the two galaxies in the original field. The smaller galaxy was also identified but not depicted independently in this figure. The scale is comoving kpc and the total mass of the galaxy is identified in the lower-right of each plot. The scale on the right axes indicates the size of the field in arcseconds. Halo numbers, 4 and 8, are for reference and indicate these halos are the 4th and 8th largest, by mass, at the redshifts indicated.

Myr after the big bang, respectively. In this figure SPs are also indicated by blue dots and the location of galaxies by red circles. The size of the circles correspond to the stellar mass of the galaxy with the key in the upper right corner indicating the circle-

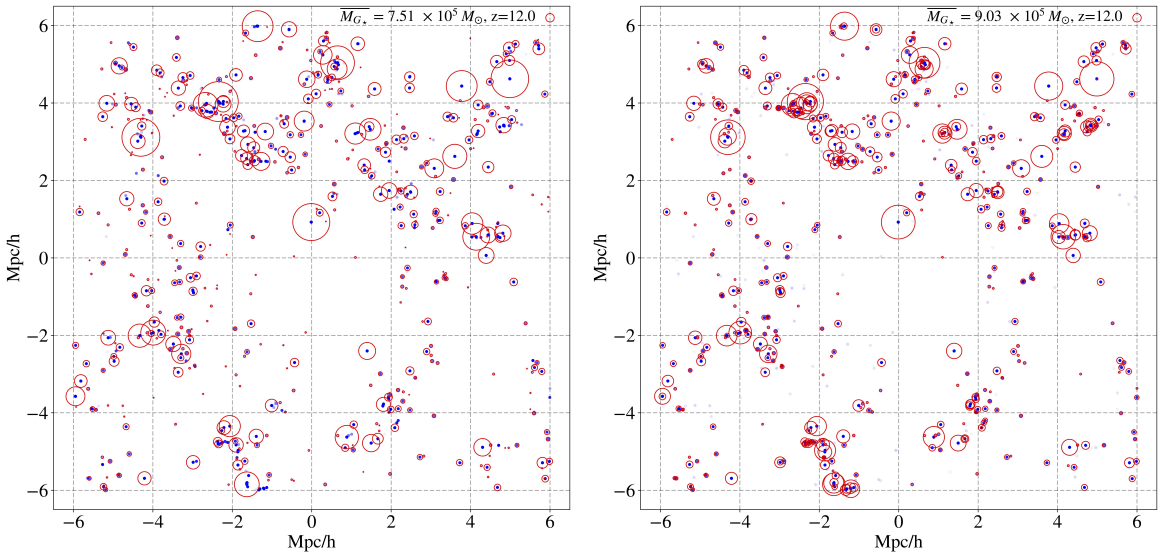

Figure 3.3: Halos before (left) and after running our halo refinement algorithm. Star particles (blue) and galaxies (red circles) in our simulation at $z = 12$. The size of the red circle corresponds to the stellar mass of the galaxy. The circle-size of an average stellar mass galaxy, for the redshift indicated, is indicated in the upper right corner. Our approach identifies halos that are separated by more than 0.1 arcsec. Additionally, we ignore objects with a stellar mass less than $10^4\,M_\odot$ since these objects are composed fewer than 10 SPs. Scale is comoving Mpc/h.

size for an average-mass galaxy at the redshift depicted. Looking at the number of halos we note that there is a burst of star formation, mainly in new halos that are just crossing the star forming density threshold, at $z = 9$. After this time, star formation is quenched in smaller, unshielded halos by reionization, which completes at $z \approx 8.5$ in our simulation.

3.2.5 Galaxy Spectral Models

The rest-frame UV and filter fluxes of our simulated galaxies are functions of the ages, metallicities, and masses of their constituent SPs. We calculate our SP luminosities using a set of simple stellar population (SSP) SED models spanning the particles' ages and metallicity range. Our SEDs are based on *STARBURST 99* (Leitherer et al., 2014), henceforth *SB99* along with Raiter et al. (2010) and Schaerer

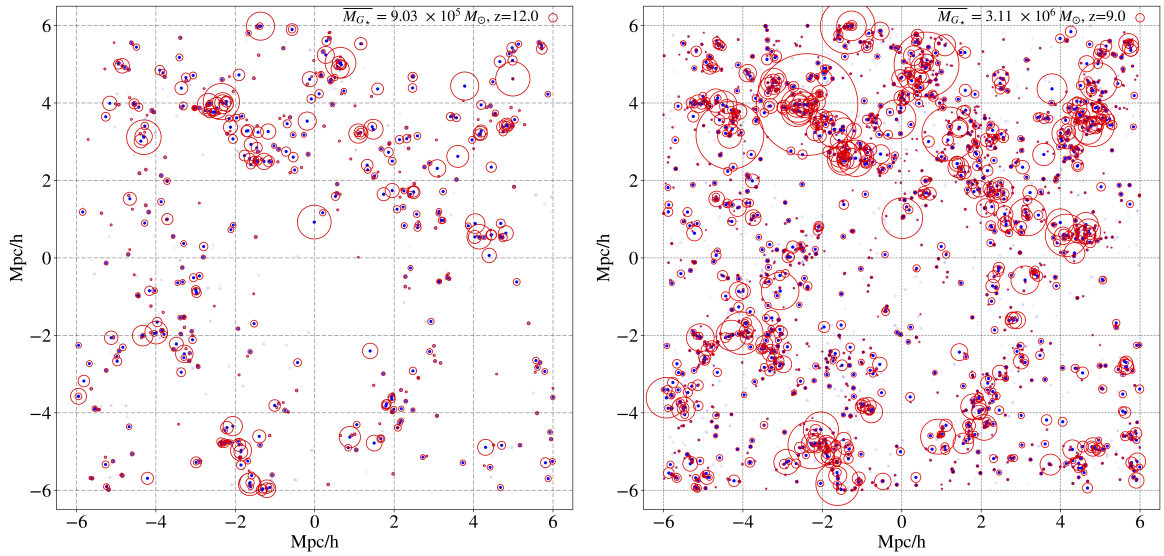

Figure 3.4: Observable galaxies in our simulation at $z = 12$, left, and $z = 9$, right. Symbology is as described in Figure 3.3. There are 538 galaxies at $z = 12$ and 2111 at $z = 9$. Scale is comoving Mpc/h.

(2003), henceforth *R10*. For the fraction of all SPs with $Z_\star \geq Z_{\rm crit}$ our SEDs model a Salpeter (1955) IMF normalized to $1\,M_\odot$. Since we have a precise age for each star particle, our SEDs model instantaneous bursts across the age range of SPs in the simulation. Pop III SP fractions with $Z_\star < Z_{\rm crit}$ are modeled using a log-normal IMF, again normalized to $1\,M_\odot$ and are based on the *R10* SEDs for a zero-metallicity population. The log-normal IMF is centered on a characteristic mass of $60 M_\odot$ with $\sigma = 1.0$ and a mass range $1\,M_\odot \leq M \leq 500\,M_\odot$. Conceptually, Pop III stars include the mass of SPs with corrected metallicities $0 < Z_\star < Z_{\rm crit}$ as well as the fractional mass of pristine stars, $P_\star \times M_\star$, with $Z = 0$, that represent the mass fraction of Pop III stars born in cells with incomplete mixing. Since $P_\star$ captures the fraction of stellar mass with $Z_\star < Z_{\rm crit}$ the total mass of Pop III stars in each of our simulated galaxies is

$$M_{\star,\rm III} = \sum_{n=1}^{N} P_{\star,n}\, M_{\star,n}, \tag{3.5}$$

where N is the total number of SPs in a galaxy and $M_{\star,n}$ is the mass of each SP.

Our *SB99* SEDs were generated over an age range of 10 kyr to 0.78 Gyr, the age of the universe at $z = 7$, in linearly spaced steps of 0.5 Myr. Each SED covers the wavelength range $91 - 1.6 \times 10^6 \mathring{A}$. We generated SEDs for metallicities of 0.02, 0.2, 0.4, and 1.0 $Z_\odot$, for each age, using the *SB99*-implemented Padova (Girardi et al., 2000) models that include stellar and nebular emission through the onset of the thermal pulse assymtotic giant branch phase of stellar evolution. We supplemented the *SB99* model with a set of *R10* models for stars with $Z = 5 \times 10^{-4}$ and 5×10^{-6} $Z_\odot$. This allows us to interpolate over the range $Z_{\rm crit} \leq Z_\star \leq Z_\odot$. The Pop III SEDs, by *R10*, are based on $Z = 0$ and cover the age range 10 kyr to 1 Gyr in steps of 1 Myr. Again, the spectrum of all stars with $Z_\star < Z_{\rm crit}$ is modeled using this SED.

Figure 3.5 depicts a sample of the rest-frame SEDs used in our analysis. The grey vertical dashed-lines in the plots indicate the rest-frame 1500 $\mathring{A}$ luminosity: our ultra-violet reference point for this study. We include the 5 Myr old Pop III SED in the plots for $Z > 0$ to illustrate how quickly the Pop III UV luminosity falls-off with age. Stars with $Z > 0$ have more UV flux than Pop III stars of the same age after $\approx$ 3 Myr.

In order to compute the observational flux, we redshift each of our SEDs over the range z=7 to 16 applying Lyman forest and continuum absorption as described in Madau (1995). Figure 3.6 depicts our implementation of this Lyman absorption model for a sampling of redshifts. This process, along with a spectral conversion from wavelength to frequency, transforms the rest-frame *SB99* and *R10* SEDs (erg/s/$\mathring{A}$/$M_\odot$) into observational fluxes (erg/s/Hz/cm^2/$M_\odot$) across the range (in redshift, age, and metallicity) of our SP. Equation (3.6) describes this conversion from rest-frame luminosity to observational flux for objects at cosmological distances,

$$f(\nu, z) = \frac{L_\nu(\nu_e)}{4\pi D_L^2}(1+z)\,\mathcal{M}(\nu_o, z), \tag{3.6}$$

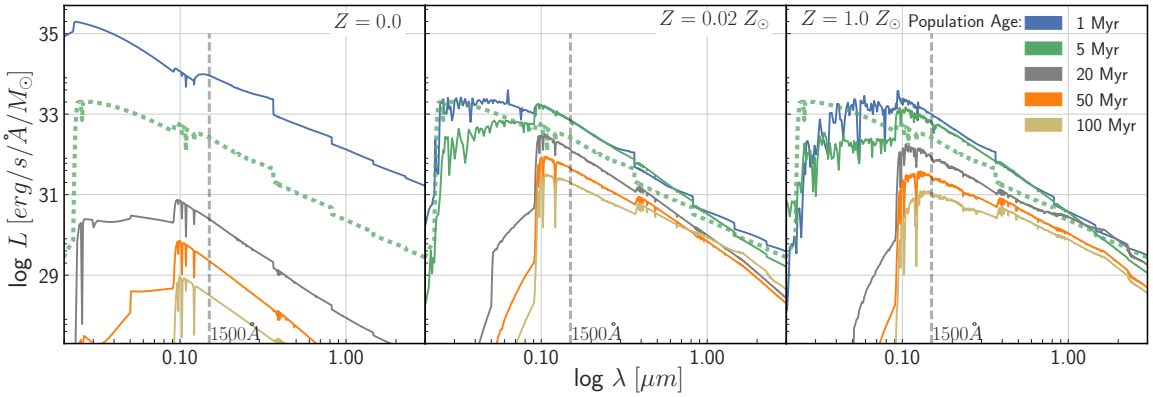

Figure 3.5: Representative SEDs used to compute the filter and UV fluxes in our study. The grey dashed vertical lines indicates the 1500 $\mathring{A}$ (our UV reference wavelength) luminosity for the models. The green dotted lines are the zero metallicity Pop III 5 Myr SED – included for easy comparison. The UV flux from young Pop III stars dominates for less than 5 Myr. In fact Pop III stars older than $\approx$ 3 Myr produce less UV flux than $Z > 0$ populations with the same age.

where the ν_o and ν_e are in Hz and refer to the observed and emitted reference frames, respectively; D_L is the luminosity distance; and $\mathcal{M}(\nu_o, z)$ is the Madau (1995) Lyman absorption function. We also generate the flux at a distance of 10 pc to facilitate the generation of absolute magnitudes. This is done by setting $z = 0$, $D_L = 10$ pc and $\mathcal{M}(\nu_o, z) = 1.0$ in equation (3.6).

We then convolve these bolometric fluxes with the set of JWST and HST filters listed in Table 3.1. We also compute the rest-frame UV flux at 1500$\mathring{A}$. The observational fluxes are computed as follows:

$$\mathcal{F}(R, z) = \frac{\int_{-\infty}^{\infty} f(\nu, z) R(\nu) \frac{d\nu}{\nu}}{\int_{-\infty}^{\infty} R(\nu) \frac{d\nu}{\nu}}, \tag{3.7}$$

where $f(\nu, z)$ is the flux at redshift z, $R(\nu)$ is the filter response function, and $\mathcal{F}(R, z)$ is the resulting bandpass flux. For the rest-frame UV flux, the filter response function is the simply the Dirac delta function shifted to the observational UV wavelength, $\nu_{\rm UV} = {}^{c}/_{(1+z)1500\mathring{A}}$, resulting in $R(\nu) = \delta(\nu - \nu_{\rm UV})$ which simplifies equation (3.7) to $\mathcal{F}(R, z) = f(\nu_{\rm UV}, z)$. The result is a set of filter-flux tables that span the range of redshifts, ages, and metallicities for a normalized star of $1 M_\odot$ representing the

Table 3.1: Filters modeled in this work

System	Filter names
JWST NIRCam	F150W, F200W, F277W, F356W, F444W
HST WFC3	F125W, F160W
Restframe UV	1500 $\mathring{A}$

Salpeter IMF, for $Z_\star \geq Z_{\rm crit}$, and the log-normal IMF for $Z_\star < Z_{\rm crit}$. This set of filter-flux tables for each redshift can be interpolated (in two dimensions) over the range of SP ages and metallicities found in the simulation.

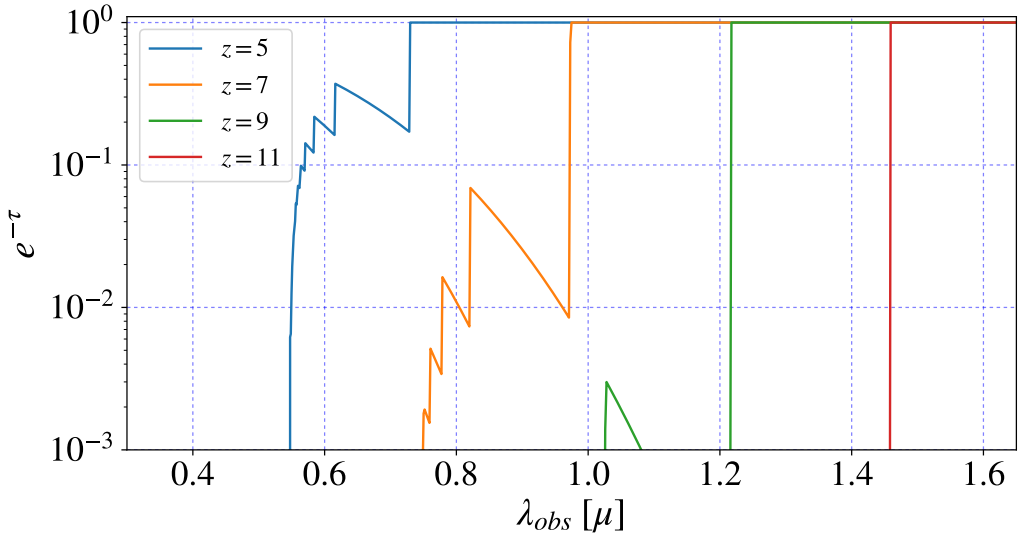

Figure 3.6: Our Lyman absorption model expressed as a transmission function of observed wavelength. The model is based on Madau (1995).

3.2.6 Simulated Observations

We interpolate the filter and rest-frame UV fluxes linearly in log-space as a function of both SP metallicity and age in order to compute the bandpass and rest-frame UV flux of our galaxies at each redshift. The resulting fluxes are then scaled by the

mass of each SP, accounting for $P_\star$, and summed to compute the total flux (in each filter) for the galaxy. We then transform the filter fluxes into AB magnitudes.

3.3 Results

In this section, we present the characteristics of our simulated galaxies. We focus on $7 \leq z \leq 15$. Figure 3.7 depicts the star formation rate density (SFRD) for our simulation, along with an observationally derived SFRD from Madau & Dickinson (2014). While our SFRD is higher than observations at $7 \leq z \leq 8$ it agrees with the LF-based SFRD described by Finkelstein (2016) when considering sample variance (Trenti & Stiavelli, 2008, see §3.3.2 for a discussion on error estimation). The LF-based SFRD is based on an integration of the reference luminosity function in that work to $M_{\rm UV}$ = -13 mag. Since the observationally based SFRD is likely undersampled at $z > 7$ (Oesch et al., 2015), the LF-based SFRD is likely a more appropriate estimate of star formation at high redshift.

The figure also depicts the Pop III SFRD as well as (what we call) the "classical" Pop III SRFD that does not include the effects of modeling the evolution of P. We see that modeling the pristine fraction increases the SFRD for Pop III stars by an average factor of 2.5 for $z \leq 16$. As we discuss below, a relatively small increase in the fraction of young Pop III stars can have a significant impact on the luminosity of early galaxies.

There is a rapid increase in the star formation rate immediately before reionization ($z_{reion} \approx 8.5$) that correlates with an even greater increase in the Pop III star formation rate. This is caused by a significant number of new, small halos crossing the density threshold for star formation. At $z = 9$ the number of star forming halos is 2112. By $z = 8$ that number rises to 6807, more than a factor of 3 increase in ≈96 Myr. While the overall star formation rate rises by a factor of approximately

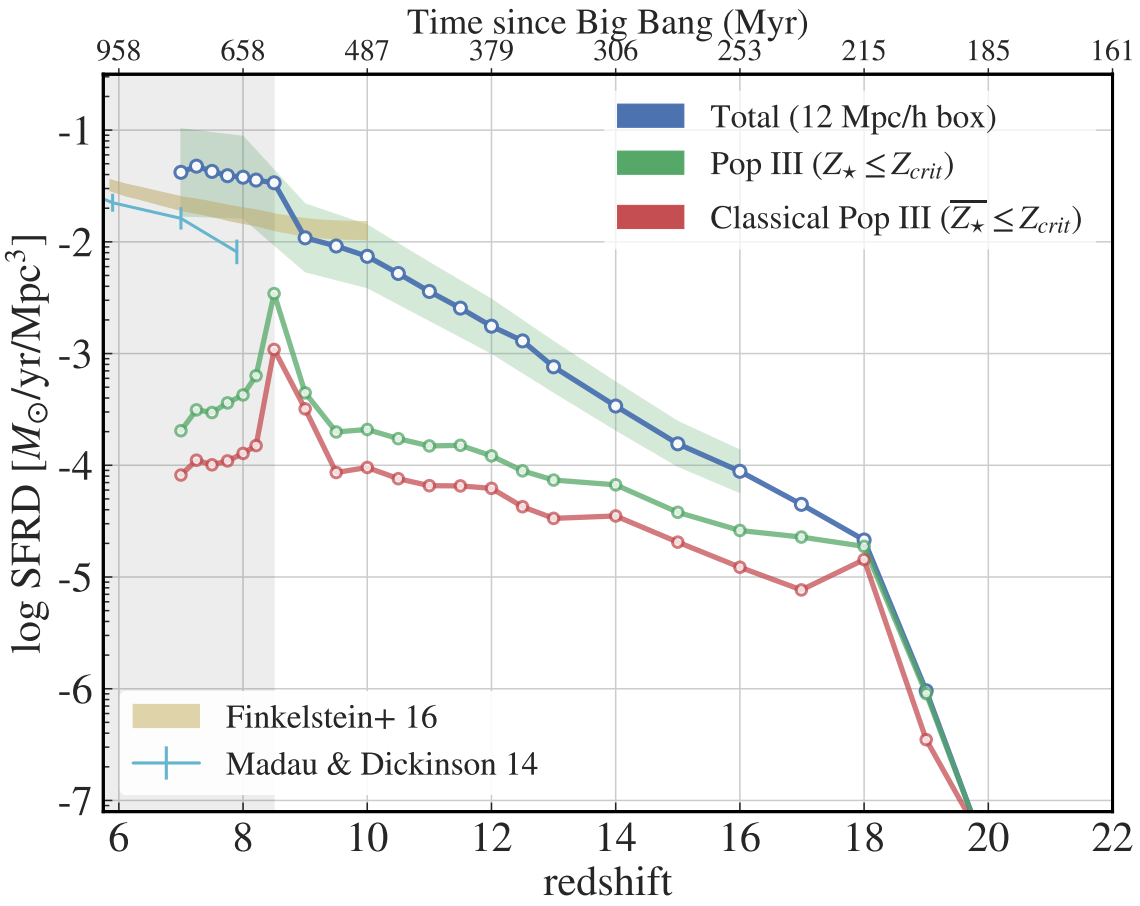

Figure 3.7: The 1σ uncertainty on the overall SFRD is also depicted (light-blue) out to $z = 16$. While our SFRD is above observations at $z \leq 8.5$, it agrees with the LF-based SFRD that incorporates galaxies down to $M_{\rm UV} = -13$ mag when considering both Poisson and sample variance, 1σ. The grey-shaded area indicates redshifts post-reionization.

3.5 from $z = 9$ to $z = 8$, the Pop III rate increases by a factor of 4.4 over this same interval. Additionally, the fraction of Pop III stellar mass in our simulation box at $z = 8.5$ increases to 7% from 4% at $z = 9$.

3.3.1 The Galaxy Mass-Metallicity Relation

While the galaxy mass-metallicity relation at $z \geq 7$ is beyond current observational limits (Zahid et al., 2013; Henry et al., 2013; Maiolino et al., 2008), Figure 3.8 depicts this relationship for a sample of redshifts in the range $7 \leq z \leq 15$ for

our simulated galaxies. The plots display the normalized probability per mass-bin, $\sum_{\text{bin}} {}^{P(\overline{Z_{\text{G}}}/Z_{\odot})}/_{d(M_{DM}/M_{\odot})} = 1.0$, of finding a galaxy with a metallicity in the range depicted on the vertical axis. Here, we use the halo DM mass for the galaxies. The figure clearly depicts the expected mass-metallicity trend but, more importantly for this work, the mass range of Pop III galaxies in the bottom row of bins in each plot, at each redshift. Each galaxy's average metallicity, $\overline{Z_{\text{G}}}$, is computed using the corrected SP metallicities described by Equation (4.3). Note that $\overline{Z_{\text{G}}}$ is computed directly from the mass-weighted average metallicity of the SPs that populate each galaxy and not from synthetic observations of galaxy spectra. Pop III galaxies, composed of SPs such that the average metallicity of the galaxy is subcritical, have been grouped at $\overline{Z_{\text{G}}} < 10^{-5} Z_{\odot}$. We analyze halos with masses down to $M_{\text{G}} = 4.62 \times 10^{7} M_{\odot}$ that consist of approximately 330 DM particles.

Taken as whole, we see that Pop III galaxies are not very massive and are comparable to the theoretical limits, $1.5 \times 10^{8} M_{\odot}$ to $1.1 \times 10^{9} M_{\odot}$, discussed in Yajima & Khochfar (2017) for $z = 7$. The most massive Pop III-dominated galaxies in our simulation occur at $z = 9$ and 10, before reionization. They have an average DM mass of $\overline{M_{\text{G}}} = 1.2 \times 10^{9} M_{\odot}$ and make up less than 3% of all galaxies with masses $M_{\text{G}} > 10^{9} M_{\odot}$.

At lower redshift, $z = 7$ and 8, Pop III galaxies span a smaller mass-range where the most massive, less than 1% of all Pop III galaxies, have $M_{\text{G}} \gtrsim 4.6 \times 10^{8} M_{\odot}$. At the other end of the mass range, we see the recently formed, purely Pop III galaxies with $M_{\text{G}} < 10^{8} M_{\odot}$. At $z = 7$ and 8 fully 69% and 54% of Pop III galaxies, respectively, are associated with these mini-halos. This is likely because the rate and location of Pop III star formation has changed between $z = 9$ and $z = 8$. The Pop III SFRD turns over at $z_{\text{reion}} = 8.5$ and the Pop III fraction is no longer keeping pace with overall star formation.

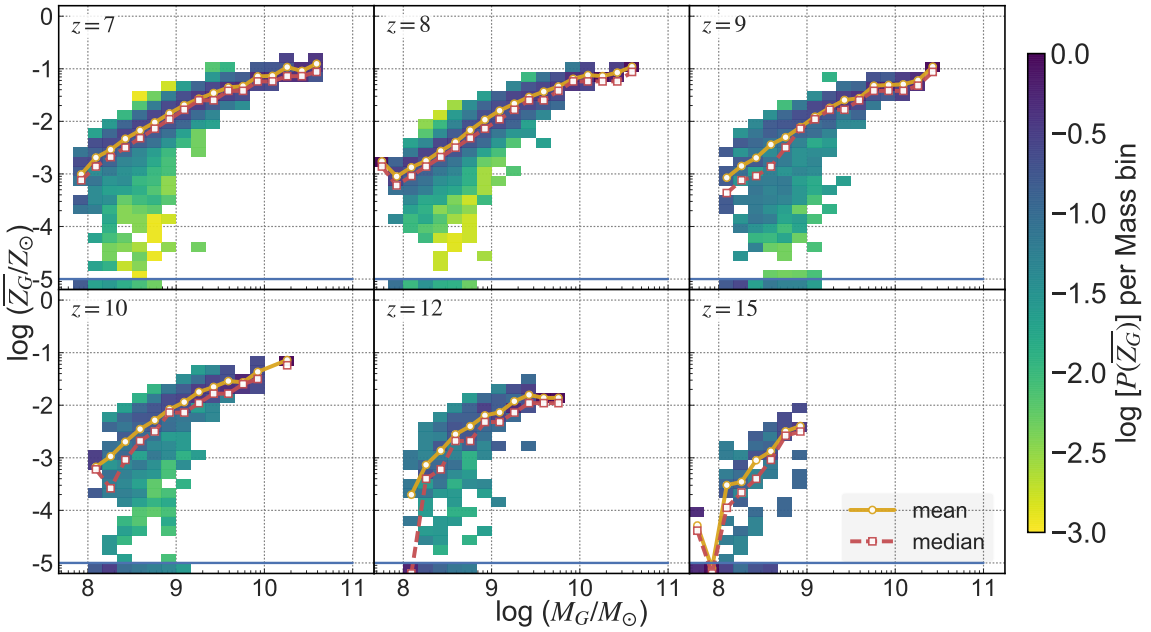

Figure 3.8: The normalized probability, in each mass bin, of finding a galaxy with a metallicity in the range $1 > Z_{\rm G} \geq 9 \times 10^{-6} Z_\odot$ where we have binned all Pop III galaxies immediately below $Z_{\rm crit} = 10^{-5} Z_\odot$ (blue line). The dark yellow line identifies the mean metallicity and the red dashed-line the median. Pop III galaxies with $M_{\rm G} > 10^9 M_\odot$ are exceedingly rare within our simulation volume (≈ 4800 Mpc^3, comoving) occurring only in the range $9 \leq z \leq 10$. At $z = 8$ we see a large number of small Pop III galaxies that formed immediately before reionization with masses less than $10^8 M_\odot$.

While the majority of new star formation is taking place within larger, shielded galaxies – and within gas that has been polluted to levels above $Z_{\rm crit}$ – we also see the results of the Pop III starbursts in new, mini-halos immediately before $z = 8.5$.

The low masses of purely Pop III protogalaxies in the range $8 \leq z \leq 11$, today's high-redshift frontier, partially explain the difficulty in finding Pop III galaxies. However, as we shall discuss, a small percentage of young Pop III stars can contribute a significant fraction of a galaxy's flux.

3.3.2 Error Estimation

We briefly describe the error estimation for both the luminosity functions and for the overall SFRD. Error estimates include both Poisson errors (shot noise) and the 1σ uncertainty in galaxy counts due to sample variance (Trenti & Stiavelli, 2008) and are computed per luminosity bin. For the SFRD the process is the same except all galaxies are essentially in one bin per redshift.

The total error in each bin is

$$v_r = \sqrt{\sigma_v^2 + 1/N}, \tag{3.8}$$

where the sample variance

$$\sigma_v^2 = (\bar{b})^2 \, \sigma_{\rm box}(z)^2 \tag{3.9}$$

is the product of the average galaxy bias, $\bar{b}$, based on Press & Schechter (1974), and the fluctuation amplitude, $\sigma_{\rm box}(z)$, for the simulation volume at redshift z. The shot noise is $1/N$.

In turn, the average bias is derived from the mass of each galaxy in the bin,

$$b = 1 + \frac{(\nu^2 - 1)}{1.69}, \tag{3.10}$$

where

$$\nu = \frac{1.69}{\sigma(M, z)} \tag{3.11}$$

and $\sigma(M, z)$ is the fluctuation amplitude of a galaxy of mass M at redshift z.

Lastly, the DM mass in collapsed objects, at each redshift, matches the prediction in Barkana & Loeb (2001) to within -3% to +6% at $z \leq 10$. The greatest difference is at $z = 12$ to 15 where the simulation has 12 to 14% more mass in halos than predicted by theory resulting in a slight overestimate of the sample variance at $z \geq 12$.

3.3.3 *Luminosity Functions*

Galaxy observations are characterized by their flux – which in turn is determined by the galaxy's stellar populations. A small fraction of hot, young Pop III stars can contribute a large fraction of the galaxy's luminosity. However, only the Pop III stars with ages < 3.5 Myr contribute more flux than their polluted cousins, so detecting a galaxy dominated by Pop III flux means looking for a recent starburst such that a significant fraction of the flux from the entire galaxy is coming from these types of stars. We next look at the luminosity functions and Pop III flux-fractions derived from our simulation data.

Given our total simulation volume of 4828 Mpc^3 we have data down to $\phi \approx 2 \times 10^{-4}$ mag^{-1} Mpc^{-3}. Further, since star formation in our simulation is resolution-dependent we cannot track galaxy formation at scales below $\approx$ 260 pc, physical. While such a small proto-galaxy is likely not detectable, even by JWST, it does prevent us from characterizing the turnover at the faint end of the LF. Additionally, several such mini-halos may merge producing larger numbers of fainter galaxies than reported here. Within this context, Figure 3.9 depicts the UV luminosity functions for all of our galaxies down to $M_{\mathrm{UV}} = -13$ mag where the galaxy counts per magnitude bin begin to decrease due to the simulation's limited resolution.

We have included both observationally-derived and extrapolated Schechter (1976) functions by Finkelstein (2016) for reference: Solid grey lines indicate Schechter functions derived from observations, while grey-dashed lines are an extrapolation of the Schechter parameters – also from Finkelstein (2016). Schechter parameters for the observational data and extrapolations are listed in Table 3.2. We have also included observational data from Bouwens et al. (2015) and Oesch et al. (2013) along with data from an analysis of galaxies in the Renaissance Simulations by O'Shea et al.

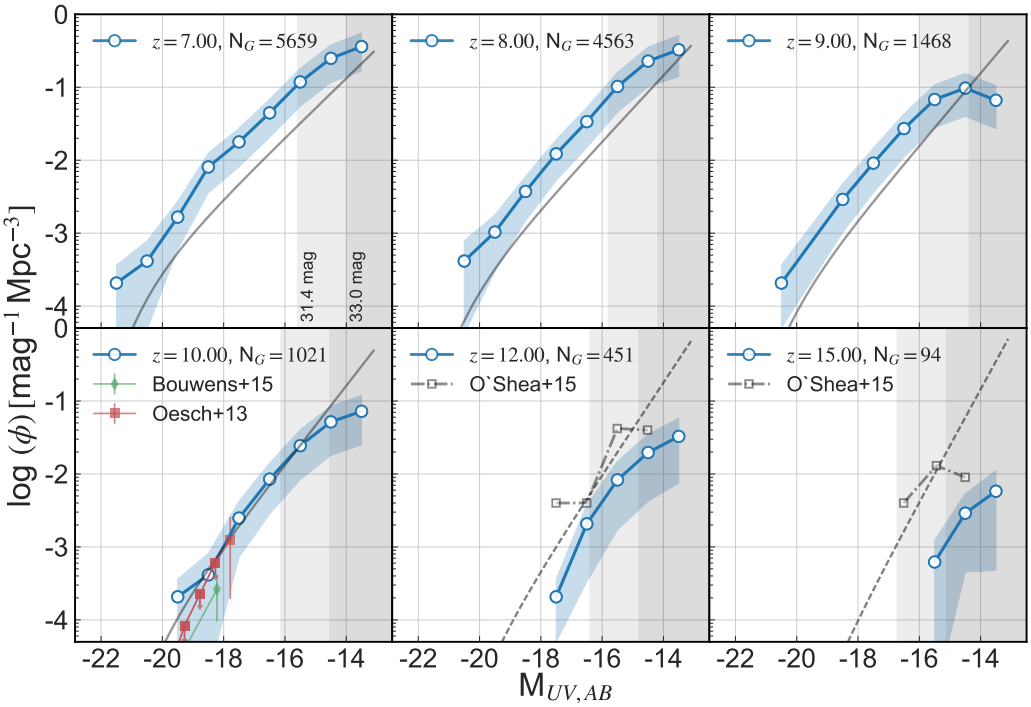

Figure 3.9: UV luminosity functions derived from our simulation with 1σ error bounds including both Poisson noise and sample variance. Dark grey lines are Finkelstein (2016) Schechter fits. Dashed-grey lines are Schechter functions based on an extrapolation of the Schechter parameters also found in that work. For $z = 10$, we have included Bouwens et al. (2015) and Oesch et al. (2013) points based on observations, with error bars. For redshifts 12 and 15 we have included luminosity functions derived from the Renaissance Simulations by O'Shea et al. (2015). The shaded areas indicate the regions where $m_{\rm UV} > 31.4$ mag, a likely limiting magnitude for a JWST ultra-deep campaign and $m_{\rm UV} > 33$ mag, a likely lensing limit.

(2015).

We note that all of our LFs at $z < 10$ lie slightly above the faint end of observationally-derived Schechter functions. However, it should be noted that data from our simulation includes many faint objects for which the observationally-derived models suffer from the greatest uncertainty. Furthermore, although our simulation box represents an average density region of the universe, the variance in initial conditions could have resulted in more overdensities with a scale that is responsible for the increase in star formation at $z \approx 9$.

Additionally, we do not account for dust. Dust attenuation in high redshift galax-

Table 3.2: Schechter Function Parameters

z	$\log(\phi^*)$	α	$M^*_{\rm UV}$
8	-3.75	-2.13	-20.52
9	-3.94	-2.24	-20.39
10	-4.13	-2.35	-20.25
11	-4.29	-2.47	-20.11
12	-4.49	-2.58	-19.98
13	-4.69	-2.69	-19.84
14	-4.89	-2.81	-19.71
15	-5.08	-2.92	-19.57
16	-5.28	-2.03	-19.44

Schechter function parameters for the reference lines in the luminosity function plots. Data is from Finkelstein (2016). Values at $z > 10$ have been extrapolated based on a linear fit to the parameters in that work.

ies is uncertain at best (Cullen et al., 2017; Cowley et al., 2018; Calzetti, 2001) and we have not included its effects in any of our plots. However if we extrapolate work by Schaerer et al. (2015) at $z \approx 6.8-7.5$ to $z = 8-10$, we would expect $A_{\rm UV} \approx 1.1 \pm 0.2$ of UV dust attenuation. Including this level of dust attenuation would reduce our absolute magnitudes by ≈ 1 and bring our data more in-line with the faint end slope at these redshifts.

Our LFs closely follow the predicted faint end slope, α, at $z = 10$ and are in reasonable agreement with both the extrapolated Schechter function and data from the Renaissance Simulations at $z = 12$. Again, these Schechter curves (grey dashed lines) are based on a linear fit and extrapolation of the trends in M^*, α, and $\log \phi^*$ using observational data over the range $4 \leq z \leq 8$. Although we have no data at the bright-end of the LF, due to our small volume, we feel our LFs are reasonably representative of galaxy populations, in the range plotted, for an average-density

region of the universe.

3.3.4 Pop III Flux

Since we are mainly concerned with the search for Pop III stars, we focus our analysis on more detailed characteristics of our galaxies. Figure 3.10 depicts the normalized probability of finding a Pop III flux fraction, as measured at 1500$\mathring{A}$ in the rest-frame, in the range $10^{-3} \leq {}^{f_{\rm III}}/_{f_{\rm Tot}} \leq 1$ for our galaxies as a function of magnitude and redshift. When ${}^{f_{\rm III}}/_{f_{\rm Tot}} < 10^{-3}$ we have mapped the value to 10^{-3}. Note that probabilities are computed independently for each magnitude bin, as was done for the galaxy mass-metallicity relation.

The topmost row of bins in each plot represent a Pop III flux fraction of at least 75%: $P({}^{f_{\rm III}}/_{f_{\rm Tot}} \geq 0.75)$, while the next row down indicates a flux fraction $P(0.75 > {}^{f_{\rm III}}/_{f_{\rm Tot}} \geq 0.50)$. Note that combining the probabilities in the 50% and 75% bins does not change the probabilities significantly from considering the 75% bins alone. Hence we use 75% as our definition of "significant Pop III flux" and a "Pop III–bright galaxy". Magnitude bins are labeled at their right edge and are 1 magnitude wide. Below we reference a magnitude bin by its right (dimmer) edge.

At redshift 7, only 2% of galaxies with binned absolute magnitudes of -13, -14 and -15 are Pop III–bright. Similarly, at $z = 8$ less than 1% of galaxies are Pop III–bright and have $M_{\rm UV} = -16$ mag. However, as we move to the era before reionization, approximately 18% of our galaxies at $z = 9$ with $M_{\rm UV} = -15$ mag (corresponding to $m_{\rm UV} \approx 31.4$ mag at this redshift) are Pop III–bright and 11% have $M_{\rm UV} = -17$ mag. This correlates with our observation of the increase in the SFRD at this epoch. At $z = 10$, we find that the fraction of Pop III–bright galaxies drops to $\approx 8\%$ with $M_{\rm UV} = -15$ mag and 7% with $M_{\rm UV} = -16$ mag. As we move to $z = 12$, about 10% of the faint objects ($M_{\rm UV} = -16$ mag) are dominated by Pop III flux. At $z = 15$ the

brightest Pop III–bright galaxies have $M_{\rm UV} = -14$ mag but represent 50% of galaxies at that absolute magnitude.

The results discussed so far include Pop III stars created in cells in which the subgrid turbulent mixing of metals was incomplete, resulting in the enhanced Pop III SFRD we see in Figure 3.7. The bottom row of Figure 3.10 depicts the Pop III flux fraction for our galaxies when constraining Pop III star formation to cells with $\overline{Z} < Z_{\rm crit}$. This is the no-mixing or classical Pop III case. When considering only the classical Pop III SPs we see that the enhancement of the Pop III SFRD due to our subgrid turbulent mixing model, an average of $\approx 2.5\times$ the classical rate, is responsible for a significant amount of flux at several redshifts.

For instance, considering all 'classical Pop III galaxies' at $z = 9$, only 7% of galaxies with $M_{\rm UV} = -15$ mag are Pop III–bright, as compared to the 18% we discuss above when we consider Pop III stars created in regions of incomplete mixing. The subgrid model results in ≈ 2.6 times more Pop III bright galaxies at this redshift and absolute magnitude. This result points to the importance of accurately modeling Pop III star formation since small changes in their density can significantly effect the predicted fraction of Pop III flux.

Next, we consider the overall fraction of observable galaxies in the simulation that are Pop III–bright, at each redshift. Figure 3.11 identifies the joint probability that a galaxy has at least a 75% Pop III flux fraction and $m_{\rm UV} \leq 31.4$ mag, which we take as the limiting magnitude for the un-lensed JWST ultra-deep campaign, as a fraction of all galaxies with $m_{\rm UV} \leq 31.4$ mag. We refer to these galaxies as "observable Pop III–bright galaxies". As we would expect from current surveys, at relatively low redshift, $7 \leq z \leq 8$, the fraction of Pop III–bright galaxies is less than 2%.

Going deeper, we again see the relatively large increase in the number of Pop III–bright galaxies at $z = 9$, immediately after a burst of Pop III star formation, where

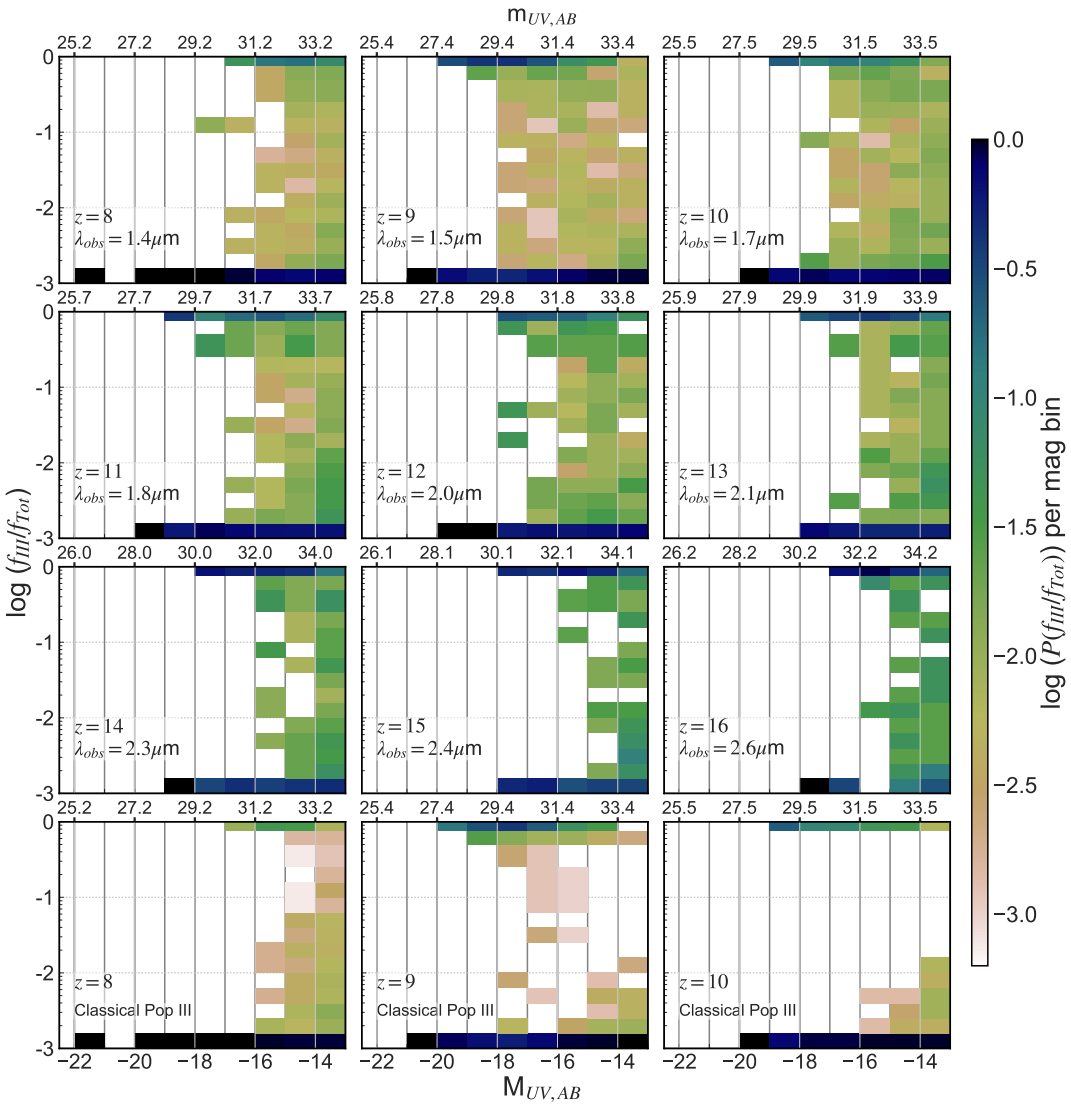

Figure 3.10: The normalized probability of finding a UV Pop III flux-fraction, $f_{\rm III}/f_{\rm Tot}$, as a function of the redshift and magnitude of our galaxies. When $f_{\rm III}/f_{\rm Tot} < 10^{-3}$ we map the value to 10^{-3}. Probabilities are computed independently for each magnitude bin. Bins are labeled at their right edge. The top-most row of bins in each plot represent a Pop III flux-fraction of at least 75%. The second row of bins represent $.75 > f_{\rm III}/f_{\rm Tot} \geq 0.50$. At $z = 9$, we find that 30% of galaxies at $M_{\rm UV} \leq -16$ mag have $f_{\rm III}/f_{\rm Tot} \geq 75\%$. The bottom row of plots depict the Pop III flux-fraction from our galaxies when only considering stars created in cells with $\overline{Z} < Z_{\rm crit}$, the classical Pop III case. Modeling the evolution of the pristine gas faction at subgrid scales results in a Pop III SRFD that is a factor of 2.5 increase over the classical rate and these luminous stars contribute a significant fraction of the flux of these young galaxies. Axis labels along the top axis are observed UV magnitude, $m_{\rm UV}$. We identify λ_{obs} at each redshift: the wavelength of the 1500$\mathring{A}$ reference in the observational frame.

17% of observable galaxies are Pop III–bright. This is the epoch immediately before reionization when smaller mini-halos begin to cross the star-forming mass-density threshold. It is during this epoch that we predict the largest fraction of detectable Pop III–bright galaxies.

After reionization, the star-forming threshold is raised quenching star formation in these mini-halos. This result points to the importance of determining the reionization redshift since most Pop III–bright galaxies are likely to be found just before it completes.

At $z = 10$ we note that less than 5% of our observable galaxies are Pop III–bright. At $z > 10$ there are no Pop III–bright galaxies with $m_{\rm UV} \leq 31.4$ mag. To find Pop III–bright galaxies we have to go to $m_{\rm UV} = 33$ mag, an intrinsic magnitude that may be within reach of a lensed JWST field.

To once again illustrate the observational effects of our subgrid model, Figure 3.11 also identifies the fraction of observable Pop III–bright galaxies when we only account for classical Pop III stars created in simulation cells with $\overline{Z} < Z_{\rm crit}$. As can be seen the subgrid models' resulting enhancement to galactic Pop III flux is evident over the redshift range $7 \leq z < 11$. Comparing results in the redshift range $9 \leq z \leq 10$ we note that the fraction of observable Pop III–bright galaxies is, on average, $2\times$ higher for our subgrid model than for the classical Pop III case. Again, this exemplifies the importance of modeling Pop III star formation accurately since it has a significant effect on the density of Pop III–bright galaxies we expect to detect at high redshift.

Most of the Pop III–bright galaxies form at the border of polluted areas or in regions of pristine gas away from larger halos. While our sample volume is relatively small, this result points out that Pop III–bright galaxies can be found both in relative isolation and near other, often larger galaxies with $\overline{Z}_{\rm G} > Z_{\rm crit}$. Once again, modeling the mixing time required to pollute the gas above $Z_{\rm crit}$ is important here.

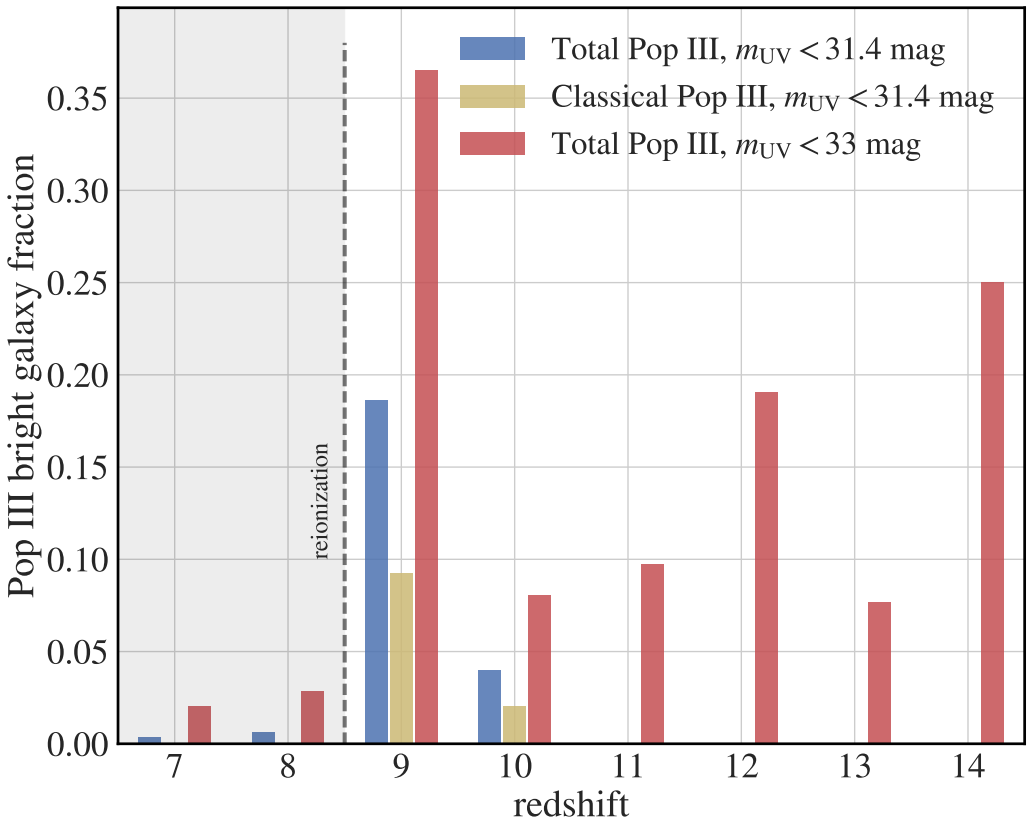

Figure 3.11: The blue bars indicate the joint probability of finding an observable ($m_{\rm UV} \leq 31.4$ mag) Pop III–bright galaxy as a fraction of all observable galaxies, as a function of redshift. The yellow bars ignore the effects of our subgrid model and its enhancement to the Pop III SFRD. The resulting reduction in Pop III flux is visible across $7 \leq z < 11$. The red bars also depict this joint probability but for a limiting intrinsic magnitude of $m_{\rm UV} = 33$ mag. The burst of Pop III star formation immediately before reionization is apparent at $z = 9$.

By examining fainter galaxies we can find a larger fractions of galaxies with significant Pop III flux at higher redshift. Figure 3.11 also depicts characteristics of galaxies that have at least 75% of their flux coming from Pop III stars while requiring that $m_{\rm UV} \leq 33$ mag, approximately the JWST 10x lensing limiting magnitude. With these criteria we note that at $z = 11$ the fraction of Pop III–bright galaxies is only 9%, the result of more galaxies dominated by Pop II flux meeting the criteria $m_{\rm UV} \leq 33$ mag. However, at $z = 12$ the fraction of observable Pop III–bright galaxies jumps to 18% as a result of going to this intrinsic magnitude with lensing. At $z = 14$ about

25% of galaxies are Pop III–bright. If there are enough lensing opportunities JWST should detect a relatively high (about one in four) fraction of Pop III–bright galaxies at $z = 14$.

3.3.5 Observational Predictions

In this section we discuss predictions for the space telescopes and filters described in Table 3.1. As with the rest-frame UV flux, we have not modeled dust for the results presented in this section.

The LFs derived from our simulated bandpasses are depicted in Figure 3.12 and cover the redshifts $z = \{9, 10, 12\}$. If a particular redshift is not depicted it is because there was no flux in the bandpass. For each of these plots we indicate the JWST magnitude cutoff for the deep campaign, 31.4 mag, at redshifts $z = 9$ and 12 using dark and light grey regions, respectively.

The HST F125W filter, due to Lyman forest absorption, was unable to detect any of our galaxies at $z > 10$. In fact, at $z = 12$, F125W samples across the Lyman limit. However, at $z = 9$ our data agrees with the predicted Schechter faint end slope, while the $z = 10$ prediction is about 1 dex below the extrapolated Schechter function. However, even at $z = 10$ this filter samples across the Lyman-α line and the flux has been attenuated by the intergalactic medium (IGM).

Examining the data for F160W, we see our simulated galaxies are somewhat bright at $z = 9$, but within $\approx 1\sigma$ of the model, while our $z = 12$ data are lower than predictions. This is also due to Lyman forest absorption in this bandpass. However, this level of agreement with Schechter functions based on Hubble deep-field surveys at $z = 9$ and 10 is evidence that our simulation is producing reasonable results out to these redshifts.

The situation is similar for the JWST bandpass filter at 1.5 μm (F150W). Our

data for galaxies at $z = 9$ and 10 follow the extrapolated Schechter function but once again, at $z = 12$, this wide-band filter samples mostly blue-ward of the Lyman-α line in the rest-frame. Hence we are seeing the attenuation of UV photons by the IGM as we go from $z = 10$ to 12.

The remaining plots for the JWST filters redder than 1.5 $\mu\,m$ match the predicted Schechter functions well for $z = 9$ and 10. The predictions for $z = 12$ are slightly lower than would be predicted by extrapolated Schechter functions, however we are in a cosmic era with unobserved and unmeasured galaxy counts as well as a region in which the simulation may be underestimating the numbers of these early structures due to limited resolution.

Considering our magnitude limit of $m_{\rm AB} = 31.4$ mag, galaxies at $z > 12$ have to be brighter than $M_{\rm AB} \approx -16.4$ to be detected by JWST. We note that none of our simulated galaxies at $z = 15$ are detectable given our assumption of a limiting magnitude $m_{\rm AB} = 31.4$ mag. Of course, our relatively small simulation volume did not generate any of the more rare, yet bright, galaxies at these high redshifts. However, filters 2 $\mu\,m$ and redder indicate detections for our galaxies out to $z = 12$ – if just barely.

3.4 Conclusions

We have used a large-scale cosmological simulation to study high-redshift galaxies and the prospect of finding Pop III-bright galaxies. While several of our contemporaries have done similar work (Cowley et al., 2018; Barrow et al., 2017; Liu et al., 2016; Xu et al., 2016; O'Shea et al., 2015), our approach is novel in that our models includes the enhancement to Pop III star formation we expect due to the timescale required to turbulently mix pollutants at subgrid scales. We find that our Pop III SFRD is approximately twice what we would have expected without modeling the

subgrid pristine fraction of gas. As a check, we have analyzed more than 20,000 galaxies in our simulation volume of 4828 comoving Mpc^3 producing UV LFs and statistics on the fraction of Pop III-bright galaxies across a range of redshifts. We have also generated LFs for several HST and JWST filters.

The current observational constraints on $z \geq 8$ LFs are uncertain at best (Finkelstein, 2016; McLeod et al., 2015; Bouwens et al., 2015; Oesch et al., 2015). Determining the faint end slope, α, is the challenge here since observations of galaxies dimmer than M^* are likely to dominate galaxy number densities at high-redshift and, more importantly, to be the home of Pop III galaxies. We find that linear extrapolations of the faint end slope to $z > 8$, as captured in Table 3.2, appear reasonable to $z = 16$. While the Schechter function indicates an ever-increasing number of faint galaxies, we know that the actual LF must flatten and turn-over at some point. Even though the simulation's resolution limits our ability to estimate this turn-over magnitude, we have determined that galaxies down to $M_{\mathrm{UV}} = -14$ reasonably follow the extrapolated α. Additionally, our simulation demonstrates that M^*_{UV}, the absolute magnitude where galaxy counts begin to rapidly decay, is brighter than $M_{\mathrm{UV}} = -17$ out to $z = 16$, again in agreement with linear extrapolations of current observations.

The mass-metallicity relation for our simulated galaxies follows the expected trend of increasing metallicity with increasing mass. When considering galaxies composed purely of Pop III stars, we note that they are very rare and typically have $M_{\mathrm{G}} < 10^9\, M_\odot$. The peak of Pop III galaxy formation occurs immediately before reionization at $z = 9$ and 10 where $\approx$17% and 25%, respectively, of simulated Pop III galaxies with $Z < Z_{\mathrm{crit}}$, have masses $M_{\mathrm{G}} > 10^9\, M_\odot$.

Turning to Pop III-bright galaxies with at least 75% of their flux coming from Pop III stars, roughly 17% of all galaxies brighter than $m_{\mathrm{UV}} = 31.4$ mag (*observable* galaxies) are Pop III-bright at $z = 9$, immediately before reionization. Less than

3% of observable galaxies are Pop III-bright between $7 \leq z \leq 8$, after reionization. Moving to $z = 10$, the Pop III-bright fraction falls to 5% – a smaller fraction of the set of more luminous observable galaxies. Finally, at $z > 10$, we do not find any galaxies that are Pop IIIbright with $m_{\rm UV} \leq 31.4$ mag within our volume. However, we find at least 18% of galaxies at $z = 12$ and 25% at $z = 14$ are Pop IIIbright when considering $m_{\rm UV} = 33$ mag, an intrinsic magnitude limit within reach of the JWST using lensing. Thus we predict that the best redshift to search for luminous Pop III-bright galaxies is just before reionization, while lensing surveys for fainter galaxies should push to the highest redshifts possible.

Although our simulation's enhanced Pop III SFRD has only minor implications for the LFs, it does play a significant role in the fraction of Pop III flux coming from our observable ($m_{\rm UV} \leq 31.4$ mag) high-redshift galaxies. In fact, when we consider the evolution of the subgrid pristine fraction, the fraction of observable Pop III-bright galaxies in the range $9 \leq z \leq 10$ is $\approx 2\times$ higher than in the classical Pop III case, in which Pop III stars are only generated in cells with gas $\overline{Z} < Z_{\rm crit}$. This emphasizes the importance of modeling Pop III star formation accurately, since it has a large effect on the types of galaxies we expect to detect at high redshift.

While our subgrid model greatly improves the code's ability to reliably produce results for a given physical model, we note that other simulations of high-redshift galaxies may make different assumptions about the relevant physics that lead to different conclusions about the observability of PopIII galaxies at $z > 10$ (e.g. Schaye et al. (2015); Jeon et al. (2014); Wise et al. (2012)). For example, a recent simulation by Jeon et al. (2015) followed the assembly of a single $10^8\,M_\odot$ halo in a zoom simulation with a high resolution 300 kpc^3 comoving box. They found that Pop III star formation was subdominant by $z \approx 13$ in this environment and negligible by $z = 10$. While some differences from our results are likely due to parameter choices and the

type of region being simulated, they also noted that radiative transfer and related heating played a crucial role in determining their results. While our work handles cooling by molecular hydrogen along with a simple model for H_2 photodissociation, we have not yet included radiative feedback, leaving this to future work. Thus the debate is ongoing as to the relative importance of different aspects of the physics as well as the values for loosely constrained parameters.

However, our data predict good news for the JWST. Although we have not considered the effects of attenuation due to dust absorption, our simulation exhibits galaxy counts per magnitude that meet or exceed current, observationally-based predictions for filters redder than $\approx 1.25\mu$m through $z = 10$.

While the simulation parameters used in this work are only a starting point for modeling the first galaxies, future work will address the sensitivity of these results across a range of values. These results will help guide future searches for Pop III galaxies.

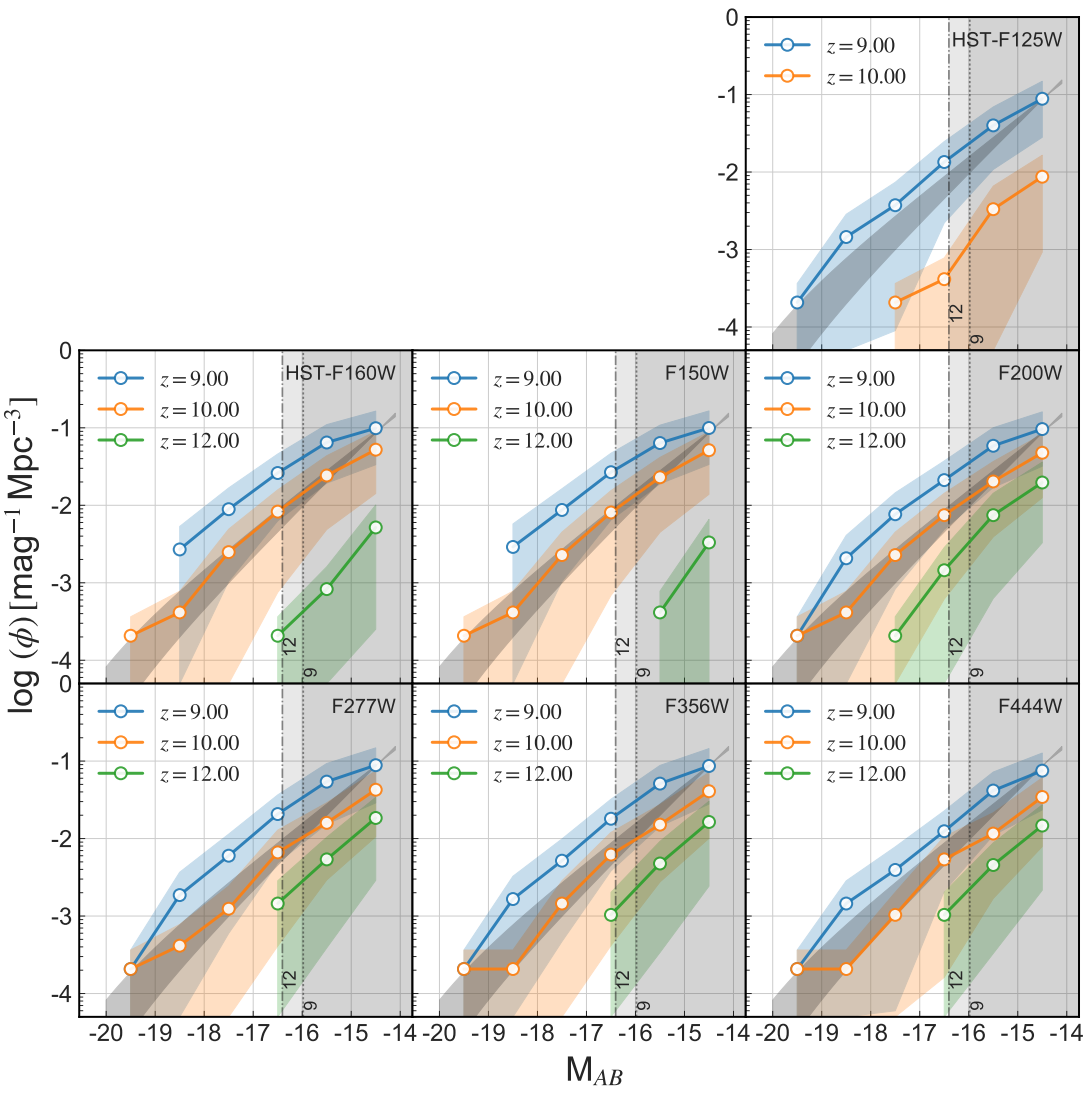

Figure 3.12: Luminosity functions, with 1σ error bounds, derived from our simulated galaxies convolved with our filter models across the redshift range $9 \leq z \leq 12$. The dark grey Schechter functions represent the bounding redshifts and are again from Finkelstein (2016) (without errors). The dark, vertical shaded areas of each plot indicate the regions where $m_{\rm AB} > 31.4$ mag, the JWST limiting magnitude for the ultra-deep campaign, for $z = 9$ and $z = 12$. If a redshift does not appear in a plot, none of our galaxies were visible in that filter. Note that we have not included dust attenuation.

Chapter 4

SIMULATION PARAMETER STUDY

4.1 Background

In the previous 2 chapters we discussed Pop III star formation in the context of cosmological simulations. In particular, we demonstrated that modeling the pristine fraction of gas at subgrid scales improves the accuracy of Pop III star formation in a manner similar to increasing the simulation's resolution. In turn, improving the accuracy of Pop III star formation improves our ability to predict the observability of high redshift galaxies and the rate at which Pop III SNe pollute the early universe. These results will help guide the search for Pop III stars and improve our understanding of the chemical enrichment of early galaxies.

While we have demonstrated that the timescale required to mix pollutants at subgrid scales is important, there are many other factors that go into understanding high redshift galaxy formation and many modeling parameters are poorly constrained. As such, in this chapter we explore some of the more loosely constrained parameters used in our cosmological simulations to determine their impact on the overall Pop III SFRD as well as the impact on the observability and chemical composition of early galaxies.

This chapter is structured as follows. In Section 2 we describe our methods, including a brief review of our implementation of the subgrid model of metal pollution, some of the relevant physics modeled within RAMSES, and the setup for the simulations used to characterize this parameter study. In Section 3 we describe our results and discuss the effects of the various parameters on the high-redshift luminosity function,

the fraction of Pop III flux emitted and the effect on the chemical composition of our stars. Finally, conclusions are discussed in Section 4.

4.2 Methods

We briefly review the simulation setup and physics used for all of the runs discussed in this chapter. The simulation physics, cosmology and the implementation of the pristine gas fraction scalar, as well as the primordial metallicity scalar, are the same as previously discussed in Section 3.2. Those interested only in a description of the parameters that differ from the simulations discussed in previous chapters should skip to Section 4.2.4.

4.2.1 Simulation Setup

To facilitate comparisons with our previous works in Chapters 2 and 3, we adopted the cosmological parameters used therein: $\Omega_{\rm M} = 0.267$, $\Omega_\Lambda = 0.733$, $\Omega_{\rm b} = 0.0449$, $h = 0.71$, $\sigma_8 = 0.801$, and $n = 0.96$, based on Komatsu et al. (2011). These parameters have their usual cosmological definitions.

We again made use of RAMSES (Teyssier, 2002), an adaptive mesh refinement (AMR) cosmological simulation code, to model a 12 Mpc h^{-1} on-a-side volume generated from Multi-Scale Initial Conditions (MUSIC) (Hahn & Abel, 2013). We evolved this volume to $z = 7$ covering approximately the first 780 Myr of cosmic history, given our cosmology, for each of the new simulations analyzed.

The following parameters are common to all of the simulations discussed in this work. The initial gas metallicity was $Z = 0$ and the primordial molecular hydrogen fraction was 10^{-6} (Reed et al., 2005). The initial grid resolution of 11.7 comoving kpc $\rm h^{-1}$ was based on a starting resolution of 1024^3 cells ($l_{\rm min} = 10$). Our choice for the initial resolution resulted in a DM particle mass of $4.47 \times 10^5\, M_\odot\, h^{-1}\, \Omega_{\rm DM}$ or

$1.40 \times 10^5\, M_\odot$ for our cosmology.

We took a quasi-Lagrangian approach to refinement. As cells became $8\times$ overdense, as compared to $\overline{\rho}$, we refined them to ensure the mean mass per cell was roughly constant across the simulation. We allowed for up to eight additional refinement levels ($l_{\rm max} = 18$) resulting in an average physical spatial resolution of 45.8 pc $\rm h^{-1}$. However the highest refinement level reached by $z = 7$ was $l = 15$.

The range of star particle (SP) masses generated across the simulations was $8.6 \times 10^3\, M_\odot \leq M_\star \leq 6.0 \times 10^4\, M_\odot$. The nonlinear length scale at the end of the simulations, $z = 7$, was 47 comoving kpc $\rm h^{-1}$. This scale corresponds to a mass of $3.2 \times 10^7 M_\odot$ $\rm h^{-1}$.

We did not model black holes (BHs), also known as sink particles, since BH feedback is not important for early galaxy evolution (Prieto et al., 2017; Jeon et al., 2012; Somerville et al., 2008; Scannapieco & Oh, 2004) or for the parameters we were interested in investigating.

The redshift of reionization was also a free parameter in our simulation. We set $z_{\rm reion} = 8.5$, as reported by the Planck Collaboration et al. (2016).

4.2.2 Simulation Physics

Ramses uses CLOUDY (Ferland et al., 1998) to model gas cooling for $T \gtrsim 10^4$ K. We used the cooling rates from Rosen & Bregman (1995) for temperatures below this value. We set the radiative cooling floor to 100 K, but adiabatic cooling can lower the gas temperature below this value. The UV background was derived from Haardt & Madau (1996).

As discussed in Chapter 2, we also modeled molecular cooling in the pristine gas (Johnson & Bromm, 2006; Prieto et al., 2008; Hirano & Yoshida, 2013). Our analytic model is based on work by Martin et al. (1996) and provides a radiative cooling rate,

Λ_r/n_{H_2}, for the gas densities encountered in the simulations. As mentioned above, we assumed a primordial H_2 fraction of 10^{-6}. We also assumed an optically thin box and all of our H_2 is destroyed shortly after the first stars are formed. We did not model H_2 formation.

The simulations spawn SPs in regions of gas according to a Schmidt law (Schmidt 1959) using a star formation rate

$$\frac{d\rho_\star}{dt} = \epsilon_\star \frac{\rho}{t_{\rm ff}}, \text{ when } \rho > \rho_{\rm th}. \tag{4.1}$$

where $t_{\rm ff} = \sqrt{3\pi/(32G\rho)}$ is the gas free fall time. Star forming regions also needed to be at least 200 times the mean density of the simulation, as a function of redshift, before SPs were formed. This ensured that SPs are only formed in collapsed objects and not in high-density flows (Rasera & Teyssier, 2006; Dubois & Teyssier, 2008).

For our simulations we set $\rho_{\rm th} = 1.0\, m_p\, {\rm cm}^{-3}$. We set the star forming efficiency to $\epsilon_\star = 0.01$, giving results in reasonable agreement with the observed high redshift star formation rate (Finkelstein, 2016; Madau & Dickinson, 2014). Our SP mass resolution was $m_\star = \rho_{\rm th}\Delta x^3 = 6.6 \times 10^3\, M_\odot$. The final mass of each SP was drawn from a Poisson process such that it was a multiple of $m_\star$.

Lastly, while radiation pressure from Pop III and other massive stars can disrupt – and also trigger – star formation (Wise et al., 2012; Tremblin et al., 2012; Deharveng et al., 2010; Whalen et al., 2004), effecting the star formation rate in early galaxies, we did not included its effects in this work. This is an important aspect of the physics that we will explore in a subsequent study.

4.2.3 The Pristine Fraction, Primordial Metallicity and the Corrected Metallicity

For these simulations, we made use of the modifications to RAMSES described in Section 2.2.1 to track two new metallicity-related scalars. These scalars allowed us

to more accurately model the fraction of Pop III stars created in early galaxies and to follow the unique elemental yields generated by Pop III SN. The *pristine gas mass fraction*, P, and the *primordial metallicity*, $Z_{\rm P}$, are described below. Additionally, we discuss how we used the pristine fraction to improve the accuracy of the metallicity of the gas and SPs.

The Pristine Fraction

The pristine gas (mass) fraction, P, was used to track the mass fraction of gas with $Z < Z_{\rm crit}$ in each simulation cell. The scalar evolves from $P = 1$, indicating that 100% of the gas in the cell is metal-free, to $P = 0$, indicating that all of the gas in the cell has been polluted above $Z_{\rm crit}$. $P_\star$ records the value of P in SPs at the time they were spawned and identifies the mass fraction of Pop III stars with $Z_\star < Z_{\rm crit}$ for each SP.

As discussed in detail in Pan et al. (2013), and first implemented in a cosmological simulation in Sarmento et al. (2017), the following equation was used to describe the evolution of the pristine gas fraction:

$$\frac{dP}{dt} = -\frac{n}{\tau_{\rm con}} P \left(1 - P^{1/n}\right). \tag{4.2}$$

The change in the pristine gas fraction at each time-step was therefore a function of n, a measure of the locality of mixing, and a timescale $\tau_{\rm con}$, that is the inverse of the turbulent stretching rate (Pan & Scannapieco, 2010; Pan et al., 2012, 2013; Sarmento et al., 2017). These parameters are, in turn, functions of the turbulent Mach number, M, and the average metallicity of the cell relative to the critical metallicity, $\overline{Z}/Z_{\rm crit}$. By knowing P at the time of star formation we subsequently modeled the mass fraction of Pop III stars for each SP formed as $M_{\star,\rm III} = M_\star \times P_\star$.

The Corrected Metallicity

Each SP in the simulation recorded both the host cell's average metallicity, $\overline{Z} \rightarrow \overline{Z}_\star$, and the pristine gas fraction, $P \rightarrow P_\star$ at the time it was created. This information was combined to better model the metallicity of the polluted fraction of gas or stars. When metals were well mixed throughout the cell's volume $P = 0$ and the scalar $\overline{Z}$ represented the average metallicity of any sub-volume of gas in the cell. However, before mixing was completed, the polluted fraction, $f_{\rm pol} \equiv 1 - P$, described the fraction of gas that was actually polluted with metals. Therefore, a better estimate of the metallicity of the polluted fraction of gas was the corrected metallicity

$$Z = \frac{\overline{Z}}{f_{\rm pol}}. \tag{4.3}$$

As expected, when $f_{\rm pol} = 1$ the corrected metallicity was the average metallicity. However, when $f_{\rm pol} < 1$ only a fraction of the cell was polluted and the metals were concentrated in a volume smaller than the cell. When referring to the corrected metallicity of polluted fraction of gas or SPs, we use Z or $Z_\star$.

As discussed in 2, the corrected metallicity was precise when all of the metals are contained in the polluted fraction. However, the gas could be polluted to $\overline{Z} < Z_{\rm crit}$ in regions still capable of creating Pop III stars. This situation resulted in a small uncertainty in the corrected metallicity that we ignore. Equation (4.3) captures the upper bound to the correction while the lower bound to the corrected metallicity is

$$Z = \frac{\overline{Z} - Z_{\mathbb{P}} P}{f_{\rm pol}}, \tag{4.4}$$

where $Z_{\mathbb{P}} = Z_{\rm crit} = \{10^{-6}, 10^{-5}, 10^{-4}\} Z_\odot$ (for runs Z6, fid and Z4, respectively) was the upper limit on the metallicity of the pristine gas. Note that when $Z_{\mathbb{P}} = 0$, as it would when polluting the primordial gas, equation (4.3) is exactly the metallicity of the polluted fraction of gas, assuming that pollutants were well mixed in this sub-volume.

Finally, we did not create polluted stars when the polluted fraction of gas in a cell, $1 - P$, was $< \{10^{-6}, 10^{-5}, 10^{-4}\}$ for runs Z6, fid, and Z4, respectively. While this may seem arbitrary, creating such a small fraction of Pop II stars would not change our results.

Primordial Metals

We refer to the first metals generated by the first stars as *primordial metals*. Since the elemental abundance patterns for ejecta from massive Pop III SN are likely very different from that of lower-mass Pop II stars (Heger & Woosley, 2002), we have developed a straightforward method to track these metals in a cosmological simulation. Anytime a SP with a non-zero pristine fraction went SN, we tracked the Pop III SN ejecta using the scalar $\overline{Z}_{\rm P}$.

This new scalar allowed us to follow primordial metals injected into the gas and to model the final metal content of subsequently formed SPs via $\overline{Z}_{\star}$ and $\overline{Z}_{{\rm P},\star}$. Every SP potentially possessed a combination of these two types of metals. Once we applied our correction to the metallicity, the fraction of primordial metals in SPs was computed as $Z_{{\rm P},\star}/Z_{\star}$ where $Z_{\star}$ captures the total metallicity of the SP. When mapping these metallicities to the chemical composition of a SP (or fraction thereof for $0 < P < 1$), we used $Z_{\star} - Z_{{\rm P},\star}$ to model the mass fraction of 'normal' metals, while $Z_{{\rm P},\star}$ modeled the mass fraction of primordial metals produced by a representative Pop III SN abundance pattern.

4.2.4 Simulations

We carried out a set of 5 large-scale cosmological simulations to study the effects of varying the critical metallicity, SN mass loading, and the consequences related to adopting a Pop III specific IMF on the overall cosmic star formation rate and the rate

and location of Pop III star formation. Table 4.1 identifies the simulations and their corresponding parameters. All other simulation parameters were consistent across all runs, as described in Section 4.2.1.

Table 4.1: Simulations

Name	$Z_{\rm crit}$	f_w[a]	Pop III IMF	α	$M_{\rm c}/M_\odot$	σ
fid	10^{-5}	10	Salpeter[b]	2.35	–	–
Z4	10^{-4}	10	Salpeter	2.35	–	–
Z6	10^{-6}	10	Salpeter	2.35	–	–
P3SN	10^{-5}	10	Log normal[c]	–	60	1.0
fw1	10^{-5}	1	Salpeter	2.35	–	–

[a] This is SN mass loading. It denotes the amount of gas, expressed in multiples of the mass of SN ejecta, carried along with the SN blast and removed from the host cell.
[b] The Salpeter IMF mass range spans 0.1 to 100 $M_\odot$.
[c] The log normal IMF mass range spans 1 to 500 $M_\odot$.

The critical metallicity, $Z_{\rm crit}$, marks the boundary between Pop III and Pop II star formation. This parameter is loosely constrained (Omukai et al., 2005) and we explored the effects of varying the critical metallicity across 3 orders of magnitude on the Pop III star formation rate and on the subsequent luminosity and chemical composition of early galaxies. We defined the critical metallicity of the gas for the fiducial run as $Z_{\rm crit} = 10^{-5} Z_\odot$, as was done in our earlier works. The runs Z4 and Z6 were used to determine the effects of setting the critical metallicity 1 dex higher, and lower, respectively.

By default, the RAMSES model for stellar evolution assumes that a user-specified fraction, $\eta_{\rm SN}$, of the mass of each SP, regardless of the SP's metallicity or pristine fraction, goes SN after 10 Myr. We used $\eta_{\rm SN} = 0.10$ for the fiducial run corresponding to the massive, short lived stars at the top of a Salpeter (1955) IMF. For this study,

we implemented a second IMF for Pop III stars.

The fraction of each SP, in run P3SN, with metallicity below $Z_{\rm crit}$ is $P_\star \times M_\star$ and was modeled using a log normal Pop III IMF (Larson, 1973) as discussed in Raiter et al. (2010) and Tumlinson (2006). Our Pop III IMF had a characteristic mass of 60 $M_\odot$ and $\sigma = 1$. The mass range spans 1 to 500 $M_\odot$ and corresponds to Model ID "TE" in Raiter et al. (2010). Specifically, our IMF was

$$\frac{dN}{d\ln(M)} = exp\big(-5.3 - \frac{1}{2\sigma^2}\ln(\frac{M}{60M_\odot})^2\big) \tag{4.5}$$

where -5.3 normalizes the PDF.

The IMF directly influenced the luminosity of galaxies containing Pop III stars as well as the fraction of Pop III SN. Our Pop III IMF resulted in 99% ($\eta_{\rm SN,III} = 0.99$) of Pop III stars going SN within the first 10 Myr representing a significant increase in feedback energy as well as the amount of metals injected into the ISM as compared to the fiducial case. Note that we used the same Type II SN prescription for all Pop III SN in this IMF although a subset of stars in the mass range ≈40-140 $M_\odot$ may collapse directly into BHs or generate pair-instability SN (PISN) (Heger et al., 2003) with different explosion energies and yields.

The fraction of Pop II stars, per SP, had mass $(1.0 - P_\star) \times M_\star$. This IMF was modeled using the Salpeter IMF described above with $\eta_{\rm SN} = 0.10$. The Pop II IMF used the standard power-law slope, $\alpha = 2.35$, and spanned the mass range 0.1 to 100 $M_\odot$. Once again, the mass range and slope did not directly factor into the SN feedback process since a fixed 10% of the mass fraction of each polluted SP resulted in a SN after 10 Myr – regardless of the maximum mass assumed. However, these parameters were important when modeling the luminosity of the surviving SPs.

All SN in the simulation injected $E_{\rm SN} = 10^{51}$ ergs/10 $M_\odot$ even though the energy from some Pop III stars were likely to have been higher (Scannapieco et al., 2003;

Scannapieco, 2005; Heger & Woosley, 2010). Further, we assumed that 15% of SN ejecta were metals, regardless of the type of SP.

The mass-loading parameter, f_w, established the amount of gas, in terms of a multiple of the mass of SN ejecta, in the host cell that was carried along with the SN blast. For this work, and our previous studies, we used a default value of $f_w = 10$. This material was subsequently distributed equally among all of the cells within the SN blast radius of 300 pc, or a volume of $\approx 1.13 \times 10^8$ pc^3. For this study, we explored the effect of reducing the mass loading factor to $f_w = 1$ via run fw1.

While the fractional difference in the amount of material carried into the cells in the SN blast radius was insignificant, reducing f_w from 10 to 1 resulted in early galaxies retaining more of their gas. Specifically, for the $f_w = 10$ fiducial case, each SN removed 1 SP mass of gas from the cell since the SN ejecta mass was 10% of the SP mass. This level of SN mass loading helped to modulate future star formation by reducing the gas in star forming cells, although, for numerical reasons, the maximum amount of gas carried by any SN was capped at 25% of the gas remaining in the cell. For $f_w = 1$, 10x more gas was left in the central star forming region of active galaxies as compared to the fiducial case, assuming the 25% limitation was not routinely reached in that simulation.

4.2.5 Halo Finding

AdaptaHOP (Aubert et al., 2004) was used to find star forming galaxies in the simulation. Groups of 20 particles were used to compute the local matter density and halos must have been composed of at least 100 DM particles, equivalent to a DM halo mass of $1.4 \times 10^7\, M_\odot$, to have been considered a candidate halo. Further, only candidates with densities 80 times the average total matter density, as a function of redshift, were saved.

Many of the more massive objects found by AdaptaHOP were composed of more than one observationally distinguishable galaxy and these overly bright objects had the potential to bias the bright end of our luminosity functions. To determine the observable radius of galaxies, we assumed that detectability implied at least a 0.1 arcsec separation between objects, as is does for the HST. We postprocessed these halos, as discussed in 3, to ensure we identified individual galaxies.

4.2.6 Galaxy Spectral Models and Simulated Observations

We computed the UV fluxes, at a rest-frame wavelength of 1500 $\mathring{A}$, for our simulated galaxies based on the redshift, ages, metallicities, and masses of their constituent SPs using a set of simple stellar population spectral energy density (SED) models. We used the same procedure as described in Section 3.2.5. Further details are contained therein.

Each of the model SEDs was redshifted over the range z=7-16 and attenuated to account for Lyman forest and continuum absorption (Madau, 1995). This process also included a spectral conversion from wavelength to frequency converting the SEDs into the familiar units of flux, normalized to an IMF of stars with 1 solar mass: $erg/s/Hz/cm^2/M_\odot$.

All of the SEDs, translated into fluxes at a given redshift, modeled stars of discrete metallicities and discrete ages spanning the age range of SPs in the simulation. We interpolated the data in both metallicity and age linearly, in log-space, to determine the flux of specific SPs and fractions thereof.

The flux from Pop II stars, with $Z_\star \geq Z_{\rm crit}$, were based on *STARBURST 99* SEDs (Leitherer et al., 2014), supplemented with SEDs by Raiter et al. (2010), for $Z_{\rm crit} \leq Z_\star \leq 5 \times 10^{-4}\, Z_\star$. These SEDs modeled a Salpeter IMF, see Table 4.1, were normalized to $1 M_\odot$ and the fluxes derived from them were easily scaled by the

polluted mass fraction of each SP.

Pop III stars, with $Z_\star < Z_{\rm crit}$, had fluxes that were based on Raiter et al. (2010) SEDs that were derived from the log normal IMF (see Table 4.1 and Figure 3.5), normalized to $1 M_\odot$, for $Z = 0$ stars. As mentioned, the Pop III stellar mass, as a fraction of each SP, was $P_\star \times M_\star$.

4.3 Results

We analyze our simulations with a focus on Pop III stars in both aggregate and within the context of galaxies, focusing on $7 \leq z \leq 15$. Figure 4.1 depicts the star formation rates density (SFRD) for our simulations, along with observational data derived from Madau & Dickinson (2014) and Finkelstein (2016). We have tuned our star forming efficiency such that our SFRDs are in fair agreement with the LF-based SFRD described by Finkelstein (2016) over the range $7 \leq z \leq 8$ when considering both Poisson error and sample variance (Trenti & Stiavelli, 2008). We use the same star forming efficiency for all runs. We include the 1σ errors only for the fiducial and P3SN runs since they show the greatest variance. For a detailed discussion on error analysis see Section 3.3.2.

Figure 4.1 also depicts the Pop III SFRD as well as the classical Pop III SRFD that does not include the effects of modeling the evolution of the pristine gas fraction and its subsequent effect on Pop III star formation. Almost immediately, after polluted stars begin to form at $z \lesssim 18$, we notice that the difference between the three runs with different critical metallicities, $Z_{\rm crit}/Z_\odot = 10^{-4}, 10^{-5}$, and 10^{-6}, do not show much variation. This result demonstrates that the Pop III cosmic star formation rate is very weakly correlated with the value of the critical metallicity over this redshift range.

However, the variation due to modeling the evolution of the pristine gas fraction,

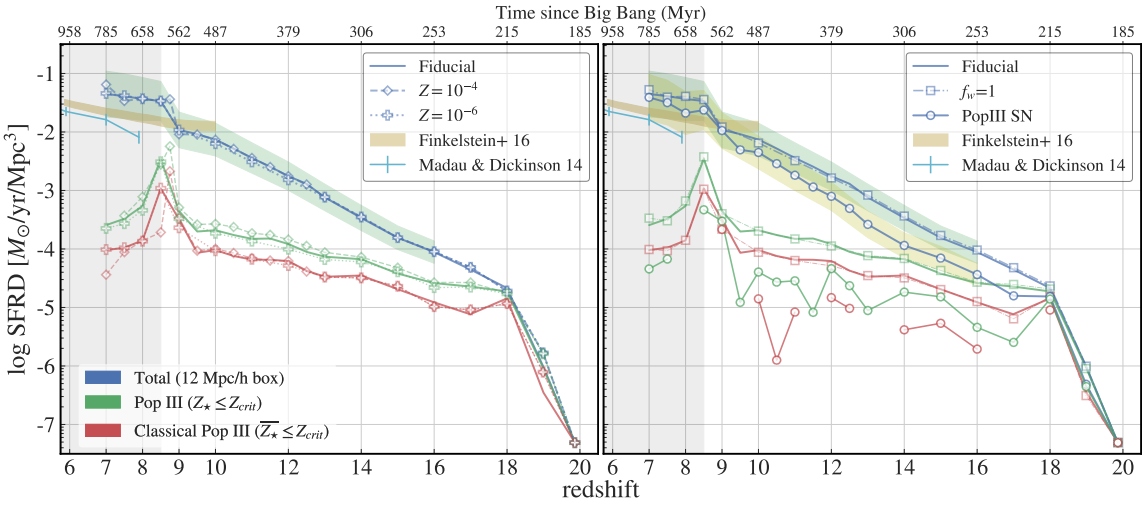

Figure 4.1: SFRDs along with observations by Madau & Dickinson (2014) and a LF-based SFRD by Finkelstein (2016). The LF-based SFRD is based on an integration of the reference luminosity function to $M_{\rm UV}$ = -13 mag. The 1σ uncertainty on our data, $z \leq 16$, accounts for both Poisson noise and sample variance. The Pop III SFRD show very little variation over 3 orders-of-magnitude of the critical metallicity demonstrating that modeling the gas at sufficient resolution, or via a subgrid model, is more important that knowing $Z_{\rm crit}$. The largest effect on the star formation rate occurs when changing the IMF for Pop III stars. The grey-shaded area indicates redshifts post-reionization. If data is missing for a redshift it indicates a SFRD of zero.

P, accounts for an average increase of a factor of ≈2 (0.3 dex) in the Pop III SFRD, at $z < 18$, as compared to the classical rate, when averaged across all 5 runs. An increase in the Pop III rate for the subgrid model was also evident in our earlier work (see Chapter 2) and confirms that modeling the unpolluted fraction of gas, or increasing the resolution of the simulation, is more important than knowing the critical metallicity when attempting to predict the Pop III star formation rate at high redshift.

The greatest change in the Pop III star formation rate is caused by the change to the Pop III IMF in run P3SN. This is not surprising since the log normal IMF adopted for Pop III stars in P3SN results in almost 10x more energy and pollutants than the Pop III stars modeled via a Salpeter IMF in all other runs. The difference

between the Pop III SFRD for P3SN and the fiducial run is approximately a factor of 4.3 over the range $z < 18$. Thus, the P3SN simulation demonstrates how feedback and the IMF are intimately linked making high redshift predictions of Pop III stellar populations difficult without further observational data or theoretical insight (Stacy et al., 2010; Bromm et al., 1999).

Considering the P3SN run, we also note that the classical Pop III rate falls to zero during several cosmic epochs: $z = 18 \rightarrow 16$, $14 \rightarrow 12.5$, $12 \rightarrow 11$, and $10 \rightarrow 9$. This is due to the increased metal generation coupled with the instantaneous mixing assumption that is typically used in simulation cells polluted with SN ejecta. Our subgrid model exhibits continued Pop III star formation in regions of unpolluted gas during these intervals.

As pointed out in Chapter 3, the increase in star formation immediately before reionization, $z_{reion} \approx 8.5$, correlates strongly with a sharp increase in the Pop III star formation rate. This is caused by a significant number of new minihalos crossing the star formation density threshold immediately before reionization increases the temperature of the gas (Furlanetto & Oh, 2008). Hence we predict that the largest number of Pop III dominated galaxies will be found just prior to reionization.

Figure 4.2, left, supports this conclusion and depicts the fraction of halos that have at least 90% of their stellar mass in Pop III stars – henceforth 'Pop III dominated' galaxies – as a function of redshift. The increase in the number of new Pop III dominated galaxies is clearly visible at $z = 9$. The right panel depicts the mass of Pop III dominated halos, for the fiducial run, and clearly shows that Pop III dominated halos also attain their highest masses during this epoch. Even though polluted star formation is keeping pace with Pop III star formation at $z = 9$, the majority of Pop III star formation is taking place in new minihalos as we demonstrate next.

Figure 4.3 depicts the metallicity of the gas for run fw1 at two redshifts, before

and after reionization, and a subset of galaxy locations where $m_{\rm AB} \leq 33$ mag. As can be seen, most of the Pop III dominated galaxies at $z = 9$ form in unpolluted regions away from existing galaxies. At $z = 8$ Pop III star formation has dropped-off significantly since reionization has raised the halo mass required to initiate star formation (Couchman & Rees, 1986; Simpson et al., 2013; Bose et al., 2018). Pop III dominated galaxies drop off by a factor of 10 post-reionization.

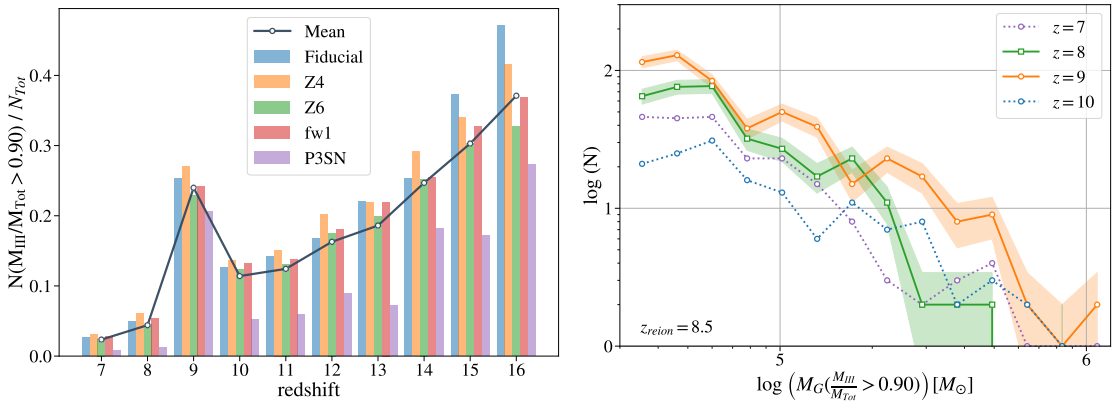

Figure 4.2: *Left:* The fraction of halos dominated by Pop III star formation (defined as galaxies with at least 90% of their stellar mass in Pop III stars) across all runs sharply increases immediately before reionization at $z = 9$. Considering all of the runs except P3SN, fully 25% of galaxies, pre-reionization, are Pop III dominated while only 5% are post-reionization. *Right:* The histogram depicts counts of Pop III dominated galaxies, binned in mass, and indicates that they also attain their peak masses, for the fid run, at $z = 9$ (orange) vs post-reionization (green). The shaded regions around the solid lines indicate 1σ errors based on the galaxy counts.

Referring back to Figure 4.2, and ignoring P3SN for now, at $z = 9$, ≈25% of galaxies are Pop III dominated. However, by $z = 8$ the majority of star formation is taking place in pre-existing polluted galaxies and the fraction of Pop III dominated galaxies drops to ≈5%. While P3SN generates the lowest fraction of Pop III stars and halos, the difference between the number of halos pre and post-reionization is just as dramatic. At $z = 9 \approx 21\%$ of galaxies are Pop III dominated. This falls to slightly more than 1% by $z = 8$, also a 20% drop as exemplified by the other runs.

Lastly, while the overall fraction of Pop III dominated galaxies is greater at $z > 13$

than at $z = 9$, as we discuss in the next section, the fraction of potentially observable galaxies falls off quickly at $z > 10$ for all of our models.

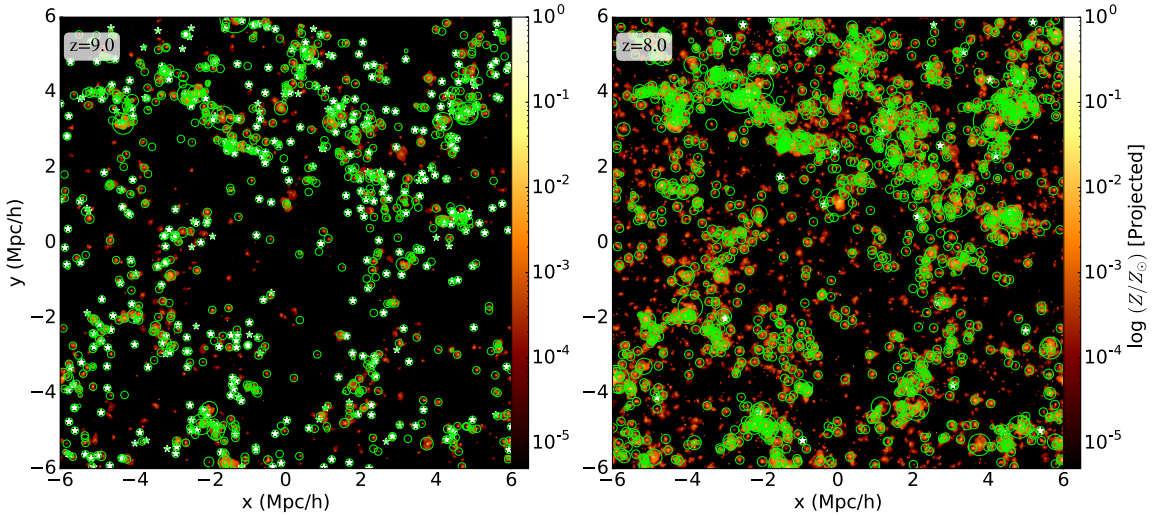

Figure 4.3: The metallicity of the gas for run fw1 at $z = 9$ (left) and 8 (right). Circles and stars indicate galaxies with $m_{\rm AB} \leq 33$ mag. Symbol size indicates the relative mass of each galaxy. White stars identify Pop III dominated galaxies (with $\geq 90\%$ of mass in Pop III stars). Green circles are galaxies with $< 90\%$ of their mass in Pop III stars. At $z = 9$, there are 399 Pop III dominated galaxies and most form in pristine gas away from existing galaxies. By $z = 8$, Pop III star formation is quenched since reionization raises the overall gas temperature raising the halo mass required to initiate star formation. Here there are only 39 Pop III dominated galaxies. Scale is comoving Mpc $\rm h^{-1}$.

4.3.1 Galaxy Luminosity Comparison

Next, we evaluate the effect of our parameters on galaxy flux, remembering that a relatively small changes in the fraction of Pop III stars with ages < 3.5 Myr can make a significant change to a galaxy's luminosity. Figure 4.4 depicts LFs for our simulations across the redshift range $7 \leq z \leq 15$. The shaded areas indicate the two intrinsic magnitude limits we believe JWST will be able to detect in the deep campaign, $m_{\rm UV} = 31.4$ mag, and via lensing, $m_{\rm UV} = 33$ mag, respectively (Gardner et al., 2006).

All of the runs produce essentially indistinguishable LFs when considering 1σ

estimated errors based on Poisson noise and sample variance. Even the run P3SN, that generates $\approx 10\times$ the SN feedback as compared to the other runs, displays only a small change in galaxy luminosities across the redshift and magnitude range depicted. The combination of feedback and the reduced number of surviving Pop III stars, at each redshift, does slightly reduce the brightness of galaxies toward the faint end for run P3SN. It is in this region that we see the effect of the additional Pop III SN energy as fewer minihalos are Pop III dominated. Smaller galaxies with fewer Pop III stars are also less luminous.

The consistency of these result across simulations indicates that our predictions for the luminosity of high redshift galaxies in Chapter 3 are robust across this parameter space. While we have yet to look at the effects of radiation pressure on star formation, it is promising to note that the luminosity of these galaxies does not seem to be highly correlated with the critical metallicity or SN loading.

4.3.2 Pop III flux

While our parameter variations do not result in striking changes to the LFs of our high redshift galaxies, they do produce changes to the fraction of Pop III flux coming from them. In Chapter 3 we focused on the fraction of galaxies with at least 75% of their flux coming from Pop III stars. Here we briefly discuss the changes to the Pop III flux fraction down to 10^{-3} but once again focus on 'observable Pop III-bright' that have $m_{\rm UV} \leq 31.4$ mag and $f_{\rm III}/f_{\rm Tot} \geq 0.75$. These galaxies are important to future observational searches for Pop III stars.

While each of our runs produce changes to the Pop III flux fractions of our galaxies, the most drastic change is between the fiducial and the P3SN run. Figure 4.5 depicts the UV Pop III flux fraction, $f_{\rm III}/f_{\rm Tot}$, as a function of the magnitude and redshift of our galaxies, measured at $1500\mathring{A}$ in the rest-frame, for these two runs. Note that we

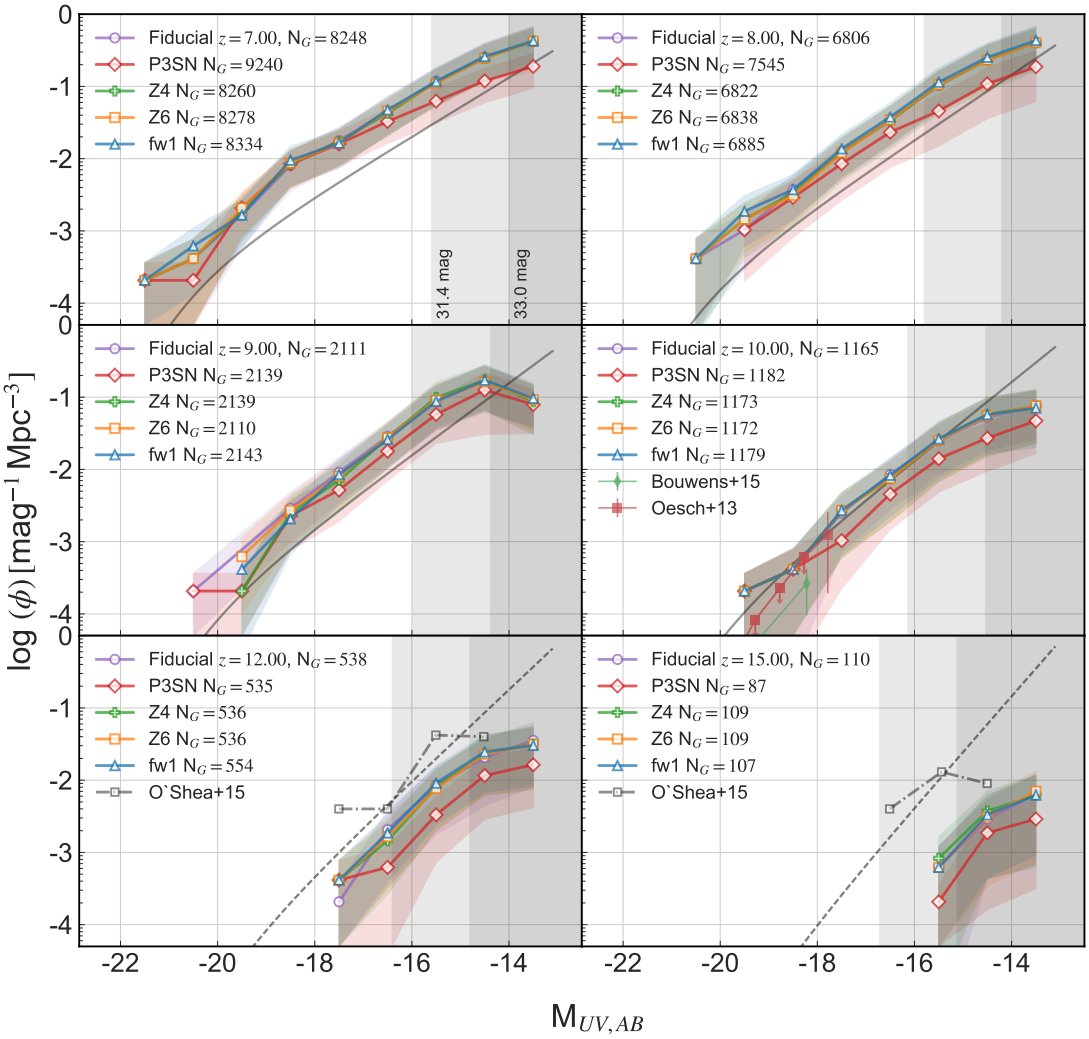

Figure 4.4: UV LFs derived from our simulations with 1σ error bounds including both Poisson noise and sample variance. Solid (dashed) grey lines are Finkelstein (2016) (extrapolated) Schechter fits. For $z = 10$, we have included Bouwens et al. (2015) and Oesch et al. (2013) observational data, with error bars. Redshifts 12 and 15 include luminosity functions derived by O'Shea et al. (2015) from the Renaissance Simulations. The rectangular shaded areas indicate likely limiting intrinsic magnitudes for JWST ultra-deep and lensed observations. As depicted, varying the critical metallicity and SN mass loading does not appreciably effect the flux coming from our simulated galaxies. However, adopting a Pop III log normal IMF, run P3SN, greatly reduces the number of Pop III stars in minihalos. We see the effect on the luminosity of small galaxies at the faint end of the LF. However all runs produce LFs that are still within the 1σ of each other.

have normalized the probabilities in each magnitude bin such that they sum to one.

We focus on a representative sample from $z = 7 - 15$ as was done previously.

As can be seen, P3SN results in a reduction in the counts of galaxies brighter than $M_{\rm UV} = -14$ across the range $10^{-3} < f_{\rm III}/f_{\rm Tot} < 0.75$ as compared to the fiducial run. Galaxies in this flux fraction range are hybrids composed of both Pop III and Pop II stars, although galaxies with $f_{\rm III}/f_{\rm Tot} \geq 0.75$ can also contain a small fraction of Pop II stars.

This reduction in the number density of hybrid galaxies is caused by the 10 fold increase in SN energy in run P3SN that efficiently evacuates the gas from the host halo. Considering the typical (also the minimum) SP mass $M_\star \gtrsim 8.3 \times 10^3\, M_\odot$ we find the SN energy generated by Pop III SNe are at least 8.2×10^{53} erg, since $E_{\rm SN} = 10^{51}\,(\frac{M_{\rm SP}}{10 M_\odot})$ erg. Figure 4.6, top, depicts the range of halo DM masses in this simulation along with a plot of the estimated gravitational binding energy (Loeb, 2010),

$$E_{\rm b} = 2.9 \times 10^{53} \left(\frac{M_{\rm h}}{10^8 M_\odot}\right)^{5/3} \left(\frac{1+z}{10}\right) \text{ erg}, \tag{4.6}$$

bottom, for these halos. When considering a SN to gas coupling efficiency of 10% (Hartwig et al., 2018; Kitayama & Yoshida, 2005; Whalen et al., 2008), we note that our Pop III SNe efficiently evacuate the gas from median mass halos and below, which have binding energies $\lesssim 4.3 \times 10^{52}$ erg.

Also, the mean binding energy is only a factor of 1.6 above the 10% SN coupling energy for a minimum mass SP. A coupling fraction of 16%, or 2 Pop III SNe, is/are enough to unbind the gas from average mass galaxies. Hence, galaxies with a mass of $\leq 5.3 \times 10^7\, M_\odot$ at $z = 7$ and $\leq 3.5 \times 10^7\, M_\odot$ at $z = 15$, cannot retain their baryons when one or more Pop III SN occur. In fact, an average of 67%, by number, of halos become unbound by Pop III SN in the P3SN run. By mass, the fraction of halos unbound by SN goes from 32% at $z = 15$ down to 23% at $z = 7$. This increased feedback explains the lack of hybrid galaxies in the P3SN simulation.

While our stellar feedback and SN physics is not as complete as described in the

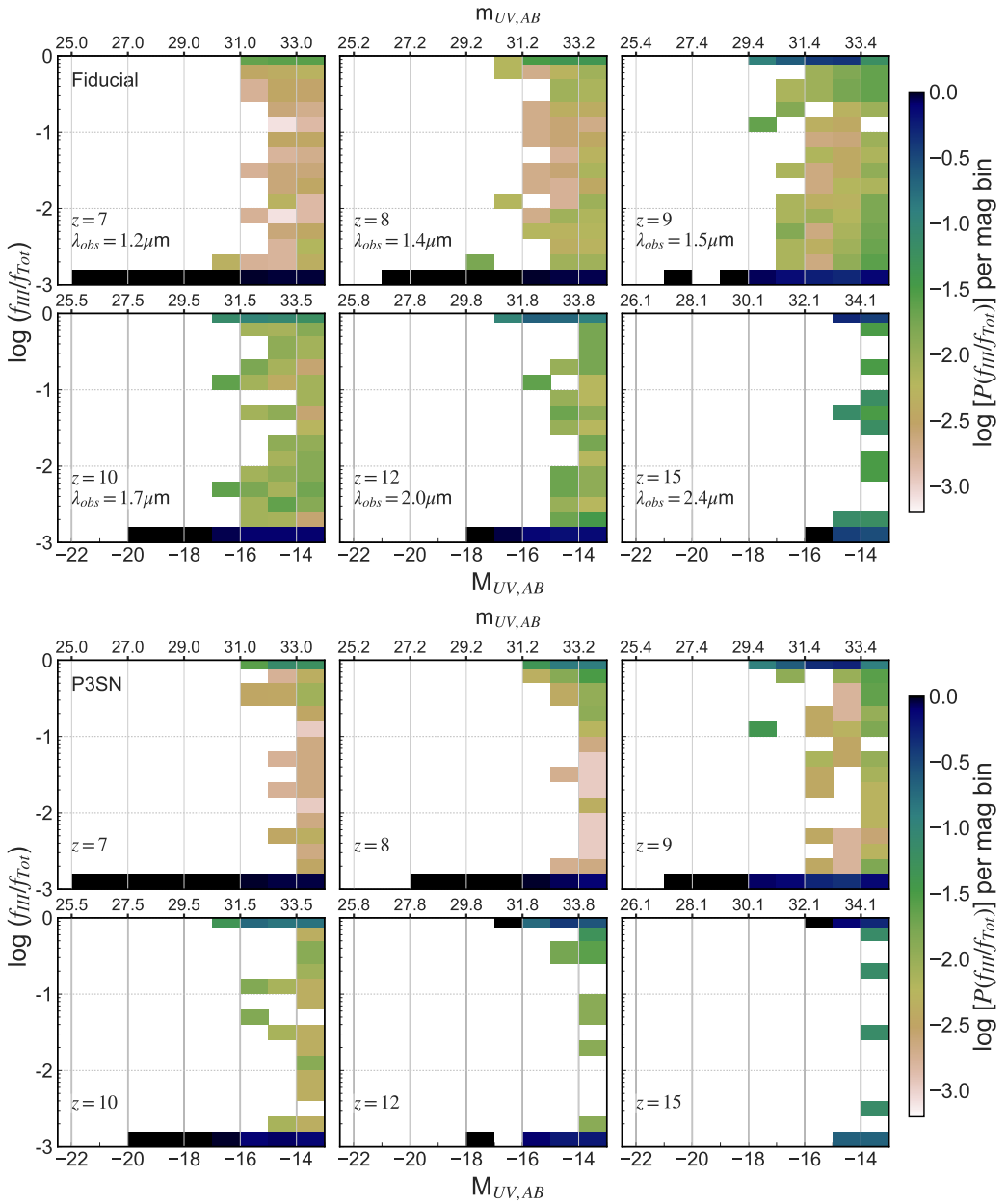

Figure 4.5: The normalized probability of finding a UV Pop III flux fraction, $f_{\rm III}/f_{\rm Tot}$, as a function of the redshift and magnitude of our galaxies for the fiducial and P3SN runs. The top row of bins in each plot represent a Pop III flux fraction of at least 75%. Comparing P3SN to the fiducial run, the probabilities of finding galaxies with $10^{-3} \leq f_{\rm III}/f_{\rm Tot} < 0.75$ decreases at all redshifts for the former simulation. This is due to the increased feedback in the P3SN simulation. However, the fraction of observable Pop III-bright (top row of bins) keeps pace at all redshifts indicating Pop III star formation in minihalos is the dominate source of Pop III flux.

above references, our purely mechanical SN feedback acts on SN ejecta mass on the order of the SP mass for our P3SN simulation. This level of coupling effectively removes the majority of gas from SN-hosting cells quenching further star formation.

Returning to Figure 4.5, the fraction of observable Pop III-bright galaxies (top row of bins in each plot) remain fairly consistent across both simulations. This is due to the fact, as already discussed, that most Pop III star formation occurs in new minihalos, away from polluted galaxies. Such star formation is relatively unaffected by the IMF and SN rate.

At $z = 12$ we see a higher fraction of observable Pop III-bright galaxies at $m_{\rm UV} \approx 31.8$ mag for the P3SN simulation than for the fiducial run while the fraction of highly polluted halos at $f_{\rm III}/f_{\rm Tot} \leq 10^{-3}$ is zero. This is once again due to the increased SN feedback that tends to quench star formation in existing halos while similar mass halos in the fiducial run continue to form Pop II stars. Hence the P3SN simulation shows fewer galaxies with a mix of Pop III and Pop II stars as compared to the fiducial model.

Pop III-bright galaxies, as a fraction of all observable galaxies, are summarized in Figure 4.7. Each panel compares a different run to the fiducial simulation. We depict the JWST 'observable' limiting magnitude of $m_{\rm UV} = 31.4$ mag, along with a lensing magnitude limit of $m_{\rm UV} = 33$ mag. We also include the classical Pop III star forming case. Error bars are based on Poisson noise only and are included for the non-fiducial runs.

Varying the critical metallicity does not appreciably change the fraction of observable Pop III-bright galaxies in our sample volume at $z = 9$, and counts at $z < 9$ are consistent with zero or a very small fraction of observable Pop III-bright galaxies. However, we note that the fiducial run did not generate any observable Pop III-bright galaxies at $z = 12$ as did the Z4 and Z6 runs. This may seem puzzling until we re-

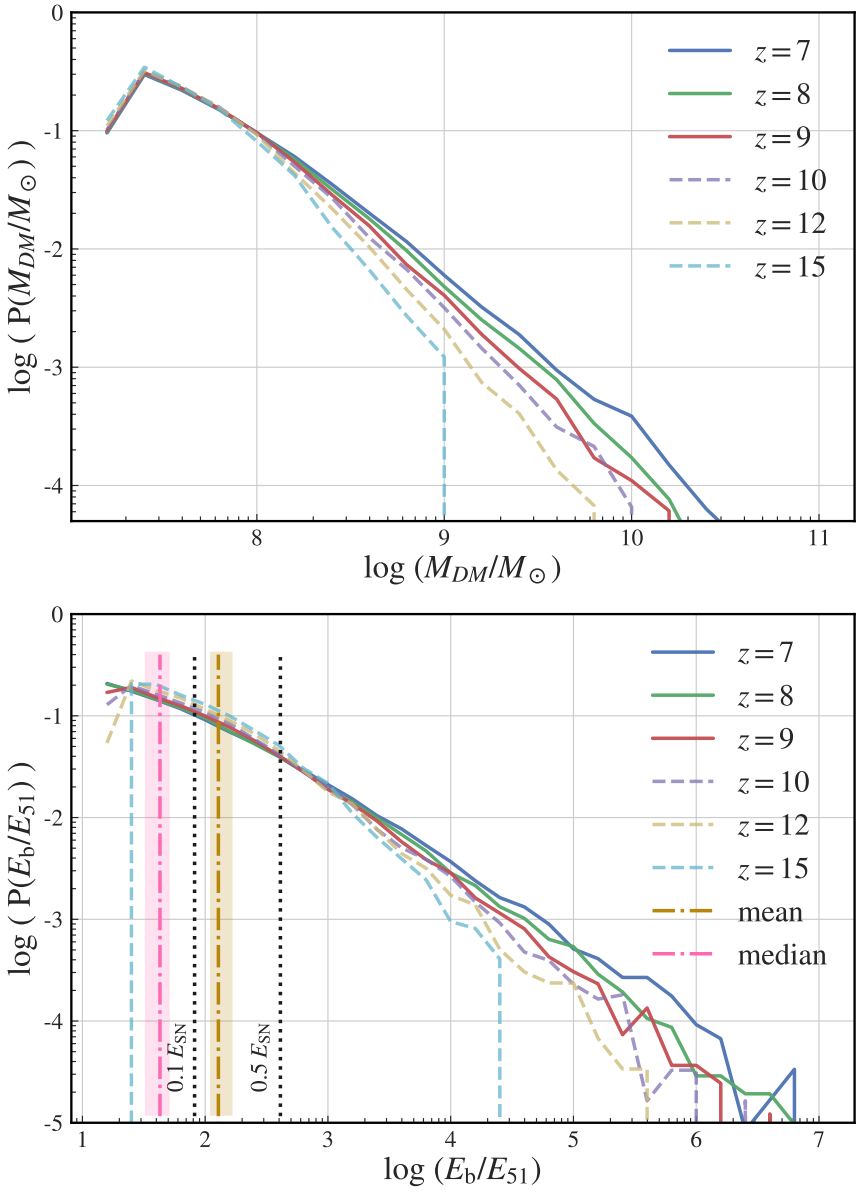

Figure 4.6: The halo DM mass function (HMF, *top*) and gravitational binding energy (*bottom*) for $7 \leq z \leq 15$ expressed as PDFs for all galaxies in the P3SN simulation. As expected, the HMF indicates that most galaxies have $M_{\rm DM} < 10^8 M_\odot$. The dotted line labeled '0.1 $E_{\rm SN}$' in the bottom plot indicates a conservative fraction of SN energy (10%) that couples efficiently to the gas. Galaxies with binding energies below this threshold lose their baryons as a result of a single P3SN Pop III SP SN. This includes galaxies with up to median binding energy (pink dashed line where the shaded region indicates the min/max median value across the redshift range). Similarly, the dashed dark yellow line indicates the mean galaxy $E_{\rm b}$ range. An average of 67%, by number, of halos become unbound by P3SN SN. We include a higher coupling efficiency factor of 0.5 $E_{\rm SN}$, for reference. Binding energy in units of 10^{51} erg.

alize that we are contending with small number statistics and galaxies on the edge of observability. In fact, there is only one observable Pop III-bright galaxy in both the Z4 and Z6 runs and it has magnitude $m_{\rm UV} = 31.38$ mag. This single galaxy is compatible with zero in our sample volume when we consider the 1σ uncertainty.

Additionally, while the fiducial run did not produce this single observable Pop III-bright galaxy at $z = 12$ we note that it was run on a different computer than the Z4 and Z6 runs. Similarly, the fw1 and Z4 runs also generated a single observable Pop III-bright galaxy at $z = 11$ while the fiducial run did not.

The greatest effect on predicted counts of Pop III-bright galaxies occurs when we consider the JWST lensing limit of $m_{\rm UV} \leq 33$ mag and P3SN. At $z = 12$, P3SN predicts more than 2 times the Pop III-bright lensing opportunities than the fiducial run and more than 3.5 times as many at $z = 13$, albeit with a large uncertainty. While the $z = 14$ statistics also indicate more lensing opportunities than in the fiducial case the 1σ uncertainties are very large and compatible with zero observations in our volume.

The locations of these Pop III galaxies, for fw1 and P3SN, are depicted in Figure 4.8 for $z = 8$ and 9. The fw1 simulation has the least amount of SN feedback, owing to the reduced SN loading factor, while P3SN has the most SN feedback. The resulting increase in the metallicity of the gas for P3SN is evident at $z = 8$, immediately after the burst of Pop III star formation. Additionally, P3SN displays a factor of $\approx$2 increase in the number of lensing opportunities for galaxies with $m_{\rm UV} \leq 33$ mag.

For run fw1 at $z = 9$, we note that there are 2143 distinct galaxies in our volume. Of these 179 have $m_{\rm AB} \leq 31.4$ mag and should be detectable by JWST via a deep campaign. Of these observable galaxies, 33 are Pop III-bright with more than 75% of their flux coming from Pop III stars. This is the 18% of observable Pop III-bright galaxies noted in Figure 4.7 for fw1. The fraction of observable Pop III-bright

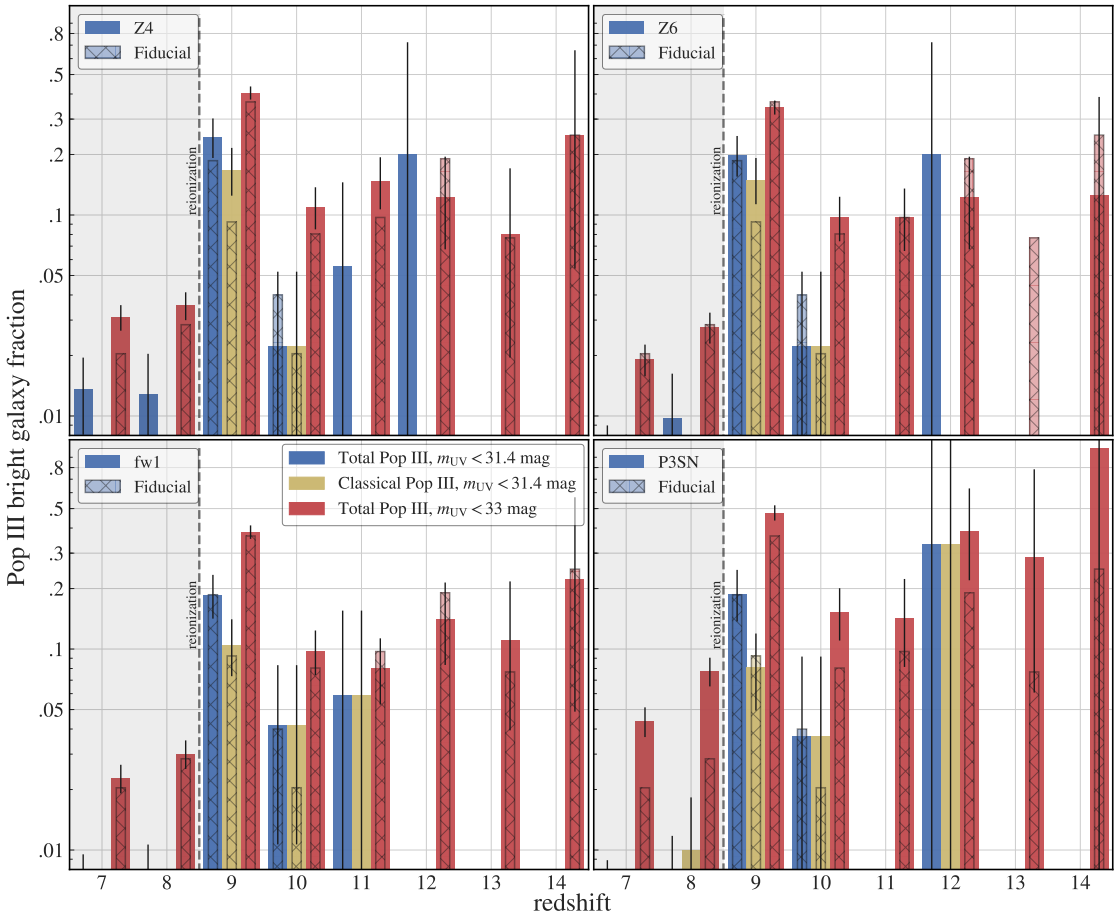

Figure 4.7: A comparison of the fraction of Pop III-bright galaxies across all of our runs. Each panel indicates the joint probability of finding an observable, $m_{\rm UV} \leq 31.4$ mag (blue) or $m_{\rm UV} \leq 33$ mag (red), Pop III-bright, $f_{\rm III}/f_{\rm Tot} \geq 0.75$, galaxy as a fraction of all galaxies meeting the magnitude cutoff. Yellow bars consider only classical Pop III star formation. Run P3SN shows the greatest change from the fiducial case with more lensing opportunities at $z \geq 9$. When considering 1σ errors there is not a significant change in the predictions from the fiducial case for Pop III-bright galaxies at $m_{\rm UV} \leq 31.4$ mag.

galaxies drops to less than 1% when we consider fw1 at $z = 8$ where only 2 galaxies with $m_{\rm AB} \leq 31.4$ mag are Pop III-bright.

The results are similar for run P3SN, the run with the most SN feedback. At $z = 9$ we find 128 of the 2139 galaxies have $m_{\rm AB} \leq 31.4$. Of these, 24 are Pop III-bright, again 18% as was the case for run fw1. Moving to $z = 8$ we find only 1 of the 200 observable galaxies is Pop III-bright, again less than 1%. Similarly, for both runs,

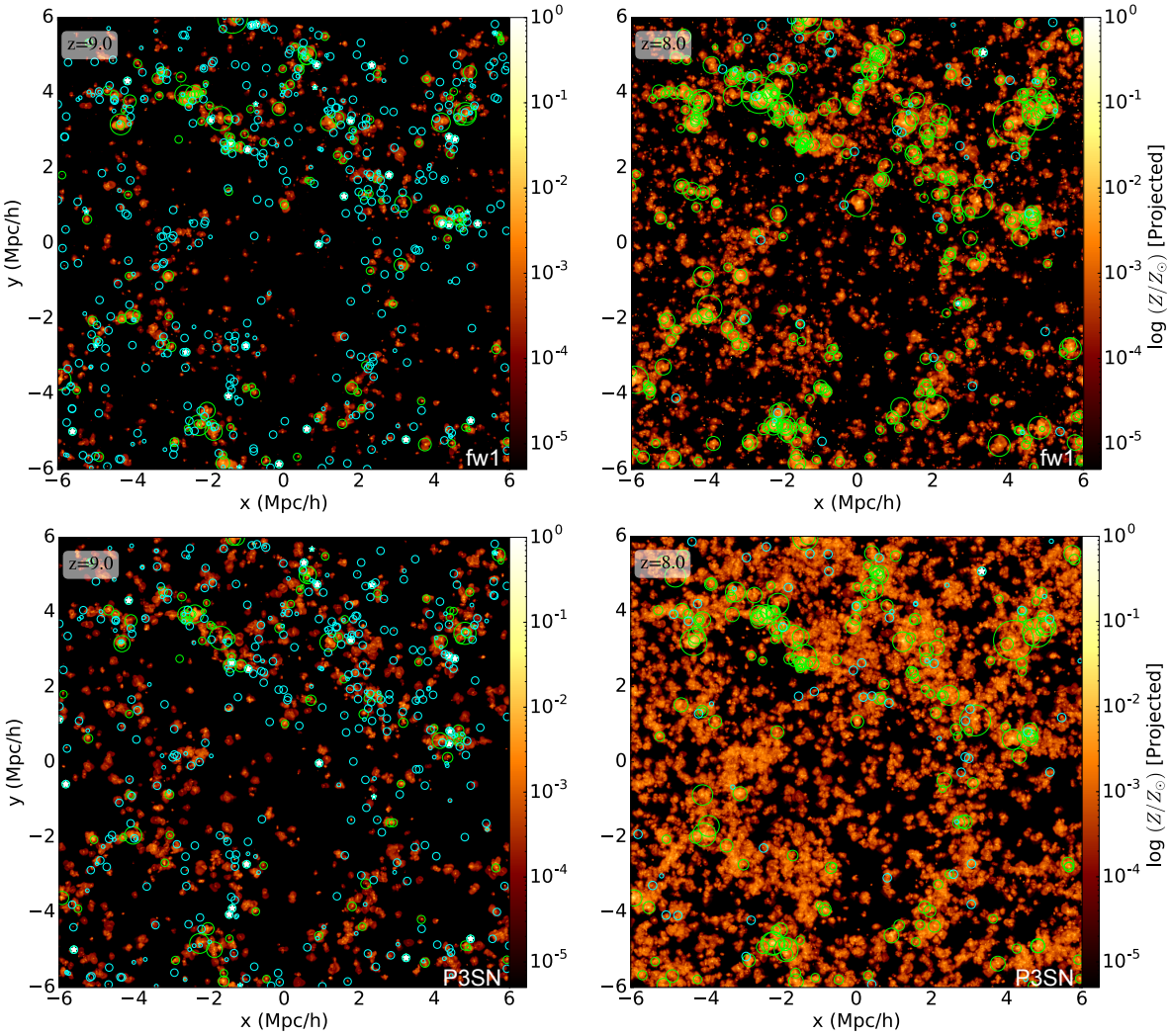

Figure 4.8: The metallicity of the gas for runs fw1 (top) and P3SN (bottom) with circles and stars indicating the locations and relative mass of galaxies. We identify observable galaxies with $m_{\rm AB} \leq 31.4$ mag in green, lensed Pop III-bright ($f_{\rm III}/f_{\rm Tot} \geq 0.75$) galaxies with $m_{\rm AB} \leq 33$ mag in cyan, and observable Pop III-bright ($m_{\rm AB} \leq 31.4$) galaxies with white stars at $z = 9$ and 8. At $z = 9$, just before reionization, there are 33 observable Pop III-bright galaxies for fw1 and 24 for P3SN. At $z = 8$, there are 2 (fw1) and 1 (P3SN). The effects of the increased feedback on the metallicity of the gas for P3SN is immediately apparent in the lower figures, post reionization. Run fw1 has the least amount of SN feedback, while P3SN the most. See the text for a more detailed discussion. Scale is comoving Mpc $\rm h^{-1}$.

there are many more Pop III-bright galaxy lensing opportunities pre-reionization than post.

The consistency in the rate of observable Pop III-bright galaxies at redshifts 9

and 10 across different simulations is not surprising given the Pop III SFRDs. Even though the P3SN Pop III SRFD is down a factor of more than 5 when compared to the fiducial run, the fraction of Pop III stars born in minihalos, and those younger than 3 Myr, are the ones that dominate the contribution to the fraction of Pop III-bright observable galaxies. In other words, the number of Pop III stars born in minihalos is fairly consistent across runs – and these objects form the majority of Pop III-bright galaxies. Additionally, for run P3SN, the fraction of Pop III stars created in larger galaxies declines because of the 10-fold increase in metals that pollutes these halos. Going back to Figure 4.5 we see this as a decrease in the fraction of hybrid galaxies with a Pop III flux fraction $10^{-3} < f_{\rm III}/f_{\rm Tot} < 0.75$.

4.3.3 Chemical Composition

Our two metallicity scalars, $\overline{Z_{\rm P,\star}}$ and $\overline{Z_\star}$, as well as the pristine fraction scalar, are associated with each SP in the simulation. Using $\overline{Z_\star}$ and $P_\star$, we model the fraction of stellar mass in each SP that represents Pop III stars, $P_\star$, as well as the enhanced metallicity of the polluted fraction of Pop II stars, $Z_\star = \overline{Z_\star}/(1 - P_\star)$ as described in Section 4.2.3. Using $Z_{\rm P,\star}$, we also model the fraction of metals in SPs originating in Pop III SN, as $Z_{\rm P,\star}/Z_\star$.

To simplify direct comparisons with our earlier work, we once again adopt the elemental abundance pattern generated by a $60\,M_\odot$ Pop III SN (Heger, 2016) as representative of metal yields in the $25M_\odot \leq M_\star < 140M_\odot$ range, the dominate region of our Pop III IMF. Specifically, the abundances of each element in each SP are computed by mapping the mass fraction of primordial metals, $Z_{\rm P,\star}$, to the abundances found in the ejecta of a $60\,M_\odot$ Pop III SN. We leave a more sophisticated approach, e.g. – stochastically sampling yields from different mass Pop III SN progenitors across the IMF or using a convolution of representative yields, for future work. 'Regular

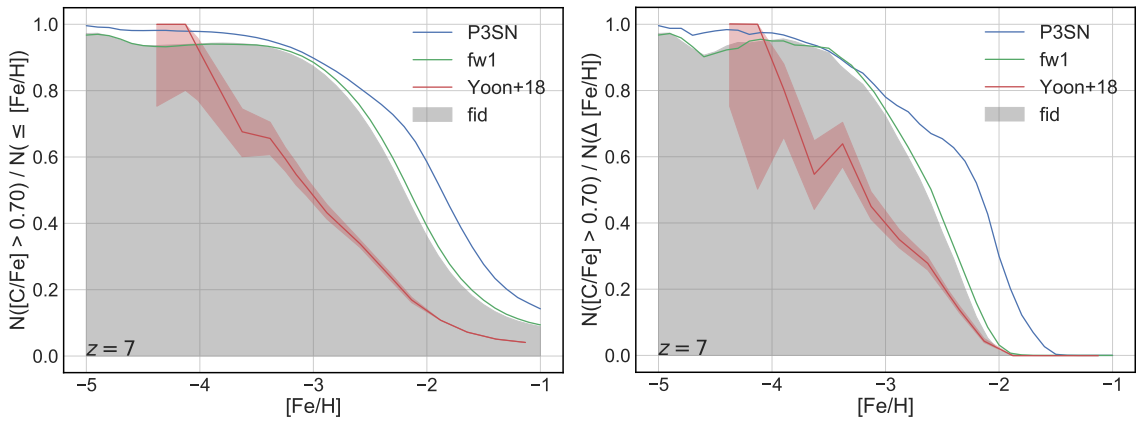

Figure 4.9: *Left*: The fraction of CEMP-no stars when considering all MP stars with [Fe/H] $\leq$ *bin value* for 3 simulations along with observational data by Yoon et al. (2018). For example, for run P3SN, 60% of MP stars with [Fe/H] ≤ -2 are CEMP-no stars. *Right*: The fraction of CEMP-no stars per bin. The observational data, red line, is based on AEGIS medium resolution data analyzed by Yoon et al. (2018), with uncertainties. As expected, the fraction of CEMP-no stars increases with decreasing metallicity. While our fraction of CEMP-no stars is higher than observations between $-4 < [Fe/H] \lesssim -2$, our simulation was stopped at $z = 7$. Many more MP stars with [Fe/H] > -4 would likely form at lower redshift diluting our CEMP-no fraction.

metals', that have a mass-fraction $Z_\star - Z_{\mathrm{P},\star}$, are modeled using abundances provided by Timmes (2016) and are representative of typical Type II SN abundances.

As discussed in detail in Section 2.3.4 and mentioned above, each SP is associated with three scalars $\overline{Z_{\mathrm{P},\star}}$, $\overline{Z_\star}$, and $P_\star$. Using this information, we can compute the mass in Pop III stars as well as the chemical abundances of polluted stars represented by each SP. Using the criteria of Beers & Christlieb (2005), we identify the mass fractions of our SPs that represent metal poor (MP, $[Fe/H] < -1.0$) and CEMP-no ($[Fe/H] < -1.0$ and $[C/Fe] > 1.0$) [1] stars. The results for runs fid, fw1, and P3SN are depicted in Figure 4.9. The left plot depicts the fraction of CEMP-no stars as a function of metallicity when considering all MP stars at or below a [Fe/H] bin. The right plot depicts the fraction of CEMP-no stars per bin.

As expected, the fraction of CEMP-no stars increases as metallicity decreases. This is because most extremely metal poor (EMP, [Fe/H] < -3) stars are likely to

[1] Additionally, CEMP-no stars do not show an enhancement to s or r-process elements.

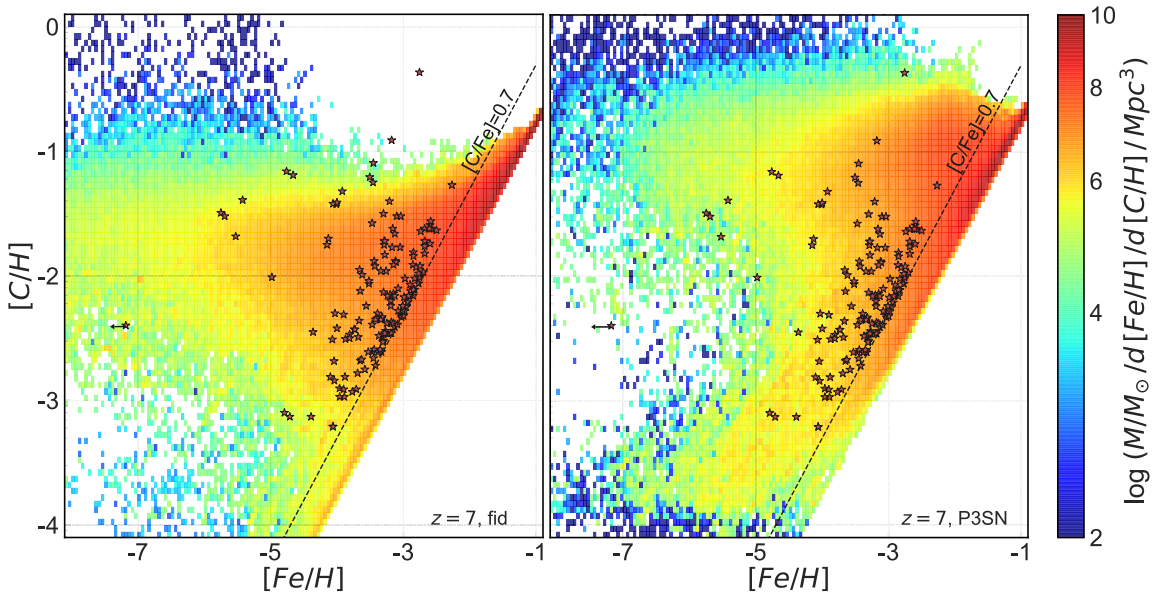

Figure 4.10: Joint PDFs depicting the mass-weighted probabilities for the chemical abundance of [C/H] as a function of the [Fe/H] for all SPs in our fiducial and P3SN simulations at $z = 7$. The largest effect on the overall carbon content of our stars is seen in the P3SN run. Here, carbon is enhanced across the entire range of metallicities, owing to the larger fraction of Pop III ejecta, and is the best match to observations of CEMP-no stars. The P3SN data is also bimodal with an enhance probability of finding stars with $0 < [C/Fe] \lesssim 1$ as well as a population of more MP stars with $[Fe/H] < -2$ and $[C/H] \approx -1$. We have plotted (in purple) CEMP-no stars from Yoon et al. (2016) along with a dashed line indicating $[C/Fe] = 0.7$.

have been born in environments polluted solely by Pop III SN (Hartwig et al., 2018; Ishigaki et al., 2018; Simon et al., 2015; Frebel et al., 2005). While our data shows a much higher fraction of CEMP-no stars over $-4 < [Fe/H] \lesssim -2$ as compared to the survey data, we note that our simulations stop at redshift 7. While most of the CEMP-no stars have likely been formed by this epoch, there are still MP stars forming that will dilute the fraction of CEMP-no stars at later times.

Moving on to a more detailed chemical analysis, Figure 4.10 depicts the mass-weighted PDFs for the chemical abundance of [C/H] as a function of metallicity for the fiducial and P3SN simulations' SPs. Results are very similar to the fid run for Z4, Z6 and fw1. We focus on carbon since it is the defining element when describing

CEMP-no stars (Beers & Christlieb, 2005). The observed chemical composition of CEMP-no stars in the MW halo requires SN progenitors from a top-heavy IMF with stars that end their lives as Type II SN leaving a BH that traps the heavier elements. Several stars in the mass range of our log normal IMF result in SN with such carbon-enhanced yields (Heger & Woosley, 2002).

Each plot is overlaid with the set of CEMP-no stars from Keller et al. (2014) and includes dashed lines depicting the [C/Fe] ratio. While both plots depict and enhanced probability of finding stars with [C/Fe] ≈ 0.5, the P3SN data more clearly displays the bimodal relationship between carbon and iron discussed by Yoon et al. (2016). This plot clearly depicts the enhanced probability of finding stars with $0 < [C/Fe] \lesssim 1$, likely indicative of a population of CEMP-no stars polluted by both Pop III and Pop II SN, as well as a population of MP stars with $[Fe/H] < -2$ and $[C/H] \approx -1$, a population likely polluted solely by Pop III SN. This agreement between the P3SN simulation and observations further supports the idea of a top-heavy IMF for the first stars by tying observations of the chemical composition of ancient MW CEMP-no halo stars to the frequency and nucleosynthetic products of Pop III SN.

4.4 Conclusions

We have conducted a parameter study analyzing the results of 5 large-scale cosmological simulations to assess their impacts on the properties of Pop III star formation and the flux coming from high redshift galaxies. In particular our simulations have explored the effects of

1. lowering the SN mass loading factor, that describes the amount of circumstellar gas carried along with SN ejecta, from 10 times the ejecta mass to 1,

2. varying the value of the critical metallicity that demarcates the boundary between Pop III and Pop II star formation between 10^{-6} and $10^{-4} Z_{\odot}$,

3. implementing a log normal Pop III IMF, within RAMSES, in place of the Salpeter IMF, resulting in an ≈10-fold increase in both the amount of SN energy and metals injected into the ISM.

We have compared these simulations to the fiducial run used in Chapter 3, quantifying the differences and analyzing the implications for predictions made in our previous works.

We find that the parameter ranges explored do not produce a large effect on the overall SFRD. The largest change, produced by P3SN, results in approximately a 50% reduction in the SFRD at $z \leq 12$ and less at $z \leq 9$. The differences between the fid and P3SN run are within sample variance at $z \leq 12$. Looking at the Pop III SFRD, run P3SN again produces the largest change from the fiducial case, this time significant, resulting in a decrease of an average of approximately 0.64 dex (a factor of ≈1/4) averaged over the redshift range $7 \leq z < 18$. This result points to the importance of understanding the Pop III IMF since it has a direct impact on the fraction of surviving Pop III stars at every epoch. Additionally, understanding the IMF relates directly to the amount of SN feedback, again and important consideration since it is relatively easy to dislodge the gas from minihalos in the early universe.

However, the effect of modeling the pristine fraction of gas also has a significant effect on the Pop III SFRD. The subgrid model produces a Pop III SFRD a factor of 2 above the classical model for all simulations except P3SN. For P3SN the difference between the classical Pop III SFRD and the subgrid model was even more pronounced with the classical rate falling to zero for several epochs. We did not see an appreciable difference when varying the critical metallicity for Pop III star formation over 3 orders

of magnitude. This result reinforces our conclusion that our subgrid model following the pristine fraction of gas is more important than knowing the value of the critical metallicity.

We find that Pop III star formation peaks immediately before reionization, in all of our simulations. This is true in terms of both the mass of Pop III dominated galaxies, and in their number counts. This result is consistent with our previous work and reinforces our conclusion that this is best epoch to search for Pop III stars.

While observational constraints on the high redshift LF are uncertain (Finkelstein, 2016; McLeod et al., 2015; Bouwens et al., 2015; Oesch et al., 2015), we find that our models predictions approximately follow the predicted faint end slope at $8 \leq z \leq 10$ and are in reasonable agreement with extrapolated Schechter functions to $z = 12$. We suspect that our simulations' limited resolution and relatively small volume limits our ability to accurately model galaxy counts at $z = 15$ as our galaxy counts in this era underperform both extrapolated Schechter models and O'Shea et al. (2015). None of our simulated galaxies are brighter than $m_{\rm UV} = 31.4$ mag at $z > 13$.

We note the largest differences in Pop III-bright galaxies, with at least 75% of their flux coming from Pop III stars, occurs between the fiducial and P3SN simulations. The feedback effects of the Pop III log normal IMF coupled with the small number of Pop III stars that survive beyond 10 Myr results in far fewer galaxies with moderate Pop III flux fractions between 0.75 and 10^{-3}. The added feedback quenches subsequent star formation in median sized galaxies, and below, resulting in a largely bimodal distribution of Pop III flux fractions for P3SN galaxies. These vary between purely young, small Pop III galaxies and a fraction of older, larger galaxies that maintain a tiny fraction of Pop III stars.

When considering the fraction of observable Pop III-bright galaxies, most of the simulations produced statistics very similar to the fiducial run. However, once again,

the P3SN model stood out. While the fraction of Pop III-bright galaxies with $m_{\rm UV} \leq$ 31.4 mag was similar to the fiducial run, the number of lensing opportunities for galaxies with $m_{\rm UV} \leq 33$ mag increases for the P3SN run by an average factor of 2 over the redshift range $7 \leq z \leq 13$.

Turning to the chemical composition of our stars we note that the P3SN model shows the best agreement with a sample of CEMP-no stars from the MW halos and supports the notion of a Pop III IMF characterized by stars in the $25M_{\odot} \leq M_{\star} < 140M_{\odot}$ range. A significant fraction of such stars go SN producing the carbon-to-iron ratios seen in CEMP-no populations. If fact, our model reproduces the bimodal distribution of these stars where we see one population of CEMP-no stars likely polluted solely by Pop III SN with $[C/H] \approx -1$ and a second population polluted by both Pop III and Pop II SN with a higher overall metallicity and $[C/Fe] \approx +1$.

Our subgrid model that traces the fraction of unmixed gas at subgrid scales improves our ability to reliably produce results, for a given physical model, across a range of simulation resolutions. However, this is just a starting point for the modeling of Pop III star formation. As we have noted throughout the text, there are many aspects of the relevant physics left to include and explore. We will expound on some of the possible follow-on work in the next chapter.

Chapter 5

REVIEW AND FUTURE WORK

This work presents a new model that improves the effective resolution of cosmological simulations with regard to Pop III star formation by tracking the fraction of unpolluted gas at subgrid scales. Our approach statistically tracks the effects of subgrid turbulent mixing, modeling the time scale required to thoroughly mix pollutants within a given volume of gas. The approach allows us to estimate the fraction of pristine gas at any epoch and results in the formation of metal free stars in regions of a simulation that would otherwise generate Pop II stars.

We used this improved physical model to track the unmixed fraction of gas across several simulations ranging from 3 Mpc h^{-1} to 12 Mpc h^{-1} on a side and discovered that higher fractions of pristine, Pop III star forming gas persists at all redshifts. Our results demonstrate that the subsequent Pop III SFR depends more on the turbulent mixing of pollutants at subgrid scales than on knowing the value of the critical metallicity that marks the boundary between metal-free and Pop II star formation. In fact, considering all of our simulations, we found that modeling the time scale required to thoroughly pollute gas at subgrid scales resulted in a 2-3$\times$ increase in the Pop III SFRD, across the redshift range studied, as compared to typical simulations that simply instantaneously update the metallicity of polluted cells.

In addition to improving the resolution of Pop III star formation, our approach provides us with the information needed to improve the modeling of the metallicity of the polluted fraction of gas and stars. Since incomplete mixing implies that metals are concentrated in a sub-volume of simulation cell, we can estimate the metallicity of the polluted fraction as $Z = \overline{Z}/f_{\rm pol}$. This correction to metallicity resulted in fewer

ultra-metal poor (UMP) stars in our simulations and helps to explain the dearth of UMP observations in the MW halo.

With our improved Pop III star formation model in-hand, we modeled the UV luminosity of the galaxies in our simulations down to $z = 7$. We found that our LFs are in good agreement with observations out to $z = 10$ and are in reasonable agreement with extrapolations of observationally based Schechter functions out to $z = 12$. We found that our model underperforms predicted faint-end galaxy luminosities at $z > 12$, but this is likely due to a combination of our limited resolution and the uncertainty in galaxy formation and composition at such high redshifts.

We also looked at the fraction of flux generated by Pop III stars in our galaxies. We found that the epoch immediately before reionization is the best time to look for galaxies with a large fraction, 75%, of their flux coming from Pop III stars. While the epoch of reionization is a free parameter in our simulations, the prediction should hold true even given the uncertainty around this cosmological event. Small, new DM overdensities continue to form, grow, and to attract star-forming baryons in the pristine gas until reionization raises its temperature ending the era of Pop III star formation in minihalos.

Tracking the formation and death of Pop III stars also allowed us to study the initial chemical enrichment of early galaxies and the IGM. Another novel innovation is our creation of a new metallicity scalar, $Z_{\rm P}$, that tracks the nucleosynthetic products of Pop III stars. This scalar enabled us to track the chemical evolution of the early universe at a very small computational cost but provided us with the ability to track the unique elemental abundances generated by the first SN. While simulations typically employ relatively computationally expensive chemical networks to follow a dozen or more species as they are formed, our approach allows us to model those abundances – and to change them – post hoc.

Assuming that the first generation of stars were very massive, as is evidenced by the physics of metal-free gas collapse, we assigned the ejecta from Pop III SN to our new scalar. We were then able to track the composition of subsequent stars via the two metallicity scalars associated with the stars' birth gas: Z and $Z_{\rm P}$. Then, in post processing, we modeled the final chemical composition of our simulated stars by assigning two different abundance patterns to the two types of metallicity.

Considering that the populations of CEMP-no stars with the lowest overall metallicity likely represent a generation of stars born in gas polluted by a single Pop III SN, we found a good match between the chemical composition of CEMP-no stars in the MW halo and simulated SPs that were polluted solely with the produces of a 60 $M_{\odot}$ Pop III SN. Further, when we convolved the material from this Pop III progenitor with elements typical of typical type II SN we were able to predict a second population of CEMP-no stars with higher overall metallicity and lower levels of carbon enhancement. In short we were able to match the bimodal pattern seen in CEMP-no stars that arrises from a population of stars polluted with Pop III SN material and another polluted with both Pop III and Pop II ejecta. We hope this approach will be useful in exploring and characterizing the IMF of Pop III stars as we have only begun to explore its potential utility.

5.1 Follow-on Studies

While this work has demonstrated that we can improve a simulation's ability to model Pop III star formation for a given parameter set and resolution, there are many aspects of the relevant physics left to explore. One of the most prominent is the effect of radiative feedback from massive Pop III stars. While Pop III SNe likely provide enough feedback to evacuate most of the star forming gas from minihalos, radiation from these first stars photoionizes and heats the gas, effectively inhibiting further

star formation even before the stars end their lives as SNe. Quantifying the effects of radiative feedback within the context of our model is an important question that needs to be addressed in a future work.

There is still debate as to the amount of energy generated by early SN across the theoretical mass range of Pop III stars (Chen et al., 2015; Nomoto, 2012). While our simulations assume a standard 10^{51} erg per 10 solar mass, parameterizing this value would help to determine the effect of weak, or stronger, SN on the chemical evolution and subsequent star formation in early galaxies. As one example, we have not included the chemical abundance signature and feedback model that likely results from PISN. While using a $60M_{\odot}$ SN abundance pattern results in a reasonable match with results of stellar archeology, including the iron rich products of PISN is important if we want to characterize the shape of the Pop III IMF. Additionally, including the luminosity of Pop III SN – especially very luminous SN – is likely important when characterizing the LF of the high redshift galaxies.

Similarly, the effects of early BHs and X-ray binaries on the evolution of the first galaxies is another avenue to consider in future modeling. While some studies suggest that feedback from early BHs alone does not significantly effect star formation, feedback from high mass X-ray binaries (HMXB) may promote star formation in nearby minihalos via the formation of molecular hydrogen (Jeon et al., 2012). Also, as with SN, modeling the luminosity of HMXB may provide a more robust model of the luminosity of early galaxies. Of course, the prevalence of HMXB is a function of Pop III binary formation. This is another area of on-going theoretical inquiry.

As discussed previously, the ability to track the nucleosynthetic products from Pop III SN affords us a relatively light-weight method of exploring and constraining the Pop III IMF by comparing the chemical make-up of subsequent stellar generations to observations. While we have started this work in Chapter 3, a more comprehensive

study could be undertaken. Stochastically sampling yields from different masses across the Pop III IMF would provide a more realistic model of the elemental yields that polluted the early universe. Many such models have been suggested, and such a work would be able to rule out IMFs that do not appreciably agree with observations of CEMP-no and MP stars in the MW halo.

Finally, the techniques used to extend the functionality of cosmological simulations to track Pop III SN ejecta can be extended to other types of SN. In fact we have started this work at Arizona State University and now have a version of the code that tracks the unique ejecta patterns generated by neutron star mergers, again without having to track individual elemental species during the simulation run.

The next generation of large telescopes will undoubtedly expand our understanding of the early universe. However, even JWST will be hard pressed to observe the earliest Pop III galaxies without lensing – likely resulting in precious view observations at $z > 12$. For the next decade or more theory coupled with simulation will be our best methodology for understanding the physics of the very early universe that gave birth to the first stars and galaxies. As observations push further back into cosmic history, they will undoubtedly help to constrain our models.

While computational methods have steadily made progress over the last decades, it is only recently that we have been able to model a reasonable fraction of the relevant processes that constitute early star and galaxy formation. However, these processes rely on physics that takes place across a wide range of scales and it will likely be some time before we can hope to include most of it in a self-consistent framework. While we have highlighted one possible approach to analytically modeling some of that physics at subgrid scales, similar insights will help to move the state-of-the-art forward. We hope to be a part of these efforts and to advance the science that contributes to the understanding of our cosmos.

REFERENCES

Abel, T., Bryan, G. L., & Norman, M. L. 2000, ApJ, 540, 39

Abel, T., Bryan, G. L., & Norman, M. L. 2002, Science, 295, 93

An, D., Beers, T. C., Johnson, J. A., et al. 2013, ApJ, 763, 65

Andernach, H., & Zwicky, F. 2017, arXiv:1711.01693

Aoki, W., Frebel, A., Christlieb, N., et al. 2006, ApJ, 639, 897

Asplund, M., Grevesse, N., Sauval, A. J., & Scott, P. 2009, ARA&A, 47, 481

Atek, H., Richard, J., Jauzac, M., et al. 2015, ApJ, 814, 69

Aubert, D., Pichon, C., & Colombi, S. 2004, MNRAS, 352, 376

Barkana, R., & Loeb, A. 2001, Phys. Rep., 349, 125

Barrow, K. S. S., Wise, J. H., Norman, M. L., O'Shea, B. W., & Xu, H. 2017, MNRAS, 469, 4863

Beers, T. C., & Christlieb, N. 2005, ARA&A, 43, 531

Berry, M., Ivezić, Ž., Sesar, B., et al. 2012, ApJ, 757, 166

Bose, S., Deason, A. J., & Frenk, C. S. 2018, arXiv:1802.10096

Bouwens, R. J., Illingworth, G. D., Oesch, P. A., et al. 2012, ApJ, 752, L5

Bouwens, R. J., Illingworth, G. D., Oesch, P. A., et al. 2012, ApJ, 754, 83

Bouwens, R. J., Bradley, L., Zitrin, A., et al. 2014, ApJ, 795, 126

Bouwens, R. J., Illingworth, G. D., Oesch, P. A., et al. 2015, ApJ, 803, 34

Bouwens, R. J., Oesch, P. A., Labbé, I., et al. 2016, ApJ, 830, 67

Bowler, R. A. A., McLure, R. J., Dunlop, J. S., et al. 2017, MNRAS, 469, 448

Bowman, J. D., Rogers, A. E. E., Monsalve, R. A., Mozdzen, T. J., & Mahesh, N. 2018, Nature, 555, 67

Bromm, V., Coppi, P. S., & Larson, R. B. 1999, ApJ, 527, L5

Bromm, V., Coppi, P. S., & Larson, R. B. 2002, ApJ, 564, 23

Bromm, V., & Loeb, A. 2003, Nature, 425, 812

Bromm, V., & Larson, R. B. 2004, ARA&A, 42, 79

Bromm, V., Yoshida, N., Hernquist, L., & McKee, C. F. 2009, Nature, 459, 49

Bromm, V. 2013, The Intriguing Life of Massive Galaxies, 295, 3

Bromm, V. 2014, Mem. Soc. Astron. Italiana, 85, 202

Brook, C. B., Kawata, D., Scannapieco, E., Martel, H., & Gibson, B. K. 2007, ApJ, 661, 10

Caffau, E., Bonifacio, P., François, P., et al. 2011, Nature, 477, 67

Calzetti, D. 2001, PASP, 113, 1449

Cassata, P., Le Fèvre, O., Charlot, S., et al. 2013, A&A, 556, A68

Cayrel, R., Depagne, E., Spite, M., et al. 2004, A&A, 416, 1117

Chai, X., & Mahesh, K. 2012, Journal of Fluid Mechanics, 699, 385

Chen, K.-J., Bromm, V., Heger, A., Jeon, M., & Woosley, S. 2015, ApJ, 802, 13

Christlieb, N., Bessell, M. S., Beers, T. C., et al. 2002, Nature, 419, 904

Clark, P. C., Glover, S. C. O., Klessen, R. S., & Bromm, V. 2011, ApJ, 727, 110

Codis, S., Gavazzi, R., Dubois, Y., et al. 2015, MNRAS, 448, 3391

Coe, D., Zitrin, A., Carrasco, M., et al. 2013, ApJ, 762, 32

Collins, G. W. 1989, New York, W. H. Freeman and Co., 1989, 512 p.,

Cooke, R. J., & Madau, P. 2014, ApJ, 791, 116

Couchman, H. M. P., & Rees, M. J. 1986, MNRAS, 221, 53

Cowley, W. I., Baugh, C. M., Cole, S., Frenk, C. S., & Lacey, C. G. 2018, MNRAS, 474, 2352

Crosby, B. D., O'Shea, B. W., Smith, B. D., Turk, M. J., & Hahn, O. 2013, ApJ, 773, 108

Cullen, F., McLure, R. J., Khochfar, S., Dunlop, J. S., & Dalla Vecchia, C. 2017, MNRAS, 470, 3006

Curl, S. 1963, AIChE J., 9, 175

Dawson, S., Rhoads, J. E., Malhotra, S., et al. 2004, ApJ, 617, 707

de Bernardis, P., Ade, P. A. R., Bock, J. J., et al. 2000, Nature, 404, 955

Deharveng, L., Schuller, F., Anderson, L. D., et al. 2010, A&A, 523, A6

Dijkstra, M., & Wyithe, J. S. B. 2007, MNRAS, 379, 1589

Dopazo, C. 1979, PhFl, 22, 20

Dubois, Y., & Teyssier, R. 2008, A&A, 477, 79

Dubois, Y., Pichon, C., Welker, C., et al. 2014, MNRAS, 444, 1453

Duplat, J., & Villermaux, E. 2008, JFM, 617, 51

Frebel, A., Aoki, W., Christlieb, N., et al. 2005, Nature, 434, 871

Frebel, A., & Norris, J. E. 2015, ARA&A, 53, 631

Frenk, C. S., & White, S. D. M. 2012, AnP, 524, 507

Furlanetto, S. R., & Oh, S. P. 2008, ApJ, 682, 14-28

Einfeldt, B. 1988, SJNA, 25, 294

Eisenstein, D. J., & Hut, P. 1998, ApJ, 498, 137

Eisenstein, D. J., Zehavi, I., Hogg, D. W., et al. 2005, ApJ, 633, 560

Erlebacher, G., Hussaini, M. Y., Speziale, C. G., & Zang, T. A. 1992, JFM, 238, 155

Ezer, D., & Cameron, A. G. W. 1971, Ap&SS, 14, 399

Federrath, C., Roman-Duval, J., Klessen, R. S., Schmidt, W., & Mac Low, M.-M. 2010, A&A, 512, A81

Freeman, K., & Bland-Hawthorn, J. 2002, ARA&A, 40, 487

Ferland, G. J., Korista, K. T., Verner, D. A., et al. 1998, PASP, 110, 761

Finkelstein, S. L. 2016, PASA, 33, e037

Frieman, J. A., Turner, M. S., & Huterer, D. 2008, ARA&A, 46, 385

Gardner, J.P., Mather, J.C., Clampin, M. et al. Space Sci Rev (2006) 123: 485. doi:10.1007/s11214-006-8315-7

Genin, F., & Menon, S. 2010, JTurb, 11, N4

Ghosal, S., Lund, T. S., Moin, P., & Akselvoll, K. 1995, JFM, 286, 229

Girardi, L., Bressan, A., Bertelli, G., & Chiosi, C. 2000, A&AS, 141, 371

Glover, S. 2005, Space Sci. Rev., 117, 445

Greif, T. H., & Bromm, V. 2006, MNRAS, 373, 128

Greif, T. H., Johnson, J. L., Klessen, R. S., & Bromm, V. 2008, MNRAS, 387, 1021

Greif, T. H., Glover, S. C. O., Bromm, V., & Klessen, R. S. 2010, ApJ, 716, 510

Greif, T. H., Bromm, V., Clark, P. C., et al. 2012, MNRAS, 424, 399

Greif, T. H. 2015, ComAC, 2, 3

Guillet, T., & Teyssier, R. 2011, JCoPh, 230, 4756

Guillet, T., Chapon, D., & Labadens, M. 2013, ascl soft, 10002

Guth, A. H., & Pi, S.-Y. 1982, PhRvL, 49, 1110

Guth, A. H., & Kaiser, D. I. 2005, Science, 307, 884

Haardt, F., & Madau, P. 1996, ApJ, 461, 20

Hansen, T. T., Andersen, J., Nordström, B., et al. 2016, A&A, 586, A160

Hahn, O., & Abel, T. 2013, ascl soft, ascl:1311.011

Hartwig, T., Bromm, V., Klessen, R. S., & Glover, S. C. O. 2015, MNRAS, 447, 3892

Hartwig, T., Yoshida, N., Magg, M., et al. 2018, arXiv:1801.05044

Heger, A., & Woosley, S. E. 2002, ApJ, 567, 532

Heger, A., & Woosley, S. E. 2010, ApJ, 724, 341

Heger, A., Fryer, C. L., Woosley, S. E., Langer, N., & Hartmann, D. H. 2003, ApJ, 591, 288

Heger, A., StarFit, 2016, `http://starfit.org/`

Henry, A., Scarlata, C., Domínguez, A., et al. 2013, ApJ, 776, L27

Hirano, S., & Yoshida, N. 2013, ApJ, 763, 52

Hirano, S., Hosokawa, T., Yoshida, N., et al. 2014, ApJ, 781, 60

Hosokawa, T., Omukai, K., Yoshida, N., & Yorke, H. W. 2011, Science, 334, 1250

Howes, L. M., Casey, A. R., Asplund, M., et al. 2015, Nature, 527, 484

Hu, W., & White, M. 1996, ApJ, 471, 30

Hutchins, J. B. 1976, ApJ, 205, 103

Inoue, A. K. 2011, MNRAS, 415, 2920

Ishigaki, M. N., Tominaga, N., Kobayashi, C., & Nomoto, K. 2014, ApJ, 792, L32

Ishigaki, M., Kawamata, R., Ouchi, M., et al. 2018, ApJ, 854, 73

Ishigaki, M. N., Tominaga, N., Kobayashi, C., & Nomoto, K. 2018, ApJ, 857, 46

Ishiyama, T., Sudo, K., Yokoi, S., et al. 2016, ApJ, 826, 9

Janicka, J., Kolbe, W., & Kollmann, W. 1979, JNET, 4, 47

Jeon, M., Pawlik, A. H., Greif, T. H., et al. 2012, AIPC, 1480, 325

Jeon, M., Pawlik, A. H., Bromm, V., & Milosavljević, M. 2014, MNRAS, 444, 3288

Jeon, M., Pawlik, A. H., Bromm, V., & Milosavljević, M. 2014, MNRAS, 444, 3288

Jeon, M., Bromm, V., Pawlik, A. H., & Milosavljević, M. 2015, MNRAS, 452, 1152

Jimenez, R., & Haiman, Z. 2006, Nature, 440, 501

Johnson, J. L., & Bromm, V. 2006, MNRAS, 366, 247

Johnson, J. L., Dalla Vecchia, C., & Khochfar, S. 2013, MNRAS, 428, 1857

Kashikawa, N., Nagao, T., Toshikawa, J., et al. 2012, ApJ, 761, 85

Keller, S. C., Bessell, M. S., Frebel, A., et al. 2014, Nature, 506, 463

Kennicutt, R. C., Jr. 1998, ARA&A, 36, 189

Kim, J.-h., Abel, T., Agertz, O., et al. 2014, ApJS, 210, 14

Kitayama, T., & Yoshida, N. 2005, ApJ, 630, 675

Koekemoer, A. M., Ellis, R. S., McLure, R. J., et al. 2013, ApJS, 209, 3

Komatsu, E., Smith, K. M., Dunkley, J., et al. 2011, ApJS, 192, 18

Krumholz, M. R., & Tan, J. C. 2007, ApJ, 654, 304

Larson, R. B. 1973, MNRAS, 161, 133

Larson, R. B. 2003, RPPh, 66, 1651

Larson, D., Dunkley, J., Hinshaw, G., et al. 2011, ApJS, 192, 16

Leitherer, C., Ekström, S., Meynet, G., et al. 2014, ApJS, 212, 14

Lemaître, G. 1927, ASSB, 47, 49

Liu, C., Mutch, S. J., Angel, P. W., et al. 2016, MNRAS, 462, 235

Livermore, R. C., Finkelstein, S. L., & Lotz, J. M. 2017, ApJ, 835, 113

Loeb, A. 2010, How Did the First Stars and Galaxies Form? By Abraham Loeb. Princeton University Press, 2010. ISBN: 978-1-4008-3406-8

Ma, X., Hopkins, P. F., Faucher-Giguère, C.-A., et al. 2016, MNRAS, 456, 2140

Madau, P. 1995, ApJ, 441, 18

Madau, P., & Dickinson, M. 2014, ARA&A, 52, 415

Maio, U., Ciardi, B., Dolag, K., Tornatore, L., & Khochfar, S. 2010, MNRAS, 407, 1003

Malhotra, S., & Rhoads, J. E. 2002, ApJ, 565, L71

Maiolino, R., Nagao, T., Grazian, A., et al. 2008, A&A, 488, 463

Mannucci, F., Cresci, G., Maiolino, R., Marconi, A., & Gnerucci, A. 2010, MNRAS, 408, 2115

Martin, P. G., Schwarz, D. H., & Mandy, M. E. 1996, ApJ, 461, 265

Mashian, N., Oesch, P. A., & Loeb, A. 2016, MNRAS, 455, 2101

Mason, C. A., Trenti, M., & Treu, T. 2015, ApJ, 813, 21

Mason, C. A., Trenti, M., & Treu, T. 2016, ApJ, 816, 46

McKee, C. F., & Ostriker, E. C. 2007, ARA&A, 45, 565

McKee, C. F., & Tan, J. C. 2008, ApJ, 681, 771

McLeod, D. J., McLure, R. J., Dunlop, J. S., et al. 2015, MNRAS, 450, 3032

Moeng, C.-H. 1984, JAtS, 41, 2052

Moin, P., Squires, K., Cabot, W., & Lee, S. 1991, PhFl, 3, 2746

Nagao, T., Sasaki, S. S., Maiolino, R., et al. 2008, ApJ, 680, 100

Nomoto, K. 2012, AIPC, 1480, 204

Norman, M. L. 2010, AIPC, 1294, 17

Norris, J. E., Christlieb, N., Korn, A. J., et al. 2007, ApJ, 670, 774

Norris, J. E., Yong, D., Bessell, M. S., et al. 2013, ApJ, 762, 28

Oesch, P. A., Bouwens, R. J., Illingworth, G. D., et al. 2013, ApJ, 773, 75

Oesch, P. A., Bouwens, R. J., Illingworth, G. D., et al. 2015, ApJ, 808, 104

Oh, S. P., & Haiman, Z. 2002, ApJ, 569, 558

Oke, J. B., & Gunn, J. E. 1983, ApJ, 266, 713

Omukai, K., Tsuribe, T., Schneider, R., & Ferrara, A. 2005, ApJ, 626, 627

O'Shea, B. W., Wise, J. H., Xu, H., & Norman, M. L. 2015, ApJ, 807, L12

O'Shea, B. W., & Norman, M. L. 2007, ApJ, 654, 66

Pacucci, F., Pallottini, A., Ferrara, A., & Gallerani, S. 2017, MNRAS, 468, L77

Paardekooper, J.-P., Khochfar, S., & Dalla Vecchia, C. 2013, MNRAS, 429, L94

Padoan, P., Nordlund, Å., Kritsuk, A. G., Norman, M. L., & Li, P. S. 2007, ApJ, 661, 972

Padoan, P., Pan, L., Haugbølle, T., & Nordlund, Å. 2016, ApJ, 822, 11

Pallottini, A., Ferrara, A., Gallerani, S., Salvadori, S., & D'Odorico, V. 2014, MNRAS, 440, 2498

Pan, L., & Scalo, J. 2007, ApJ, 654, L29

Pan, L., & Scannapieco, E. 2010, ApJ, 721, 1765

Pan, L., & Scannapieco, E. 2011, Phys. Rev. E, 83, 045302

Pan, L., Scannapieco, E., & Scalo, J. 2012, JFM, 700, 459

Pan, L., Scannapieco, E., & Scalo, J. 2013, ApJ, 775, 111

Peebles, P. J. E. 1968, ApJ, 153, 1

Peebles, P. J. E. 1980, Research supported by the National Science Foundation. Princeton, N.J., Princeton University Press, 1980. 435 p.,

Perlmutter, S., Aldering, G., Goldhaber, G., et al. 1999, ApJ, 517, 565

Piau, L., Beers, T. C., Balsara, D. S., et al. 2006, ApJ, 653, 300

Planck Collaboration, Ade, P. A. R., Aghanim, N., et al. 2016, A&A, 594, A13

Press, W. H., & Schechter, P. 1974, ApJ, 187, 425

Prieto, J. P., Infante, L., & Jimenez, R. 2008, arXiv:0809.2786

Prieto, J., Escala, A., Volonteri, M., & Dubois, Y. 2017, ApJ, 836, 216

Pontzen, A., Roškar, R., Stinson, G., & Woods, R. 2013, ascl soft, ascl:1305.002

Prunet, S., Pichon, C., Aubert, D., et al. 2008, ApJS, 178, 179

Press, W. H., & Schechter, P. 1974, ApJ, 187, 425

Raiter, A., Schaerer, D., & Fosbury, R. A. E. 2010, A&A, 523, A64

Rasera, Y., & Teyssier, R. 2006, A&A, 445, 1

Raskin, C., Scannapieco, E., Rhoads, J., & Della Valle, M. 2008, ApJ, 689, 358

Reed, D. S., Bower, R., Frenk, C. S., et al. 2005, MNRAS, 363, 393

Riess, A. G., Filippenko, A. V., Challis, P., et al. 1998, AJ, 116, 1009

Richardson, M. L. A., Scannapieco, E., & Thacker, R. J. 2013, ApJ, 771, 81

Ritter, J. S., Sluder, A., Safranek-Shrader, C., Milosavljević, M., & Bromm, V. 2015, MNRAS, 451, 1190

Roos, M. 2008, arXiv:0802.2005

Rosen, A., & Bregman, J. N. 1995, ApJ, 440, 634

Sachs, R. K., & Wolfe, A. M. 1967, ApJ, 147, 73

Salpeter, E. E. 1955, ApJ, 121, 161

Salvadori, S., Ferrara, A., Schneider, R., Scannapieco, E., & Kawata, D. 2010, MNRAS, 401, L5

Sarmento, R., Scannapieco, E., & Pan, L. 2017, ApJ, 834, 23

Sarmento, R., Scannapieco, E., & Cohen, S. 2018, ApJ, 854, 75

Sawala, T., Frenk, C. S., Fattahi, A., et al. 2016, MNRAS, 456, 85

Scannapieco, E., Schneider, R., & Ferrara, A. 2003, ApJ, 589, 35

Scannapieco, E. 2005, ApJ, 624, L1

Scannapieco, E., Kawata, D., Brook, C. B., et al. 2006, ApJ, 653, 285

Scannapieco, E., & Brüggen, M. 2010, MNRAS, 405, 1634

Scannapieco, E., & Oh, P. 2004, BAAS, 36, 94.21

Scannapieco, E., & Oh, S. P. 2004, ApJ, 608, 62

Schaerer, D. 2002, A&A, 382, 28

Schaerer, D. 2003, A&A, 397, 527

Schaerer, D., Boone, F., Zamojski, M., et al. 2015, A&A, 574, A19

Schaerer, D. 2002, A&A, 382, 28

Schaye, J., Crain, R. A., Bower, R. G., et al. 2015, MNRAS, 446, 521

Schechter, P. 1976, ApJ, 203, 297

Schneider, R., Ferrara, A., Salvaterra, R., Omukai, K., & Bromm, V. 2003, Nature, 422, 869

Schmidt, M. 1959, ApJ, 129, 243

Schmidt, W., Niemeyer, J. C., & Hillebrandt, W. 2006, A&A, 450, 265

Schumann, U. 1975, JCoPh, 18, 376

Simon, J. D., Jacobson, H. R., Frebel, A., et al. 2015, ApJ, 802, 93

Simpson, C. M., Bryan, G. L., Johnston, K. V., et al. 2013, MNRAS, 432, 1989

Sluder, A., Ritter, J. S., Safranek-Shrader, C., Milosavljević, M., & Bromm, V. 2016, MNRAS, 456, 1410

Smagorinsky, J. 1963, Monthly Weather Review, 91, 99 & Woods, R. 2013, ascl soft, 5002

Schaye, J., Crain, R. A., Bower, R. G., et al. 2015, MNRAS, 446, 521

Sobral, D., Matthee, J., Darvish, B., et al. 2015, ApJ, 808, 139

Somerville, R. S., Hopkins, P. F., Cox, T. J., Robertson, B. E., & Hernquist, L. 2008, MNRAS, 391, 481

Spitzer, L. 1956, Physics of Fully Ionized Gases, New York: Interscience Publishers, 1956,

Stacy, A., Greif, T. H., & Bromm, V. 2010, MNRAS, 403, 45

Sur, S., Pan, L., & Scannapieco, E. 2014, ApJ, 784, 94

Susa, H., Hasegawa, K., & Tominaga, N. 2014, ApJ, 792, 32

Somerville, R. S., Hopkins, P. F., Cox, T. J., Robertson, B. E., & Hernquist, L. 2008, MNRAS, 391, 481

Somerville, R. S., Gilmore, R. C., Primack, J. R., & Domínguez, A. 2012, MNRAS, 423, 1992

Sutherland, R. S., & Dopita, M. A. 1993, ApJS, 88, 253

Teyssier, R. 2002, A&A, 385, 337

Teyssier, R. 2016, Private communication

Hartwig, T., Yoshida, N., Magg, M., et al. 2018, arXiv:1801.05044

Timmes, F. X. 2016, Private communication

Tornatore, L., Ferrara, A., & Schneider, R. 2007, MNRAS, 382, 945

Trenti, M., & Shull, J. M. 2010, ApJ, 712, 435

Trenti, M., & Stiavelli, M. 2008, ApJ, 676, 767-780

Tremblin, P., Audit, E., Minier, V., Schmidt, W., & Schneider, N. 2012, A&A, 546, A33

Tumlinson, J., Giroux, M. L., & Shull, J. M. 2001, ApJ, 550, L1

Tumlinson, J. 2006, ApJ, 641, 1

Turk, M. J., Abel, T., & O'Shea, B. 2009, Science, 325, 601

Turk, M. J., Smith, B. D., Oishi, J. S., et al. 2011, ApJS, 192, 9

Turner, M. S. 1999, Phil. Trans. R. Soc. Lond. A, 357, 7

Umeda, H., & Nomoto, K. 2003, Nature, 422, 871

van de Weygaert, R. 2016, The Zeldovich Universe: Genesis and Growth of the Cosmic Web, 308, 493

van Leer, B. 1979, JCoPh, 32, 101

Venaille, A., & Sommeria, J. 2007, PhFl, 19, 028101

Vogelsberger, M., Genel, S., Springel, V., et al. 2014, Nature, 509, 177

Vogelsberger, M., Genel, S., Springel, V., et al. 2014, MNRAS, 444, 1518

Visbal, E., Haiman, Z., & Bryan, G. L. 2015, MNRAS, 450, 2506

Vreman, B., Geurts, B., & Kuerten, H. 1997, JFM, 339, 357

Walker, T. P., Steigman, G., Kang, H.-S., Schramm, D. M., & Olive, K. A. 1991, ApJ, 376, 51

Whalen, D., Abel, T., & Norman, M. L. 2004, ApJ, 610, 14

Whalen, D., van Veelen, B., O'Shea, B. W., & Norman, M. L. 2008, ApJ, 682, 49-67

Wilkins, S. M., Bouwens, R. J., Oesch, P. A., et al. 2016, MNRAS, 455, 659

Windhorst, R. A., Timmes, F. X., Wyithe, J. S. B., et al. 2018, ApJS, 234, 41

Wise, J. H., Turk, M. J., Norman, M. L., & Abel, T. 2012, ApJ, 745, 50

Wise, J. H., Abel, T., Turk, M. J., Norman, M. L., & Smith, B. D. 2012, AIPC, 1480, 123

Woosley, S. E., Heger, A., & Weaver, T. A. 2002, RvMP., 74, 1015

Woosley, S. E., & Weaver, T. A. 1995, ApJS, 101, 181

Xu, H., Wise, J. H., Norman, M. L., Ahn, K., & O'Shea, B. W. 2016, ApJ, 833, 84

Xu, H., Norman, M. L., O'Shea, B. W., & Wise, J. H. 2016, ApJ, 823, 140

Yajima, H., & Khochfar, S. 2017, MNRAS, 467, L51

Yoshida, N., Abel, T., Hernquist, L., & Sugiyama, N. 2003, ApJ, 592, 645

Yoshida, N., Omukai, K., Hernquist, L., & Abel, T. 2006, ApJ, 652, 6

Yoshizawa, A. 1986, PhFl, 29, 2152

Yong, D., Norris, J. E., Bessell, M. S., et al. 2013, ApJ, 762, 27

Yoon, J., Beers, T. C., Placco, V. M., Carollo, D. et al. 2016, Private communication

Yoon, J., Beers, T. C., Placco, V. M., et al. 2016, ApJ, 833, 20

Yoon, J., Beers, T. C., Dietz, S., Lee, Y. S. et al. 2018, Submitted to ApJ

Zackrisson, E., Rydberg, C.-E., Schaerer, D., Östlin, G., & Tuli, M. 2011, ApJ, 740, 13

Zahid, H. J., Geller, M. J., Kewley, L. J., et al. 2013, ApJ, 771, L19

Zwicky, F. 1933, AcHPh, 6, 110